ANL-19/45

Crack Growth Rate and Fracture Toughness Tests on Irradiated Ex-Plant Materials

Nuclear Science and Engineering Division

About Argonne National Laboratory
Argonne is a U.S. Department of Energy laboratory managed by UChicago Argonne, LLC under contract DE-AC02-06CH11357. The Laboratory's main facility is outside Chicago, at 9700 South Cass Avenue, Argonne, Illinois 60439. For information about Argonne and its pioneering science and technology programs, see www.anl.gov.

DOCUMENT AVAILABILITY

Online Access: U.S. Department of Energy (DOE) reports produced after 1991 and a growing number of pre-1991 documents are available free via DOE's SciTech Connect (http://www.osti.gov/scitech/)

Reports not in digital format may be purchased by the public from the National Technical Information Service (NTIS):

U.S. Department of Commerce
National Technical Information Service
5301 Shawnee Rd
Alexandria, VA 22312
www.ntis.gov
Phone: (800) 553-NTIS (6847) or (703) 605-6000
Fax: (703) 605-6900
Email: **orders@ntis.gov**

Reports not in digital format are available to DOE and DOE contractors from the Office of Scientific and Technical Information (OSTI):

U.S. Department of Energy
Office of Scientific and Technical Information
P.O. Box 62
Oak Ridge, TN 37831-0062
www.osti.gov
Phone: (865) 576-8401
Fax: (865) 576-5728
Email: **reports@osti.gov**

ANL-19/45

Crack Growth Rate and Fracture Toughness Tests on Irradiated Ex-Plant Materials

prepared by
Y. Chen, B. Alexandreanu, and K. Natesan
Nuclear Science and Engineering Division, Argonne National Laboratory

July 2020

Appajosula S. Rao, NRC
Technical Monitor and Program Manager

ABSTRACT

The performance of structural materials is critical for the safe and economic operation of light water reactors. Exposed to neutron irradiation during service, the reactor core internal materials can undergo significant microstructural and microchemical changes, leading to irradiation hardening and embrittlement. To ensure the structural integrity and functionality of nuclear reactor components during long-term operation, material degradation and damage mechanisms must be understood and managed adequately. In this work, irradiated materials harvested from the decommissioned Zorita reactor were studied for their cracking susceptibility and fracture resistance as a function of irradiation dose up to 47 displacement per atom (dpa). The material is a Type 304 stainless steel sectioned from the baffle plates of this pressurized water reactor with 38 years of service.

Crack growth rate and fracture toughness J-resistance (J-R) curve tests were performed in low-corrosion-potential environments at ~315°C. All samples behaved similarly under cyclic loading, and no deteriorated corrosion-fatigue behavior was observed in the test environments. Under constant stress intensity factors, most samples did not show elevated crack growth rates, suggesting an adequate stress corrosion cracking resistance in the test environments. However, an unstable cracking behavior was observed in a 47-dpa sample, resulting in significantly higher crack growth rates than expected at high stress intensity factors. Crack instability was also observed in a 0.06-dpa sample but did not lead to a sustained high crack growth rate.

The impact of neutron irradiation was more evident in the fracture toughness J-R curve tests. As the dose increased, the J-R curve declined considerably and became very shallow at high doses. A fully intergranular fracture morphology was also observed among the high-dose samples ruptured in an air atmosphere at room temperature. This brittle fracture mode in the absence of high temperature water environment confirmed a high degree of embrittlement of this material resulting from its service exposure to neutron irradiation.

EXECUTIVE SUMMARY

The performance of structural materials is critical for the safe and economic operation of light water reactors. During power operation, materials in a reactor core are exposed to a corrosive coolant environment, thermal/mechanical loading, and neutron irradiation. Such service conditions can activate and enhance a wide range of degradation processes, leading to deteriorated material properties and decreased performance. To ensure the structural integrity and functionality of nuclear reactor components, material degradation and damage mechanisms must be understood and adequately managed. There are gaps in the existing knowledge for the long-term operation of LWRs. In particular, data on fracture toughness and crack growth rates at high neutron fluence levels (i.e., greater than 40 dpa) are lacking. Due to the potential impact on the safety and reliability of LWRs, material degradation during long-term operation is of great interest to reactor safety.

In this work, irradiated specimens harvested from the decommissioned Zorita reactor were studied for their cracking susceptibility and fracture resistance as a function of irradiation dose. The material was a Type 304 stainless steel sectioned from the baffle plates of this pressurized water reactor with 38 years of service. Miniature compact-tension specimens about 6.5 mm thick were machined from these materials with different levels of irradiation damage, ranging from ~0.06 to ~47 displacement per atom (dpa), depending on the original locations with respect to the reactor core. Crack growth rate and fracture toughness J-resistance (J-R) curve tests were performed in low-corrosion-potential environments at ~315°C. All samples behaved similarly under cyclic loading, and no deteriorated corrosion fatigue behavior was seen in the test environments. Under constant stress intensity factors, most of the samples show no elevated crack growth rates, which suggests that there was adequate stress corrosion cracking resistance for these irradiated samples in the test environments. However, an unstable cracking behavior was observed in a 47-dpa sample at high stress intensity factors, resulting in significantly higher crack growth rates than expected. Cracking instability was also observed in a 0.06-dpa sample but did not lead to a sustained high crack growth rate.

The effect of neutron irradiation on the fracture toughness was much more evident. As the dose increased, the J-R curve of the decommissioned Zorita baffle plate material declined constantly. At ~47 dpa, the power exponent of the J-R curve was almost zero. There is no doubt that this plate material was severely embrittled by neutron irradiation. In addition, an unexpected fully intergranular (IG) morphology was also observed for all high-dose samples fractured at room temperature in air. The occurrence of such brittle fractures in the absence of a high temperature water environment confirmed that there was a high degree of embrittlement of this material because of its service exposure to neutron irradiation.

TABLE OF CONTENTS

LIST OF FIGURES

LIST OF TABLES

ACKNOWLEDGEMENTS

We would like to thank J. Stjarnsater, A. Jenssen, M. Hiser, and J.M. Smith for arranging the sample machining and shipment. We would like to acknowledge Dr. A.S. Rao, M. Hiser, Dr. R. Tregoning for many helpful discussions. We wish to thank L.A. Knoblich, E.J. Listwan, D. Rink, D. McGann, and S. Yan for their contributions to the experimental effort. This work is sponsored by the Office of Nuclear Regulatory Research, U.S. Nuclear Regulatory Commission, under Agreement Enterprise Wide NRC-HQ-25-14-D-003, Task Order Number NRC-HQ-60-17-T-002, Program Manager: Dr. A.S. Rao.

1 INTRODUCTION

Austenitic stainless steels (SSs) are used extensively in light water reactors (LWRs) thanks to their excellent corrosion and mechanical properties. A number of reactor components critical for the service performance and long-term stability of LWRs are made of 300-series SSs [1]. Exposed to both energetic neutron bombardment and the corrosion of high-temperature water, the SSs in reactor core internals undergo significant microstructural changes during power operation. Various irradiation-induced or irradiation-enhanced degradation processes, such as irradiation-assisted stress corrosion cracking (IASCC), irradiation embrittlement, radiation-induced segregations, and void swelling, can take place at LWR temperatures and irradiation doses, leading to deteriorated mechanical properties, elevated cracking susceptibility, and even geometrical instability of reactor core internals. Due to the potential impacts on the safety and reliability of LWRs, material degradation during long-term operation is of great interest to the LWR research community around the world.

To inform the technical basis of the applicable aging management programs for the long-term operation of LWRs, the mechanisms of irradiation-induced degradations must be identified, and experimental data must be obtained. In addition, there are knowledge and data gaps in the existing information [1,2]. In particular, the data relevant to post-irradiation fracture resistance and crack growth rate (CGR) are needed to evaluate the extent of irradiation embrittlement and IASCC susceptibility. Until recently, most research projects are focused on SSs [3-6] and cast SSs [7, 8] irradiated in test reactors under well-controlled irradiation and temperatures. There are concerns that the differences in neutron spectra and dose rates between test reactors and LWRs may lead to uncertainties in the assessment and evaluation of degradation [9]. Materials obtained from decommissioned Zorita reactors offer excellent opportunities to examine core internal materials exposed to prototypical LWR irradiation and real service conditions, eliminating any uncertainty in damage generation and accumulation. The information obtained from the decommissioned Zorita materials is thus invaluable for long term operation to 80 years.

The objective of the current work was to conduct CGR and J-resistance (J-R) curve tests on irradiated ex-plant materials in simulated LWR environments, and to obtain the CGR and fracture toughness data. The tests were conducted in low-corrosion-potential environments to simulate PWR-relevant service conditions. The target irradiation dose ranges from <1 to 50 displacement per atom (dpa), which is equivalent to about 50 years of service exposure in typical US PWRs.

2 ZORITA MATERIALS AND SAMPLE PREPARATION

2.1 Zorita Materials

The José Cabrera power plant, located in Almonacid de Zorita in Spain, was a nuclear power station with a single-unit pressurized water reactor (PWR) commissioned in late 1960s. After approximately 38 years of operation, the Zorita reactor was decommissioned in 2006, and subsequently was dismantled to restore the power station site. During the process of dismantling the Zorita reactor, a detailed cutting plan was carried out to harvest irradiated materials from the reactor pressure vessel internals. Several pieces of highly radioactive materials were sectioned from different locations of the baffle plates inside the core barrel. The baffle plates were attached to the core barrel with five former plates (named Formers 1 - 5) at different horizontal levels, evenly spaced from the top to the bottom [10]. Former 3 was near the center of the reactor core. Among the harvested materials, the piece farthest away from the reactor core was above Former 1, and was designated “A3.” The other pieces, designated “A,” “B1,” and “B3,” were all cut between Formers 3 and 4, close to the reactor core center.

2.2 Sample Fabrication and Dose Estimates

The harvested Zorita materials were transferred to Studsvik Nuclear AB for decontamination and sample fabrication. Small compact-tension (CT) specimens were machined from the harvested materials with an electron discharge machine [10]. The CT samples are about 6.5 mm thick (i.e., ~0.25 in. thick, or 1/4T) and have two side grooves, the depth of which is about 10% of the sample’s thickness. The nominal width and notch depth of this 1/4T-CT sample are 12 and 5.7 mm, respectively. Figure 1 is a schematic of the samples machined from the decommissioned Zorita baffle plate materials. The intended cracking plane is parallel to the rolling direction.

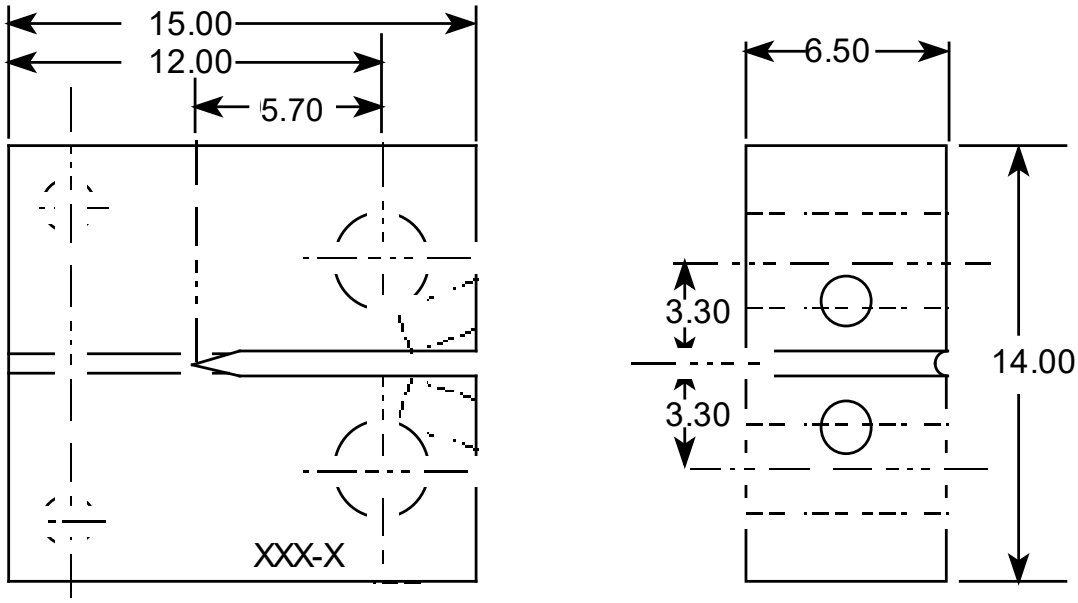

Figure 1. 1/4T-CT specimen machined from the decommissioned Zorita baffle plates (all dimensions are in mm)

Gas Natural Fenosa Engineering, Spain, performed an irradiation dose analysis using a general-purpose Monte Carlo N-particle transport code and a geometric model of the reactor core structure [10]. Based on this analysis, the accumulated displacement doses of the harvested materials ranged from <1 dpa to ~50 dpa, depending on their locations with respect to the reactor core. Because of the neutron attenuation, dose gradients were present in the harvested materials in the direction away from the core center. For each CT sample, the displacement doses were calculated at four corners of the intended cracking plane as shown in Figure 2. The average dose at the four corners is reported in Table 1. The deviation in dose is relatively small within a sample, thanks to its small dimensions.

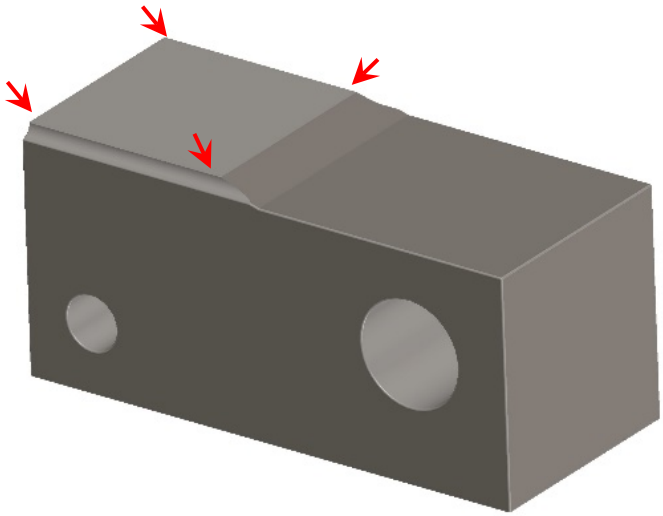

Figure 2. Dose calculation at the corners of the intended cracking plane

Table 1. 1/4T-CT samples fabricated from Zorita materials and dose estimates

Specimen ID	Source Material ID	Target Dose (dpa)	Calculated Average Dose (dpa)	Standard Deviation (dpa)
A3CT03	A3	<1	0.06	0.01
A3CT04			0.06	-
B3CT13	B3	5	8.1	0.9
B3CT14			8.1	0.9
ACT03	A	15-20	15.3	1.6
ACT04			15.3	1.6
B1CT10	B1	40	39.2	1.6
B1CT07			38.5	2.6
B1CT08	B1	50	47.2	2.4
B1CT09			47.2	2.4

3 EXPERIMENTAL DETAILS

3.1 Crack Growth Rate Tests

Two servo-hydraulic mechanical test systems located in the Irradiated Materials Laboratory (IML) at Argonne were used in this study. The IML is a radiation-controlled facility equipped with four air-atmosphere beta-gamma "hot cells." To maintain a proper radiological barrier, the hot cells are kept at a negative pressure with respect to their surroundings. The two test systems are installed in separated hot cells. Each of the hot cells is equipped with a loading frame, autoclave, load cell, linear voltage displacement transducer (LVDT), Instron control console, and computer-based data acquisition system.

The samples were tested in either simulated PWR water or high-purity water with low dissolved oxygen (DO) in this study. The test environments were provided by two separate water recirculation loops, one for PWR water and another for low-DO, high-purity water. Each loop consisted of a water storage tank, a high-pressure pump, a heat exchanger, an autoclave (a volume of ~1 liter), an electrochemical potential cell, a back-pressure regulator, an ion-exchange cartridge, and several heaters. During the tests, water was circulated at a rate of 20–30 mL/min through the autoclaves. The temperature and pressure of the autoclaves were kept at ~315°C and ~1,800 psig, respectively. For the low-DO, high-purity water environment, a gas mixture of 4% hydrogen and nitrogen was used as cover gas. The conductivity of the feedwater was kept below 0.08 μS/cm. This low-DO, high-purity water environment was very similar to the boiling water reactor hydrogen water chemistry (BWR HWC), but with a temperature higher than the typical BWR operating temperature. For the PWR water environment, approximately 1,000 ppm boron and 2 ppm lithium were added in the recirculation system. Pure hydrogen was used as cover gas in the system, resulting a hydrogen content of ~2 ppm in the simulated PWR water. The conductivity of the PWR water was about 20–25 μS/cm at room temperature. Water conductivity was found to slowly increase in the recirculation loop, suggesting a gradual increase of lithium concentration up to 2.5 ppm in the system. Both the low-DO, high-purity and PWR water had very low electrochemical potentials for SSs, which have been shown to suppress the SCC susceptibility of SSs considerably [14]. No significantly different SCC response is expected in these two low-corrosion-potential environments.

During a test, the crack length was monitored continuously using a direct current potential drop (DCPD) technique. With this method, the sample was electronically insulated from the loading system. A constant current passed through the sample and the potential drop across the crack mouth was measured and correlated with the crack extension using a pre-calibrated curve.

In this study, all samples were pre-cracked in their test environments with cyclic loading. A load ratio around 0.2–0.3, a frequency of 1 Hz, and a maximum stress intensity factor (K_{max}) of ~15 MPa $m^{1/2}$ were used for pre-cracking. The objective of the pre-cracking was to generate a sharp fatigue crack and advance the crack tip beyond the region immediately next to the machined notch.

After the sample was pre-cracked, the rise time of the load cycle and the load ratio (K_{min} / K_{max}) were increased gradually while the K_{max} was maintained at its initial pre-cracking level. These changes in loading conditions reduced the contribution of mechanical fatigue to the overall CGR and stimulated the development of environmentally enhanced cracking in the sample. To assess the degree of environmental enhancement, the measured cyclic CGRs in the test environment were compared with the anticipated fatigue growth rates in air under the same

loading conditions. A fatigue growth rate in air was calculated based on the Paris law relationship specified in Section XI of the ASME design code for unirradiated SSs [15]. When the environmentally enhanced cracking became evident, the test was set to a constant load with a periodical partial unloading (PPU) every 2 hours. With a slow-moving crack front, a loading condition of near constant stress intensity factor (K) can be achieved by load shedding. After the SCC performance was evaluated with PPU, a constant-load test period without PPU was also performed to measure the CGR at a near-constant K.

Figure 3 is a schematic of the loading history of the CGR tests. For each specimen, the SCC CGRs were measured at three K levels between 15 and 28 MPa $m^{1/2}$. To avoid any complication due to variation of the plastic zone size, the three SCC CGR test periods were conducted at consecutively higher K levels for each sample. Between the K levels, the crack was advanced with cyclic loading. The K_{max} of the cyclic loading was set to the same level at which the next SCC CGR test would be performed. The magnitude of ΔK was kept the same as that used to induce the environmental enhancement (see Figure 3). With this cyclic loading, the degree of environmental enhancement (i.e., CGR_{env}/CGR_{air}) was similar to that obtained in the previous K level. After the environmental enhancement stabilized, the test was set again to a constant K with and without PPU.

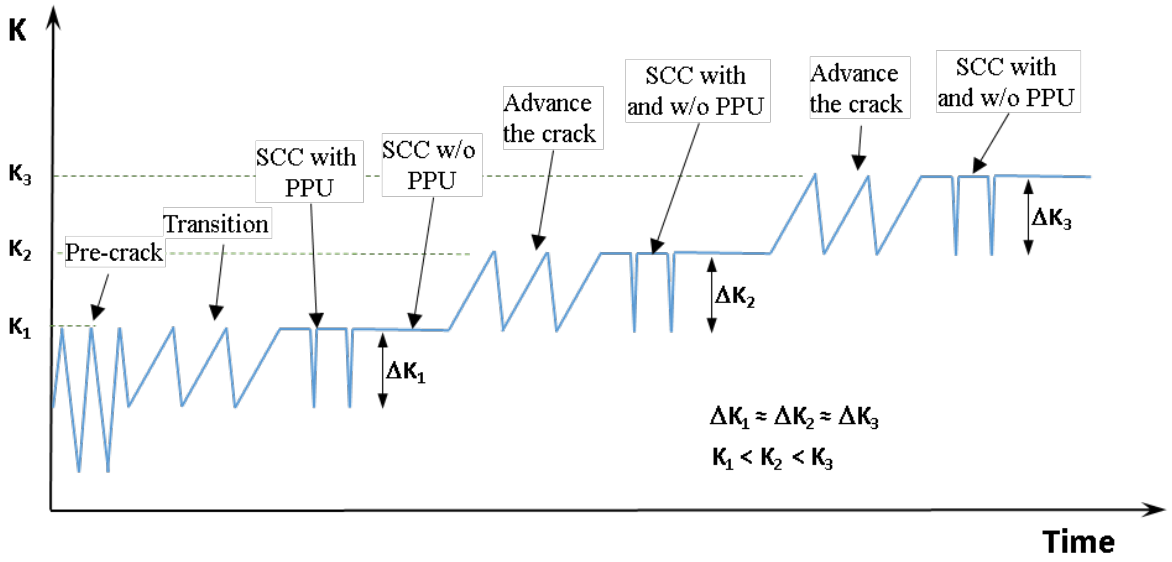

Figure 3. Schematic of the loading history for the CGR test

3.2 Fracture Toughness J-R Curve Test

After a CGR test, a fracture toughness J-R curve test was conducted on the same sample, in the same test environment. The test was performed with a constant displacement rate of 0.08 mm/min, and the load and sample extension were recorded continuously outside the autoclave. The load-line displacement of the specimen was determined by subtracting the extension of the load train, which was measured prior to the test. During the test, the loading process was interrupted periodically, and the specimen was held at a constant extension to measure the crack length with DCPD. Before each DCPD measurement, the sample was allowed to relax at the constant extension for 30 seconds.

At each holding point, a J-integral was calculated using the method specified in ASTM E1820-15a [11]. Then, a J-R curve was constructed by fitting the calculated J values and corresponding crack lengths to a power law correlation. The J values at the intersections of the power law curve and the 0.2- and 2.5-mm offset blunting lines were reported. Note that a blunting line with a slope of 4 times the flow stress was used in this study. This is different from that specified in the ASTM standard (a slope of ~2x flow stress), but is recommended by Mills [12] for materials with high strain hardening coefficients. After neutron irradiations to high doses, the strain hardening coefficients can be greatly reduced for SSs [13], and therefore a steeper blunting line (i.e., 4x flow stress) may be not necessary for highly irradiated SSs. Nonetheless, we still used this steeper blunting line in this study to be consistent with the previous method of data analysis.

3.3 Fracture Surface Characterization

After a CGR test, the sample was cyclically loaded in air at room temperature. After the sample was broken, the fracture surface was examined with a scanning electron microscope (SEM). The failure modes for the CGR and J-R curve test regions were determined. The final crack size was measured from SEM images. The DCPD result was then corrected by scaling proportionally to match the actual crack size measured on the fracture surface. Normally, the correction factor varied from one test to another, ranging from 3% to 80% in most cases.

4 RESULTS

Six 1/4T-CT specimens at different doses were tested in either simulated PWR primary water or low-DO, high-purity water at 312–315°C. Both environments have low corrosion potentials known to reduce the cracking susceptibility of SSs. Table 2 shows the tests performed on each sample and the corresponding test environment and average temperature.

Table 2. Tests performed in this study

Sample ID	Dose (dpa)	Test Environment	Average Temperature (°C)	CGR Test	Fracture Toughness J-R Test
A3CT04	0.06	PWR	314	√	√
B3CT14	8	Low-DO	312	√	√
ACT03	15	Low-DO	315	√	√
B1CT07	39	Low-DO	314	√	√
B1CT09	47	Low-DO	315	√	√
B1CT08	47	PWR	313	√	-

4.1 Specimen A3CT04, ~0.06 dpa

Specimen A3CT04 was cut from the source material "A3," which was located the farthest away from the reactor core. The calculated displacement damage of this sample was about 0.06 dpa (see Table 1). The objective of this test was to establish a baseline for other tests at higher doses. A visual check of the specimen prior to the test revealed that the two side grooves were uneven. One of the side grooves was ~30% deeper than the other. Consequently, the crack propagation direction could been affected slightly. Nonetheless, because this is not a critical issue affecting load distribution or crack length, the sample was deemed adequate for testing.

4.1.1 Crack Growth Rates

The sample was installed in the autoclave, and a set of DCPD leads was spot welded on the sample. After the autoclave was sealed, the system was pressurized to ~1,800 psig, and heated slowly to ~315°C. A small tensile load of about 25 lb. was maintained on the sample during heating. The sample was then soaked in the simulated PWR primary water for 6 days to stabilize the test condition.

Figure 4 shows the time history plots of the crack length and applied K on this sample. The cyclic CGR test started with a K_{max} of ~15 MPa $m^{1/2}$ at a load ratio of 0.2 and 0.5 Hz. The sample readily cracked, and a cyclic CGR (time-based CGR) close to the expected fatigue growth rate in air was obtained after approximately 4.5 hours (see Figure 4a). Next, the load ratio and rise time were gradually increased to induce the environmental effect. Elevated cyclic CGRs were readily observed in this sample. By the end of the cyclic test period *k*, the measured CGR was about 1 order of magnitude higher than that of fatigue growth rate in air. The test was then set to a constant-K SCC test with PPU every 2 hours. A SCC CGR of 9.9×10^{-12} m/s was recorded over a 5-μm crack extension. After the PPU was removed, the SCC CGR was lowered to about 5.4×10^{-13} m/s.

Next, the crack was advanced under cyclic loading with a K_{max} of ~21 MPa $m^{1/2}$. A sudden "jump" in the DCPD measurement (~25 μm) was observed during the first loading cycle when the load was increased (see Figure 4e). Apparently, this jump was an abrupt advance of crack front upon loading and was not a sustainable crack propagation behavior commonly associated

with SCC crack growth. No connected ligaments or uneven crack front were observed either in this sample. After the K_{max} was increased, the environmental enhancement remained strong, and the measured cyclic CGRs were about 1 order of magnitude higher than the fatigue growth rates in air. After about 100 μm crack extension, the test was switched again to a SCC test at ~21 MPa $m^{1/2}$. A relatively high SCC CGR was recorded initially with PPU every 2 hours, but the crack growth slowed considerably after 10–15 hours. An average CGR of 1.5 x 10^{-11} m/s was recorded during the test period with PPU. Without PPU, the CGR dropped to about 3.8 x 10^{-12} m/s.

After the SCC test at ~21 MPa $m^{1/2}$, K_{max} was again increased to ~26 MPa $m^{1/2}$ with cyclic loading. A sudden jump of 191 μm was once again observed in the crack length measurement during the first loading cycle (see Figure 4g). In addition, the crack front seemed to stall slightly after this sudden jump, and several aggressive cyclic loading periods had to be performed to re-activate the crack. Eventually, a level of environmental enhancement similar to that observed at ~16 and ~21 MPa $m^{1/2}$ was obtained. When the test was set to a SCC CGR with PPU, a sudden jump of ~40 μm in crack length was observed during this transition (see Figure 4h). The measured CGR was about 1.8 x 10^{-11} m/s with PPU, and decreased to 2.0 x 10^{-12} m/s without PPU. After the measurements at this K level, the CGR test on this sample concluded. All CGR results of this sample are summarized in Table 3.

Table 3. Crack growth rates of Specimen A3CT04 (~0.06 dpa) in PWR water

Test Period [1]	Test Time (hr)	Test Temp. (°C)	Load Ratio	Rise Time (s)	Return Time (s)	Hold Time (s)	K_{max} (MPa $m^{1/2}$)	ΔK (MPa $m^{1/2}$)	CGR in Env. (m/s)	CGR in Air (m/s)	Crack Length (mm)
Start	0.2										5.700
a[2]	7.7	314	0.35	0.45	0.45	0.05	14.8	9.7	3.38E-08	2.36E-08	5.918
b	12.5	314	0.41	0.88	0.88	0.12	15.3	9.0	2.28E-08	1.00E-08	6.097
c	22.8	314	0.50	2.16	2.16	0.34	15.6	7.7	1.12E-08	2.73E-09	6.276
d	32.5	314	0.60	4.16	4.16	0.84	15.4	6.1	1.84E-09	7.19E-10	6.305
e	47.2	314	0.64	8.16	4.08	1.84	15.1	5.5	6.94E-10	2.65E-10	6.326
f	55.8	314	0.62	24.8	4.1	5.2	15.4	5.9	8.30E-10	1.08E-10	6.343
g	73.8	314	0.58	50.3	10.0	9.7	15.4	6.5	3.89E-10	7.01E-11	6.361
h	96.5	314	0.59	99.9	10.0	20.1	15.5	6.3	2.87E-10	3.23E-11	6.379
i	129.8	314	0.59	208.6	10.0	41.4	15.6	6.4	1.31E-10	1.62E-11	6.392
j	167.1	314	0.59	417.7	10.0	82.3	15.6	6.4	8.39E-11	8.31E-12	6.401
k	196.0	314	0.59	836.1	10.0	163.9	15.6	6.5	4.59E-11	4.23E-12	6.405
1	316.1	314	0.60	12	12	7200	15.5	6.2	9.92E-12	4.32E-13	6.410
2	430.1	314	1.0	-	-	-	15.6	-	5.42E-13	-	6.411
l	454.3	314	0.70	83.1	10.0	16.7	21.3	6.4	5.27E-10	4.49E-11	6.482
m	486.2	314	0.69	208.3	10.0	41.7	21.2	6.5	1.71E-10	1.89E-11	6.498
n	510.8	314	0.69	417.2	10.0	82.8	21.3	6.6	8.98E-11	9.75E-12	6.506
o	550.7	314	0.69	835.2	10.0	164.8	21.2	6.6	6.35E-11	5.00E-12	6.514
3 [2]	655.0	314	0.70	12	12	7200	21.5	6.5	1.51E-11	5.36E-13	6.540
4	748.5	314	1.0	-	-	-	21.6	-	3.85E-12	-	6.542
p	768.0	314	0.75	82.5	9.9	17.5	26.5	6.6	1.05E-10	5.22E-11	6.742
q	791.4	314	0.75	41.3	9.9	8.7	26.5	6.7	2.55E-10	1.07E-10	6.757
r	815.4	314	0.74	83.0	10.0	17.0	26.6	6.9	2.77E-10	5.95E-11	6.774
s	837.9	314	0.74	208.4	10.0	41.6	26.8	7.1	1.59E-10	2.59E-11	6.786
t	863.4	314	0.73	417.5	10.0	82.5	26.8	7.2	9.35E-11	1.35E-11	6.794
u	889.0	314	0.73	835.8	10.0	164.2	26.9	7.2	7.19E-11	6.89E-12	6.799
5	960.7	314	0.74	12	12	7200	27.5	7.1	1.77E-11	7.72E-13	6.848
6	1,085.2	314	1.0	-	-	-	27.5	-	2.02E-12	-	6.850
Complete											

[1] Cyclic test periods are named in alphabetical order, and constant-K test periods are named in numerical order.
[2] Crack growth rate in the later part of the test period is reported.

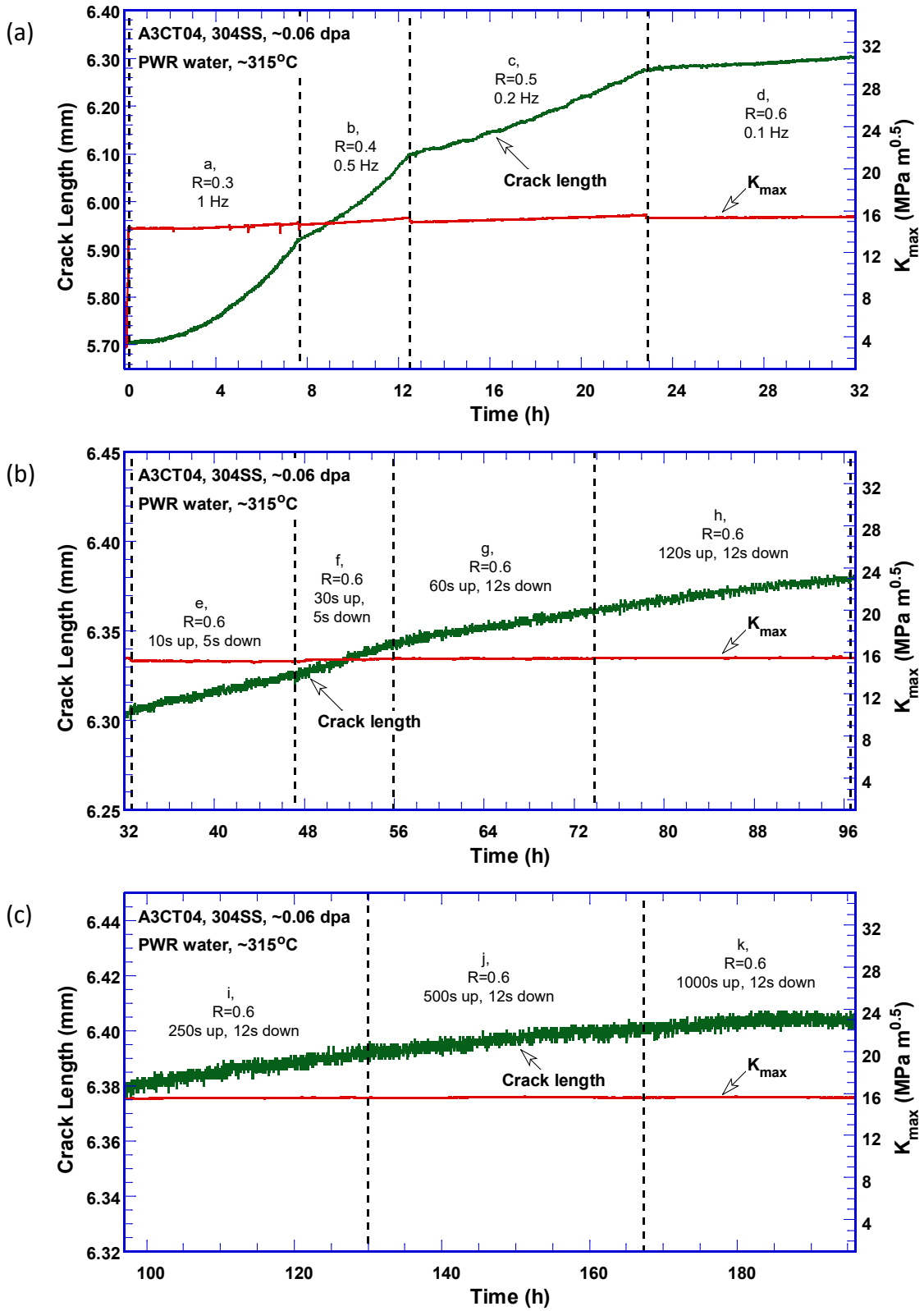

Figure 4. Crack-length-vs.-time plot of Specimen A3CT04 (~0.06 dpa) tested in PWR water: test periods (a) a-d, (b) e-h, (c) i-k, (d) 1-2, (e) l-o, (f) 3-4, (g) p-u, and (h) 5-6

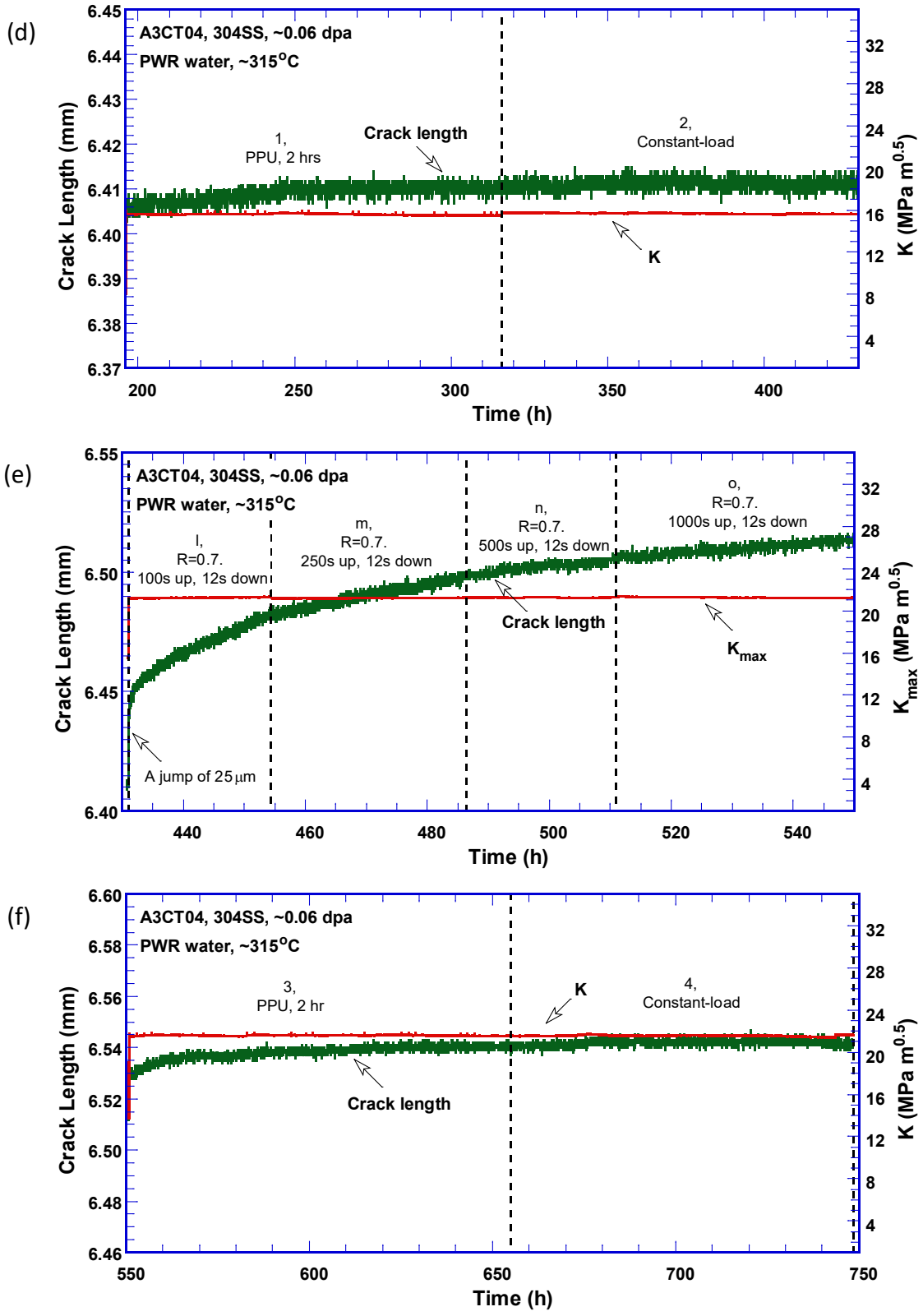

Figure 4. (Cont.)

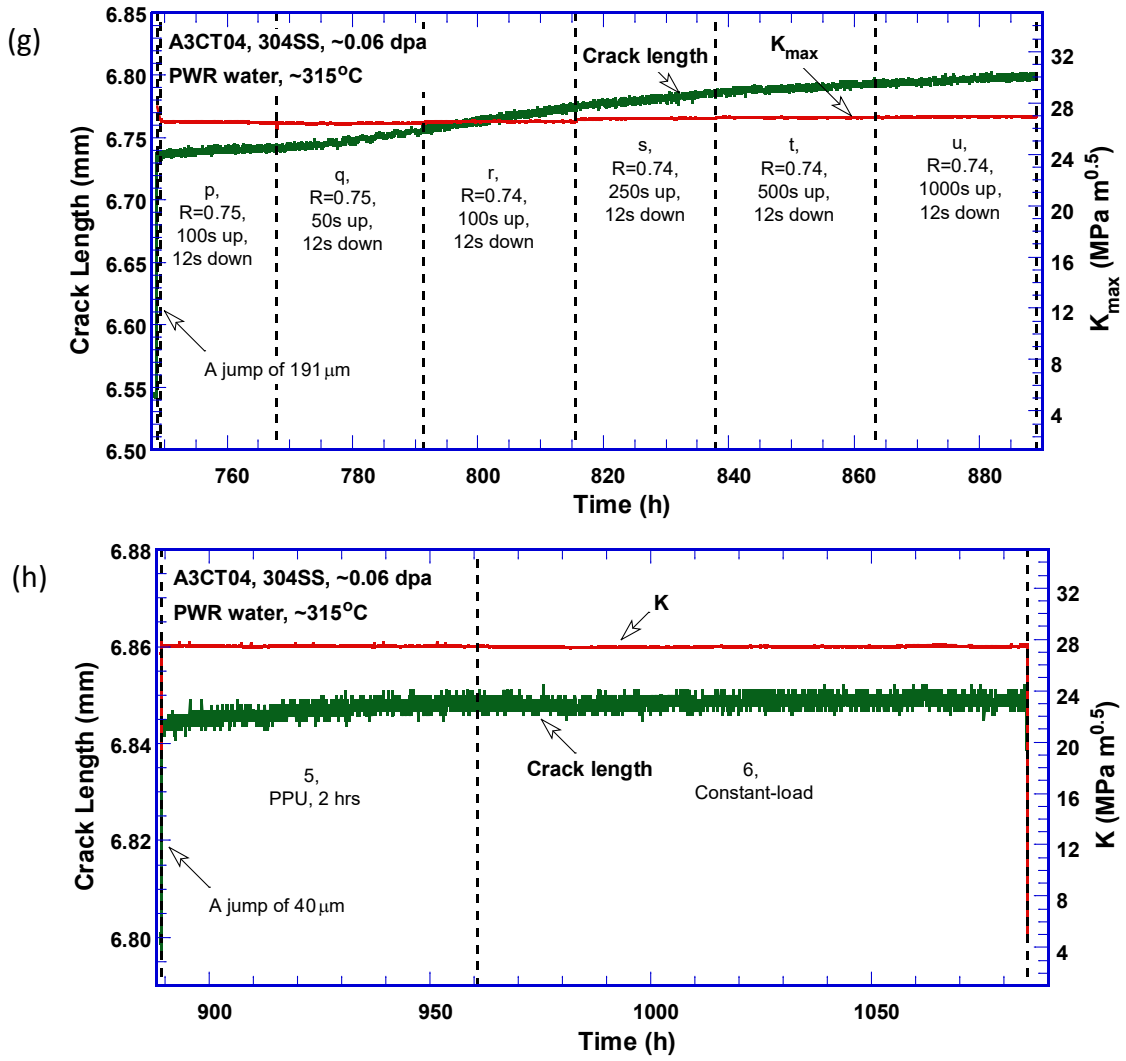

Figure 4. (Cont.)

Figure 5 shows the cyclic CGRs in water as a function of the anticipated fatigue growth rates in air under the same loading. The fatigue growth rates are calculated based on the Paris law relationship for unirradiated SSs specified in Section XI of the ASME design code [15]. As shown in Figure 5, the data points at the upper right corner are close to the diagonal line, which indicates cracking behavior dominated by mechanical fatigue. As load ratio and rise time increase, the fatigue growth rate decreases gradually. The measured CGRs in water also deviate farther above the diagonal line, suggesting an increasing trend of environmental contribution to crack growth. The environmental enhancement is strong in this sample, and the measured CGRs can be more than 1 order of magnitude higher than the fatigue growth rates at the end of cyclic CGR test. Similar environmentally enhanced cracking can also be seen when the crack was advanced with cyclic loading between two applied K levels.

Figure 6 shows the SCC CGRs measured at three K levels with and without PPU. A disposition curve (NUREG-0313) previously developed with the data of unirradiated, sensitized SSs in high-DO environments is also included in the figure [16]. The sudden jumps in crack length are not accounted for in SCC CGRs since they are not a sustainable cracking behavior in this sample. The possible mechanisms for such a cracking instability will be discussed later. As shown in

Figure 6, all SCC CGRs are below the NUREG-0313 disposition curve, suggesting good SCC resistance for this sample in the test environment. The CGRs measured with PPU are higher than those measured without PPU. For the data with PPU, a weak K dependence can be seen between 16 and 21 MPa $m^{1/2}$. Without PPU, the CGRs are too low to be determined confidently. A much longer test time would be required for such slow CGRs in the test environment. Nonetheless, the good SCC property is evident for the decommissioned Zorita baffle plate material at this low dose level.

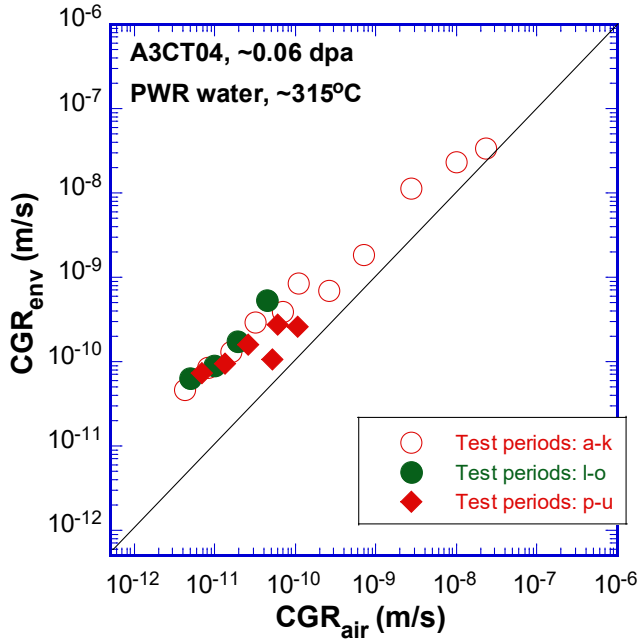

Figure 5. Cyclic CGRs of Specimen A3CT04 (~0.06 dpa) tested in PWR water

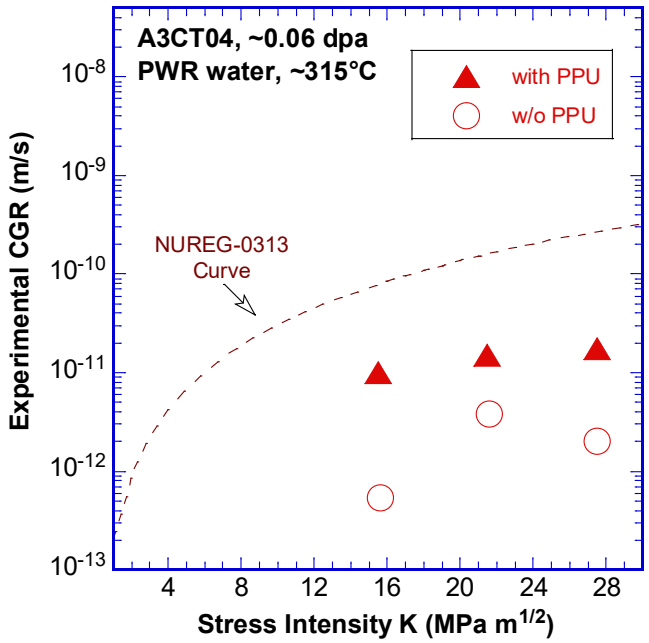

Figure 6. SCC CGRs of Specimen A3CT04 (~0.06 dpa) tested in PWR water

4.1.2 Fracture Toughness J-R Curve

After the CGR test, a fracture toughness J-R curve test was performed on the sample in the test environment. The test was performed at ~315°C with a constant displacement rate about 0.08 mm/min. The ratio of a/W for the starter crack was about 0.57. Figure 7 shows the obtained J-R curve. The maximum J and Δa values can be determined with this sample are also included in the figure. A power law relationship $J = 220 \times \Delta a^{0.61}$ is obtained with the J-versus-Δa data, and the J_Q value at the 0.02-mm offset line is about 100 kJ/m^2, lower than those of typical unirradiated or low-dose SSs. Note that a flow stress of 375 MPa was assumed for this sample in the J-R curve analysis. This low flow stress leads to a low J_{max} for such a small sample, and the data points above J_{max} have to be included in the curve fitting. The curvature of the final crack front is also too high. Consequently, the J_Q value obtained from this sample cannot be validated for a J_{1C} per the ASTM E1820-15 [11]. Nonetheless, the obtained J-R curve has a high power exponent (~0.6), similar to those observed in unirradiated SSs.

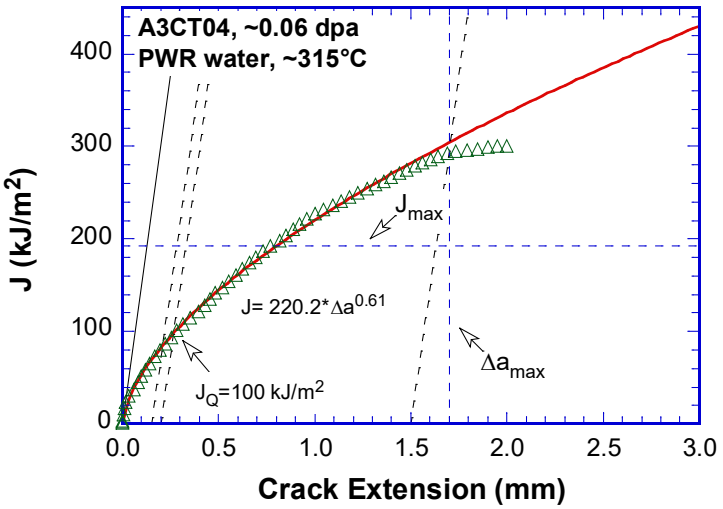

Figure 7. J-R curve of Specimen A3CT04 (~0.06 dpa) tested at ~315°C

4.1.3 Fracture Morphology

After the J-R curve test, the sample was cyclically loaded in air at room temperature to break the remaining ligament. The sample was then cleaned and moved to a shielded SEM for examination. Figure 8 shows the entire fracture surface. The CGR crack front is quite straight, suggesting well-controlled loading during the CGR test. The CGR test region shows a transgranular (TG) morphology and can be easily distinguished from the J-R curve test region. Figure 9 shows an enlarged view along the sample centerline. Details of the early and late stages of CGR test appear in Figure 10 and Figure 11, respectively. The crack propagates from bottom to top in all figures. The fracture morphology in the J-R curve test region is predominantly ductile, as shown in Figure 12a. Nonetheless, a large elongated brittle area can be seen parallel to the cracking direction (Figure 12b). The post-JR fatigue region again shows a TG morphology, followed by a ductile tearing appearance as shown in Figure 9. With these SEM images, the final crack size was determined, and the CGR results were corrected by scaling them proportionally to match the final crack size.

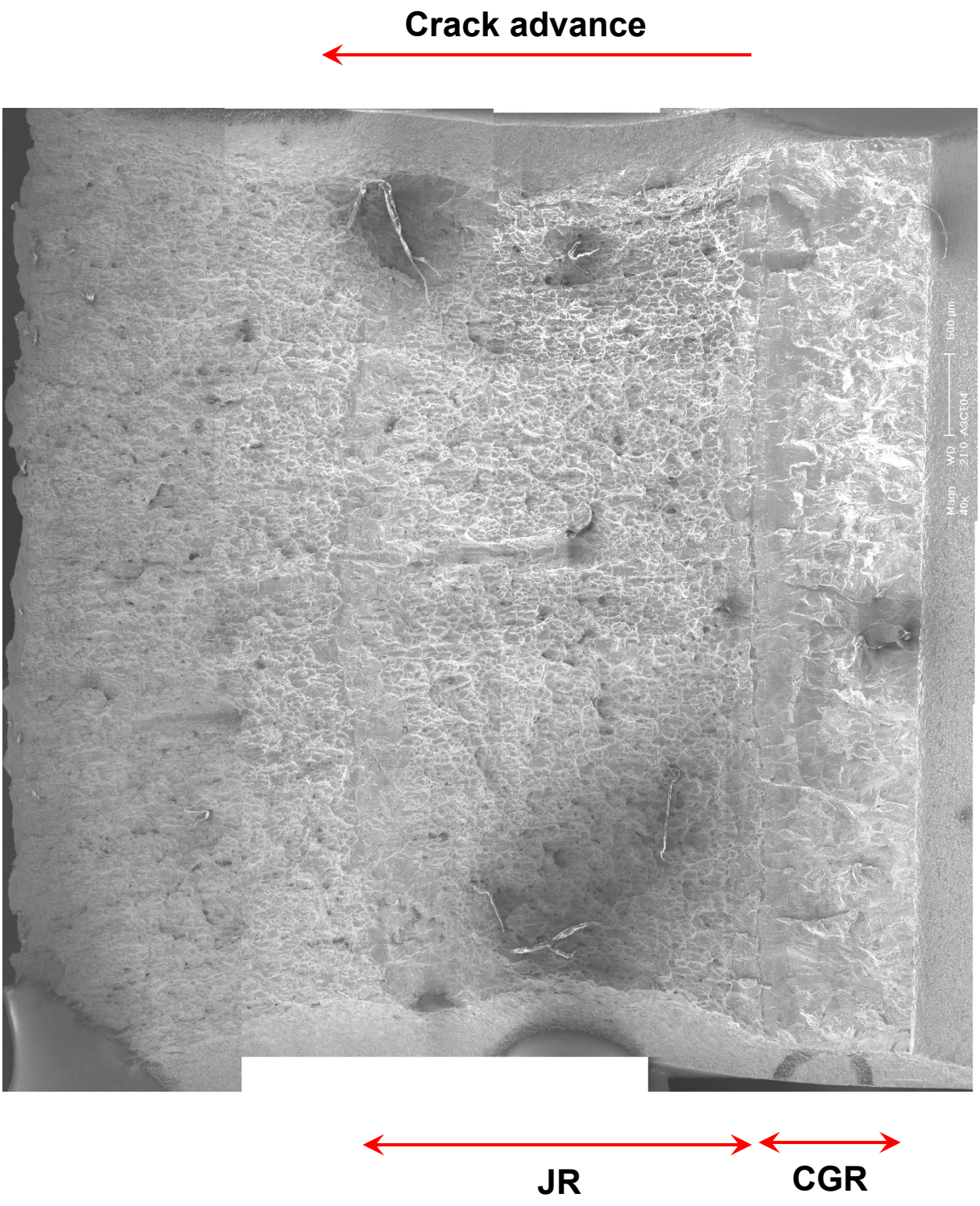

Figure 8. Fracture surface of Specimen A3CT04, ~0.06 dpa

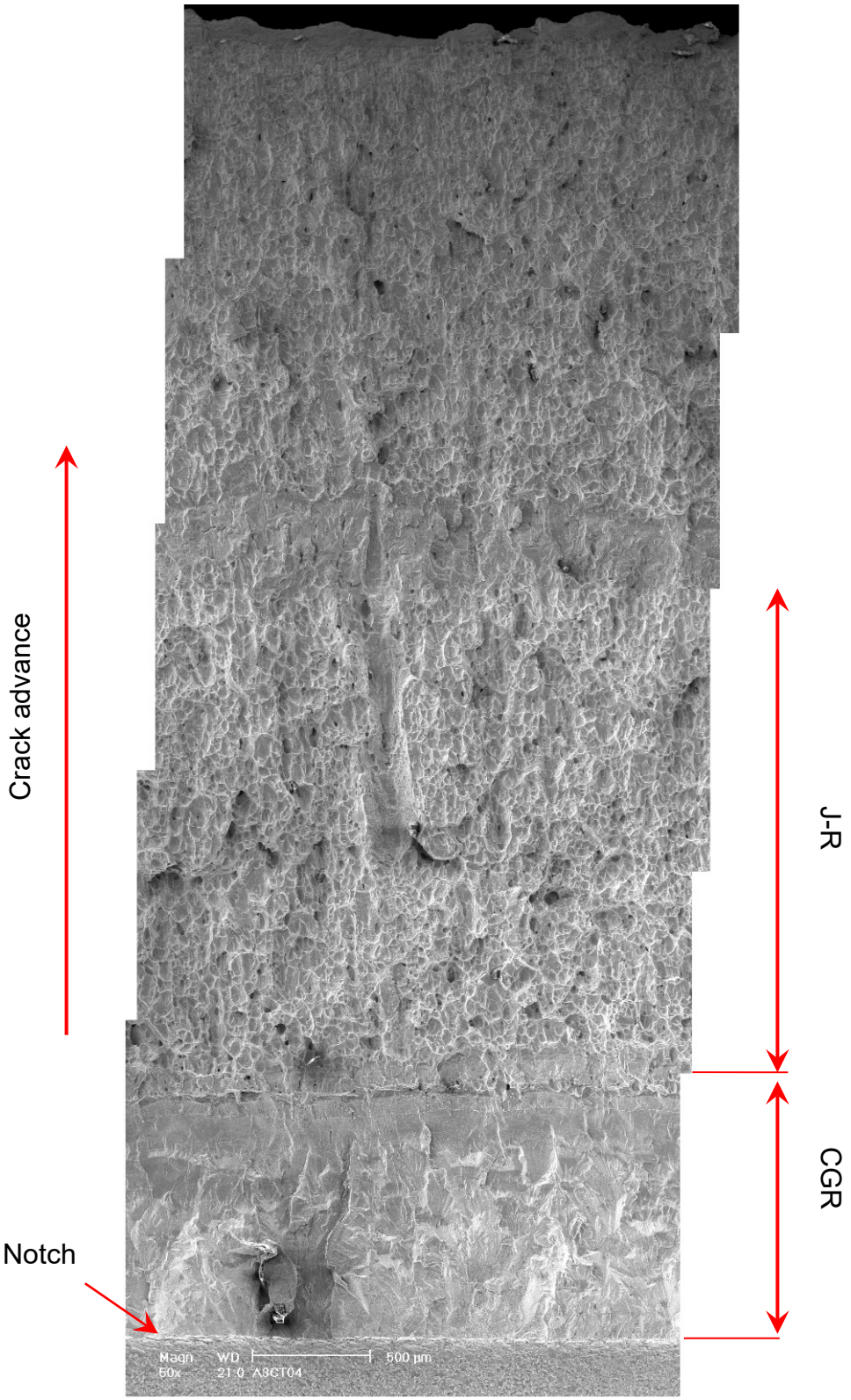

Figure 9. Enlarged view along the centerline of Specimen A3CT04, ~0.06 dpa

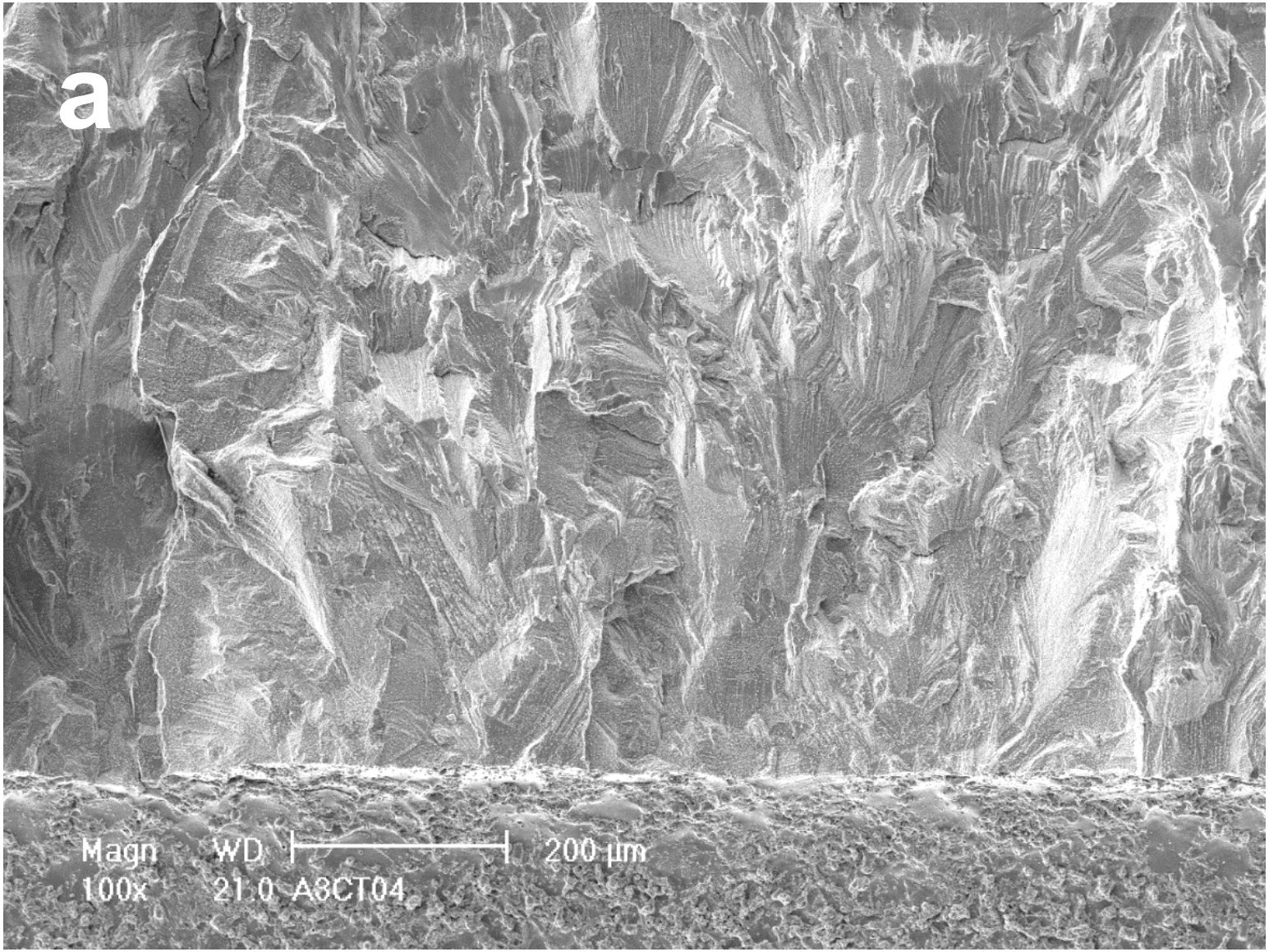

Figure 10. TG morphology at the beginning of the CGR test of Specimen A3CT04

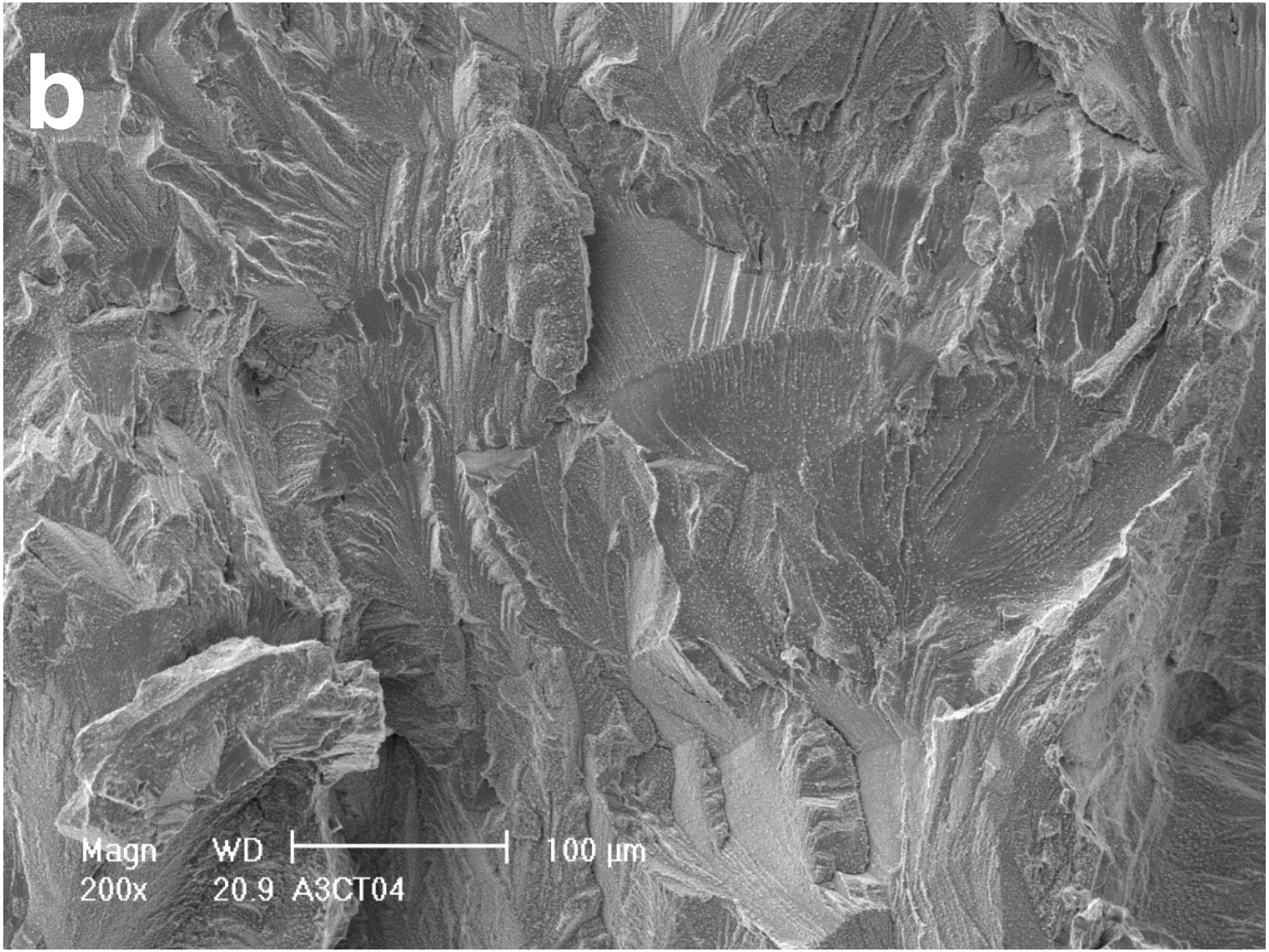

Figure 10. (Cont.)

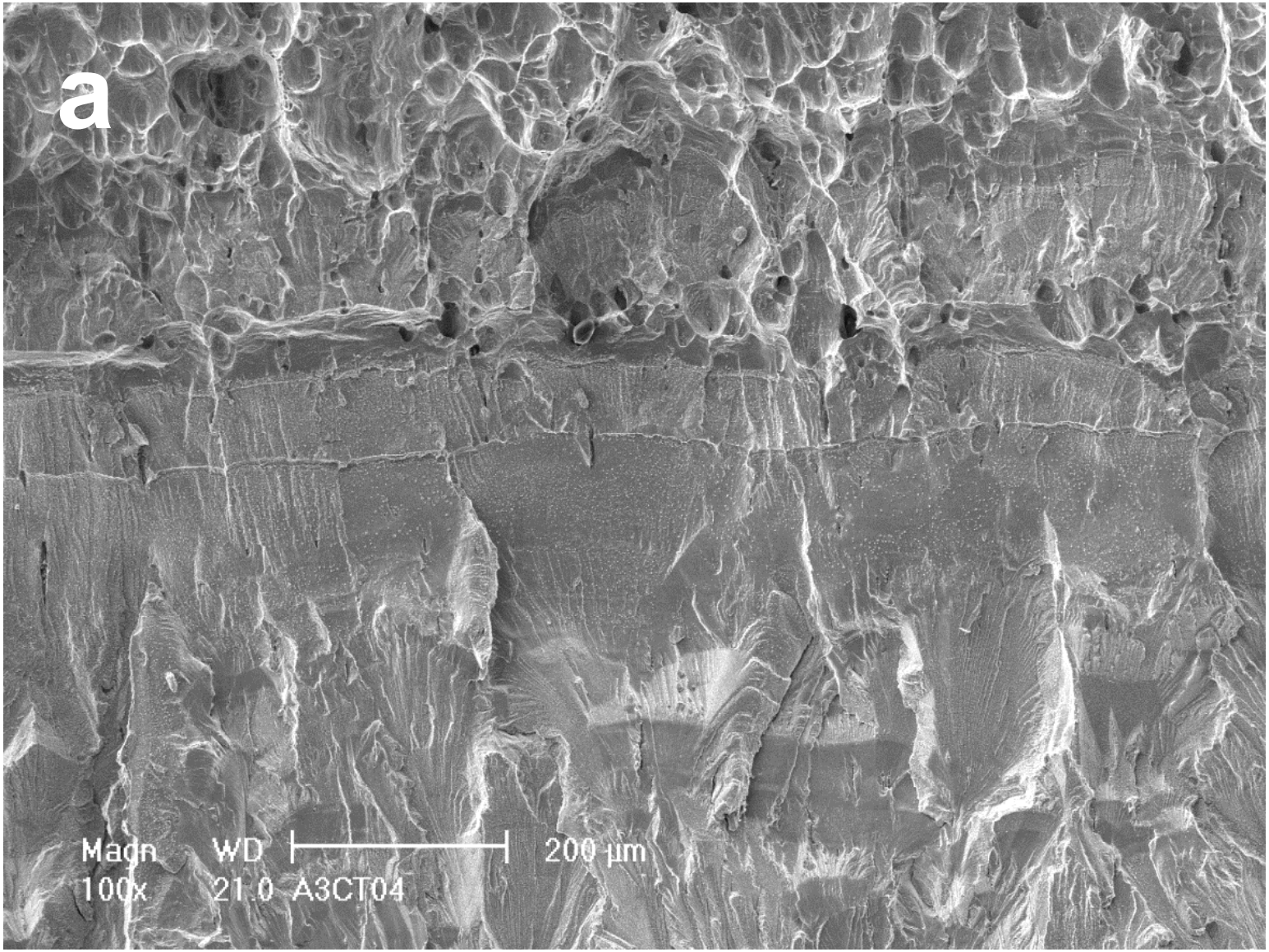

Figure 11. Transition region from the CGR to J-R curve test of Specimen A3CT04

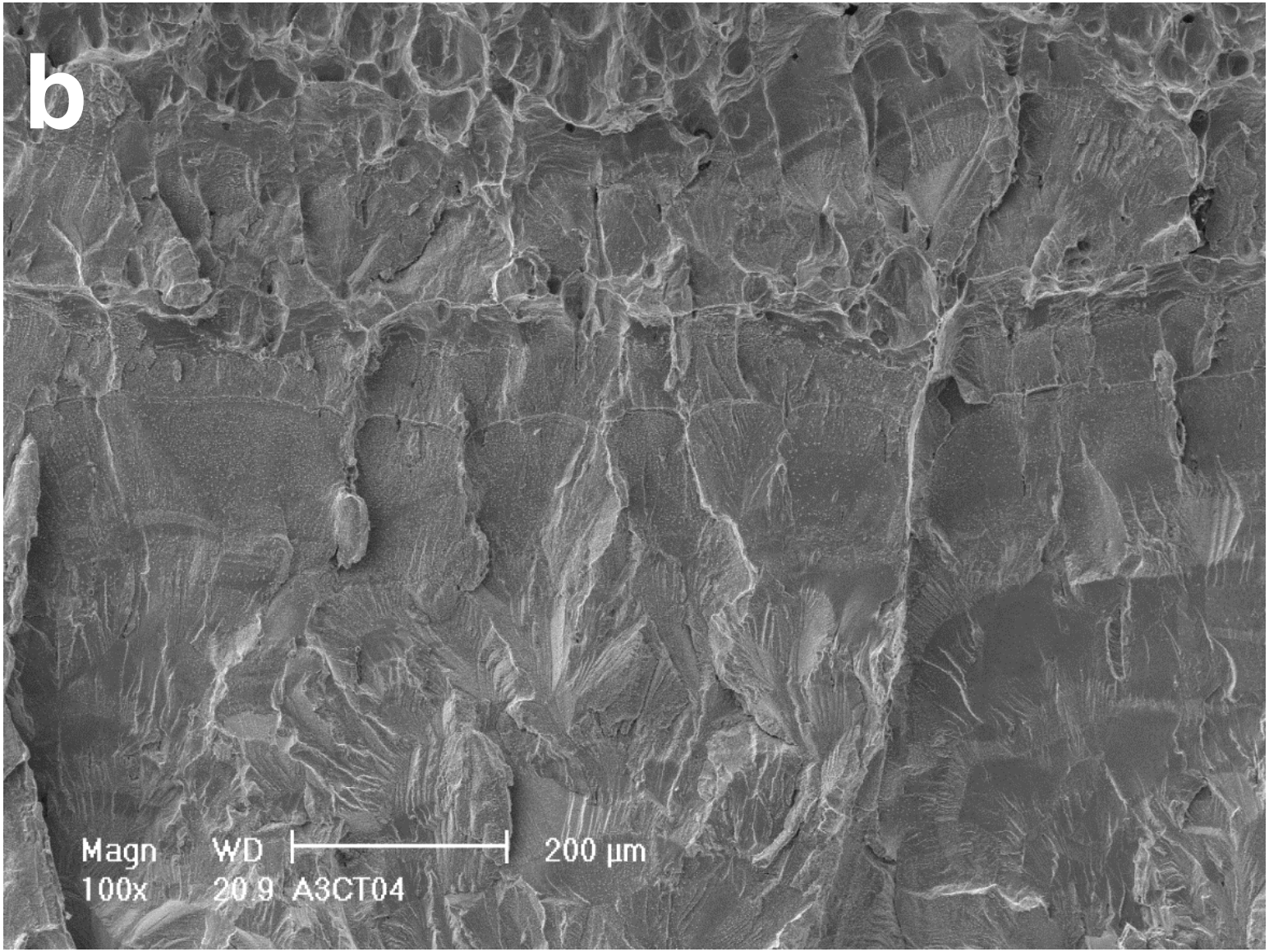

Figure 11. (Cont.)

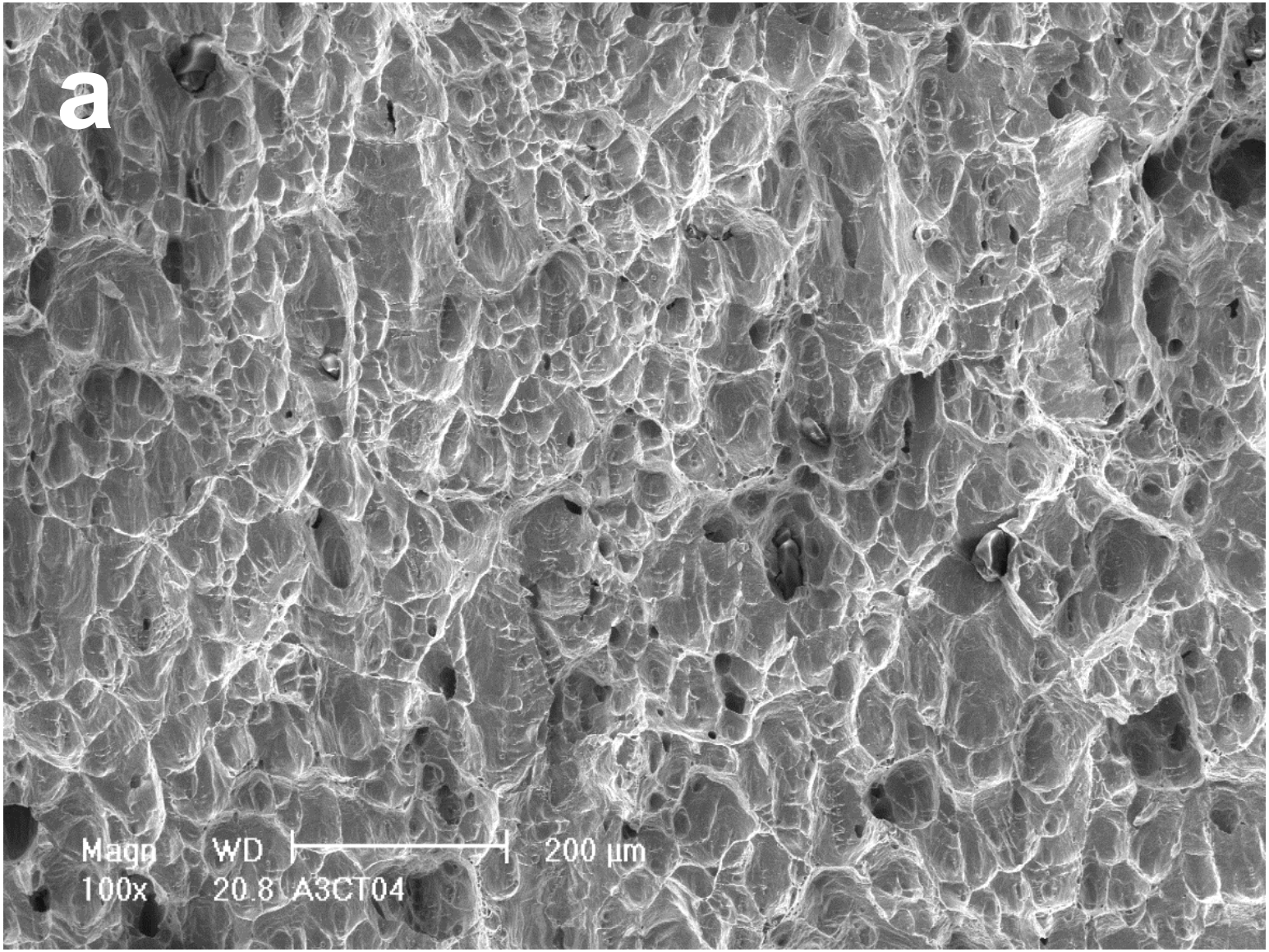

Figure 12. Mostly ductile morphology with a brittle stringer in the J-R curve test of Specimen A3CT04

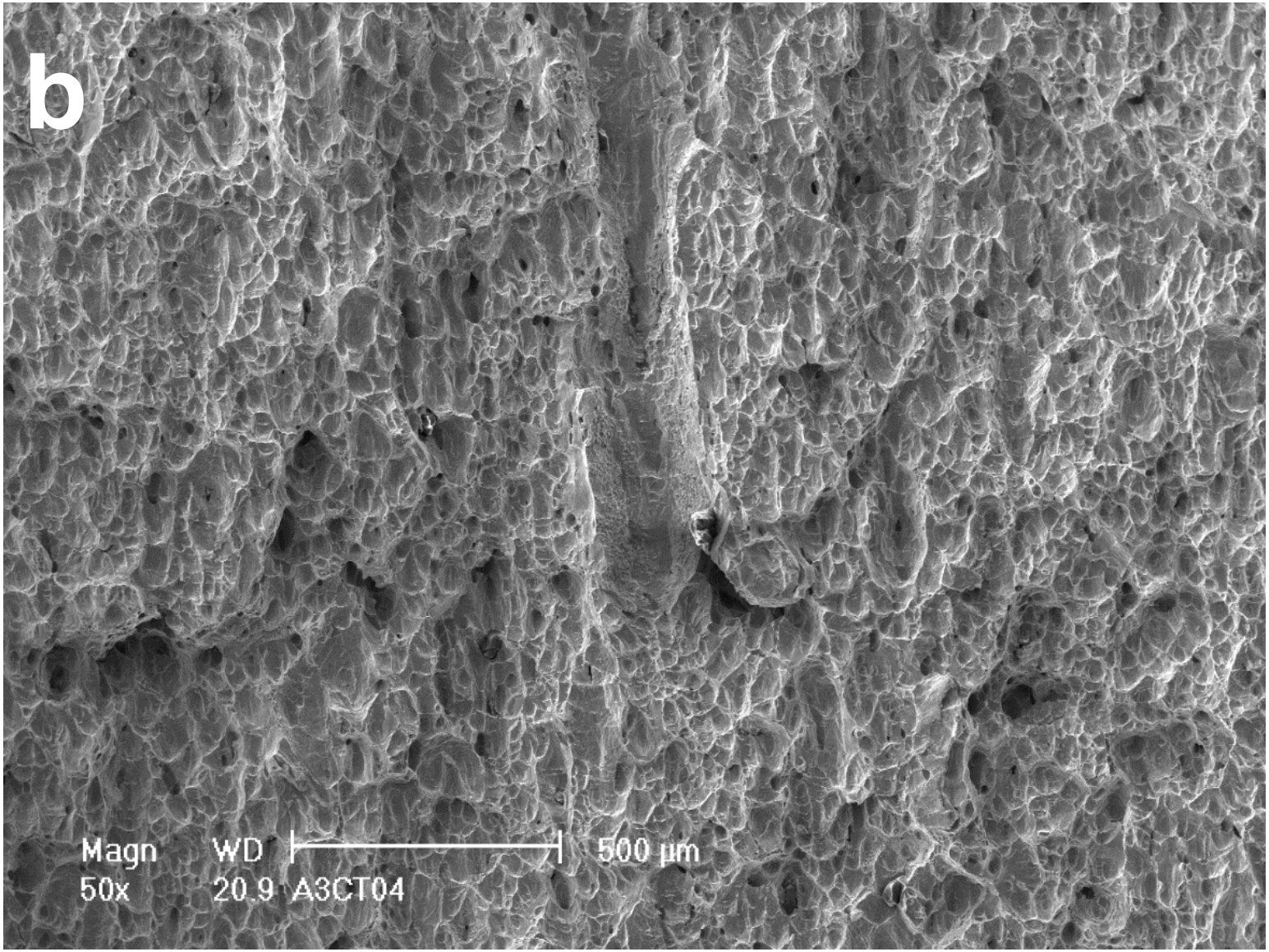

Figure 12. (Cont.)

4.2 Specimen B3CT14, ~8 dpa

Specimen B3CT14 was cut from the source material "B3," a concave corner of the reactor core baffle. The thickness of "B3" was about 29 mm, and specimen B3CT14 was machined from the side of the plate farther away from the core [10]. The displacement damage for this sample is about 8.1 dpa, based on the dose calculation (see Table 1). Visual examination of the machined sample prior to the test revealed that the initial notch size was somewhat lower than specified. Because the actual crack size is verified with SEM images after the test, this low notch size is not critical for the CGR or J-R curve test.

4.2.1 Crack Growth Rates

After the sample was installed in the autoclave, the system was pressurized to ~1,800 psig, and heated slowly to ~315°C. A tensile load of about 30 lb. was maintained on the sample during the heating. The sample was soaked in the low-DO, high-purity water for 12 days to stabilize the test condition.

The test started with cyclic loading at a K_{max} of ~12.7 MPa $m^{1/2}$ and a load ratio of 0.32 and 0.5 Hz. Figure 13 shows the time history plots for the crack length and applied K for this test. No significant crack advance was observed in this sample until the K_{max} increased to ~15.8 MPa $m^{1/2}$. A cyclic CGR comparable to that of fatigue growth rate in air was obtained after ~330 μm crack extension. As the rise time and load ratio increased, the measured CGRs declined as expected, but quickly fell below the fatigue line when the load ratio was close to 0.5. After the crack was re-activated with a K_{max} of ~16.4 MPa $m^{1/2}$, environmentally enhanced cracking started to appear in this sample with a load ratio below 0.45. Figure 14 shows the cyclic CGRs as a function of fatigue growth rate in air under the same loading conditions. After the environmental enhancement was stabilized, the test was set to a constant K with PPU every 2 hours. A SCC CGR of 2.4×10^{-11} m/s was recorded over ~100 hours. After the PPU was removed, the measured CGR decreased to about 1.5×10^{-11} m/s.

Next, the crack was advanced under cyclic loading with a K_{max} of ~21.3 MPa $m^{1/2}$. The degree of environmental enhancement remained the same as in Figure 14. After about 146 μm crack extension, the test was set again to a constant K with PPU every 2 hours. A SCC CGR of 2.9×10^{-11} m/s was obtained over ~110 hours. After the PPU was removed, the CGR decreased slightly to 1.9×10^{-11} m/s. Immediately after the constant-K test, a cyclic load test period was performed with a K_{max} of ~21.5 MPa $m^{1/2}$. In contrast to the cracking instability in the 0.06-dpa sample, no jump in crack length was observed in this sample (see Figure 13h). This confirms that no unbroken ligament developed during the constant-K test period.

The crack was advanced once again with cyclic loading at a K_{max} of ~26.5 MPa $m^{1/2}$. No stepwise increase in crack length was observed with the increase in K_{max}. The environmentally enhanced cracking remained stable, and the degree of the enhancement was about the same as that observed at the lower K_{max} levels (see Figure 14). After ~200 μm crack extension, the sample was once again set to a constant K with PPU. A SCC CGR of 1.7×10^{-11} m/s was measured over 120 hours. After the PPU was removed, the CGR dropped to 1.3×10^{-11} m/s. Before the CGR test was terminated, a brief cyclic test period was also conducted with a K_{max} of ~26.7 MPa $m^{1/2}$. Again, no stepwise increase in crack length was observed (see Figure 13i). All test conditions and CGR results from this sample are summarized in Table 4.

Table 4. Crack growth rates of Specimen B3CT14 (~8 dpa) in low-DO, high-purity water

Test Period [1]	Test Time (hr)	Test Temp. (°C)	Load Ratio	Rise Time (s)	Return Time (s)	Hold Time (s)	K_{max} (MPa $m^{1/2}$)	ΔK (MPa $m^{1/2}$)	CGR in Env. (m/s)	CGR in Air (m/s)	Crack Length (mm)
Start	2.0										5.670
a	9.4	313	0.32	0.9	0.9	0.1	12.7	8.7	negligible	8.09E-09	5.667
b	12.6	313	0.32	0.9	0.9	0.1	13.7	9.3	negligible	1.02E-08	5.673
c	27.8	313	0.32	0.9	0.9	0.1	14.3	9.7	5.18E-10	1.17E-08	5.681
d	34.9	313	0.32	0.9	0.9	0.1	14.8	10.2	2.69E-09	1.34E-08	5.708
e [2]	59.7	313	0.32	0.9	0.9	0.1	15.8	10.8	2.90E-08	1.63E-08	6.033
f	75.5	313	0.39	4.4	4.4	0.6	16.0	9.7	3.68E-09	2.56E-09	6.135
g	97.3	313	0.48	8.5	4.3	1.4	15.8	8.1	4.21E-10	8.04E-10	6.158
h	123.4	313	0.48	25.7	4.3	4.3	15.8	8.2	1.48E-10	2.76E-10	6.160
i	148.3	313	0.47	51.5	10.3	8.5	15.9	8.5	7.95E-11	1.49E-10	6.175
j	165.0	313	0.45	103.5	10.4	16.5	15.9	8.7	negligible	8.10E-11	6.174
k	189.7	314	0.43	43.3	10.4	6.7	15.8	8.9	5.67E-11	2.05E-10	6.168
l	213.3	313	0.44	26.0	10.4	4.0	16.4	9.2	5.23E-10	3.79E-10	6.194
m	237.1	313	0.44	52.1	10.4	7.9	16.6	9.4	3.00E-10	1.98E-10	6.223
n	262.5	313	0.43	104.4	10.4	15.6	16.6	9.5	2.31E-10	1.02E-10	6.242
o	289.2	313	0.43	217.4	10.4	32.6	16.6	9.5	1.05E-10	4.92E-11	6.246
p	308.6	314	0.43	435.0	10.4	65.0	16.7	9.5	1.13E-10	2.50E-11	6.252
q	333.0	313	0.43	871.4	10.5	128.6	16.8	9.7	9.75E-11	1.31E-11	6.263
1	429.3	312	0.45	12	12	7200	16.9	9.3	2.43E-11	1.43E-12	6.286
2	524.7	312	1	-	-	-	17.2	-	1.47E-11	-	6.291
r	548.7	312	0.58	51.1	10.2	8.8	20.3	8.5	1.05E-09	1.67E-10	6.365
s	574.9	312	0.56	107.7	10.3	17.3	21.0	9.2	4.20E-10	1.03E-10	6.396
t	600.0	313	0.55	215.7	10.4	34.3	20.9	9.3	2.69E-10	5.31E-11	6.410
u	626.6	312	0.55	431.9	10.4	68.1	21.0	9.4	2.28E-10	2.75E-11	6.423
v	651.2	312	0.55	862.6	10.4	137.4	21.1	9.4	1.30E-10	1.35E-11	6.437
3	763.8	312	0.57	12	12	7200	21.2	9.1	2.86E-11	1.49E-12	6.454
4	866.4	312	1	-	-	-	21.2	-	1.78E-11	-	6.458
w	884.8	312	0.56	51.7	10.3	8.3	21.5	9.5	1.52E-09	2.36E-10	6.526
x	909.9	312	0.64	51.5	10.3	8.5	26.4	9.4	9.74E-10	2.49E-10	6.582
y	934.7	312	0.64	107.4	10.3	17.6	26.6	9.6	4.46E-10	1.25E-10	6.611
z	958.5	312	0.64	214.7	10.3	35.3	26.6	9.6	3.10E-10	6.34E-11	6.635
aa	982.4	312	0.63	430.7	10.3	69.3	26.8	9.9	1.69E-10	3.41E-11	6.646
ab	1,005.9	311	0.66	847.6	10.2	152.4	26.4	8.8	1.27E-10	1.24E-11	6.655
5	1,126.3	311	0.65	12	12	7200	27.0	9.4	1.71E-11	1.79E-12	6.660
6	1,222.9	311	1	-	-	-	27.0	-	1.27E-11	-	6.671
ac	1,225.9	311	0.58	87.5	10.5	12.51	26.7	11.2	1.75E-09	2.44E-10	6.677
Complete											

[1] Cyclic test periods are named in alphabetical order, and constant-K test periods are named in numerical order.
[2] Crack growth rate in the later part of the test period is reported.

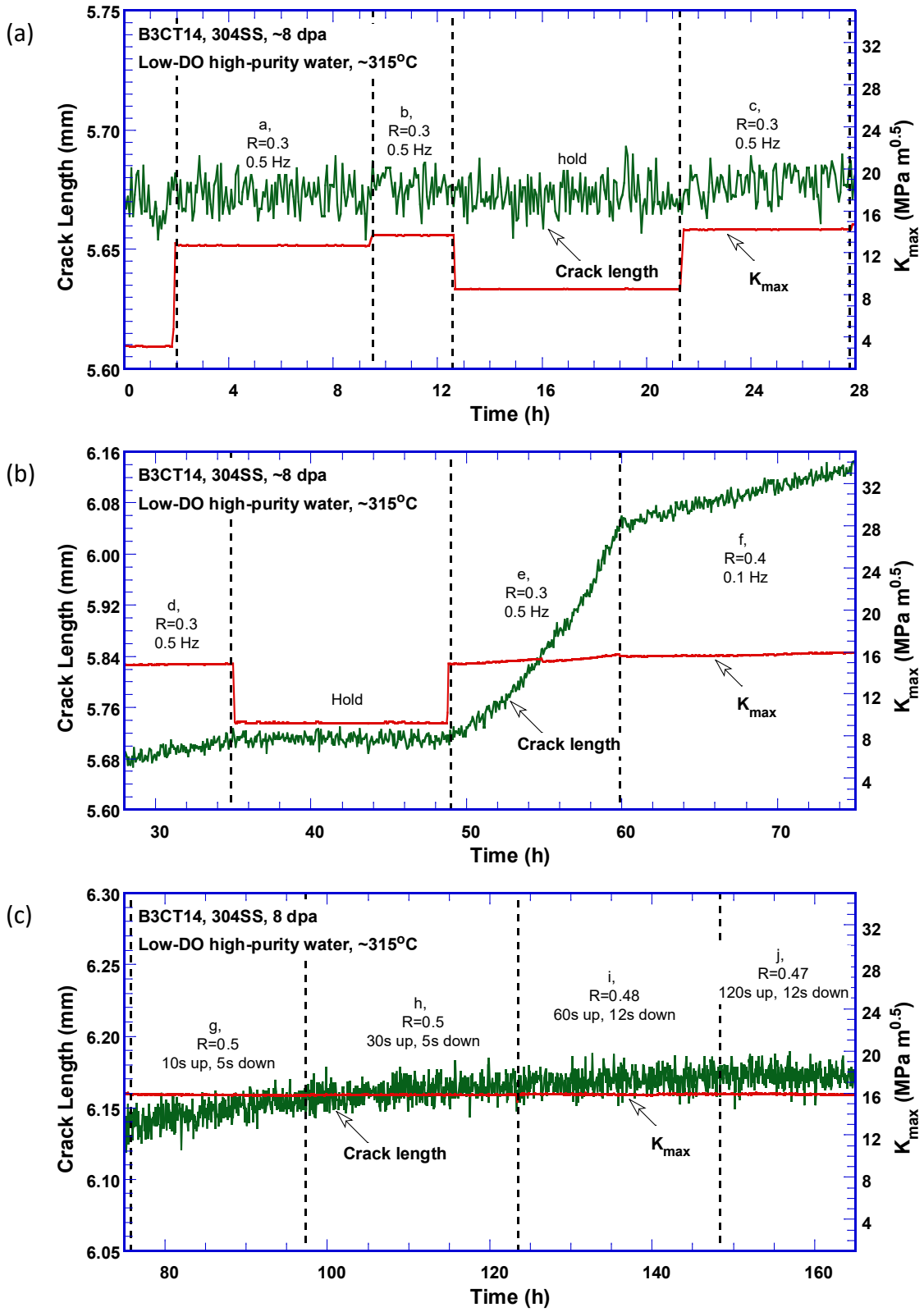

Figure 13. Crack-length-vs.-time plot of Specimen B3CT14 (~8 dpa) tested in low-DO high-purity water: test periods (a) a–c, (b) d–f, (c) g–i, (d) k–n, (e) o–q, (f) 1–2, (g) r–v, (h) x–ab, and (i) 5–6

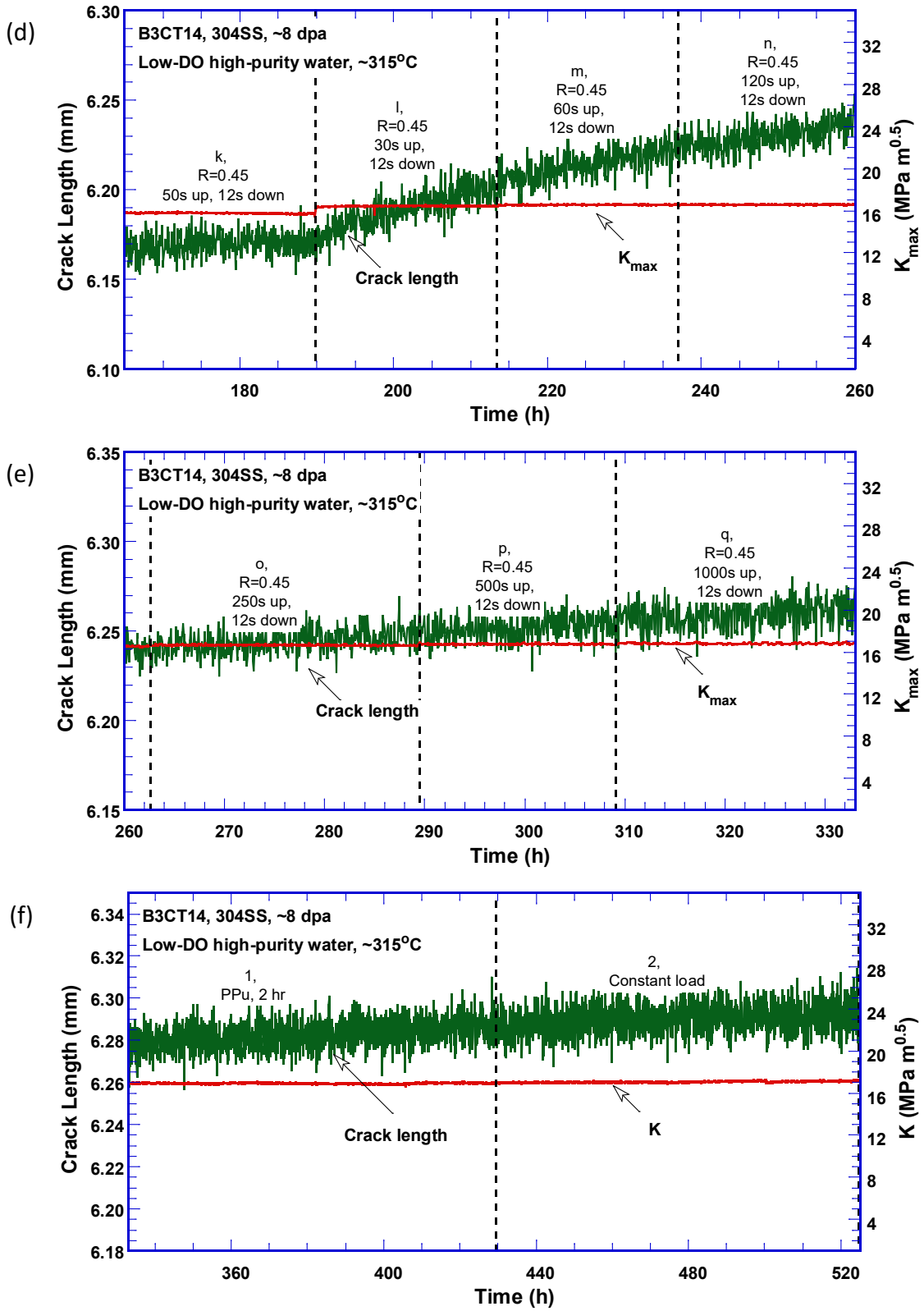

Figure 13. (Cont.)

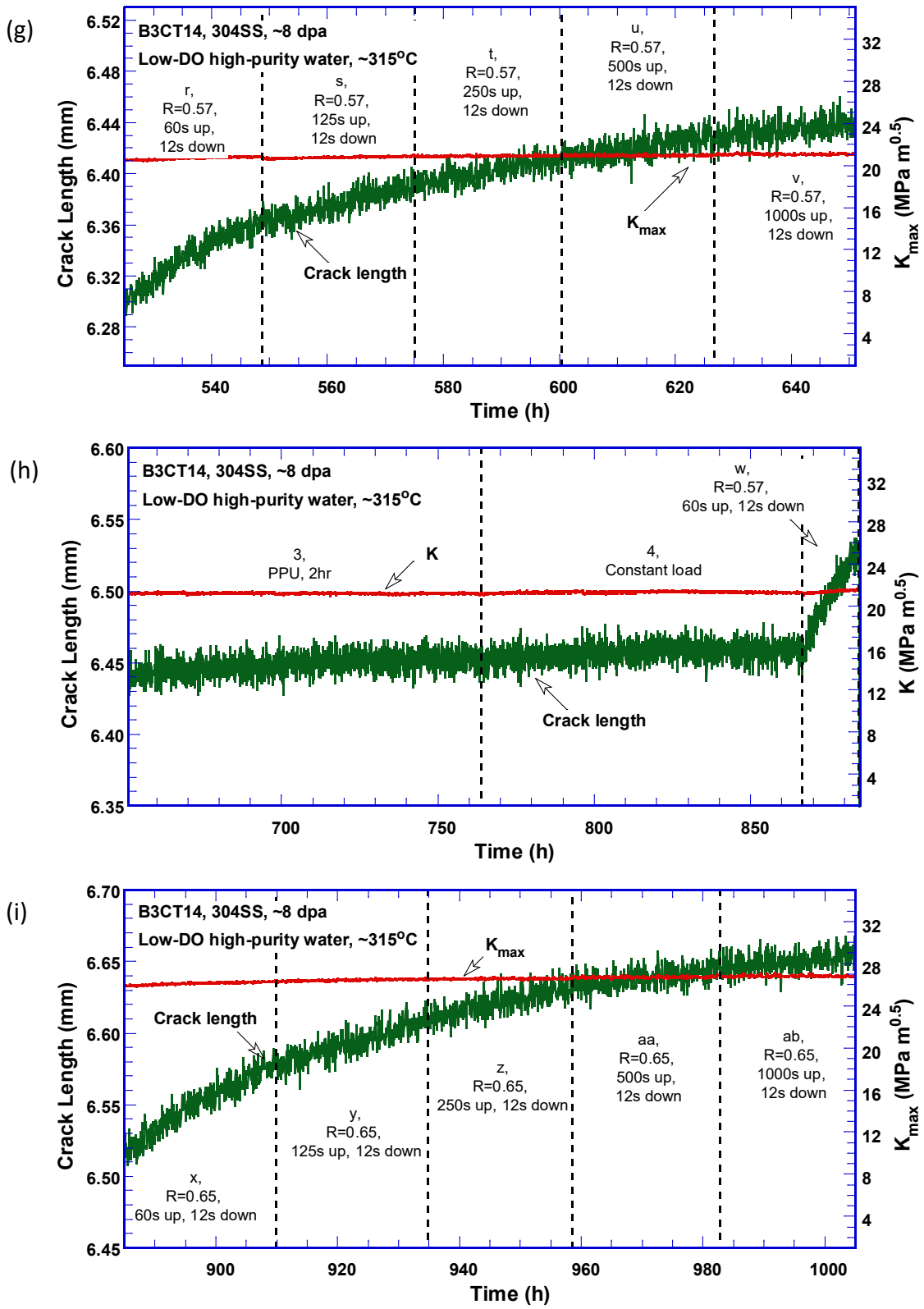

Figure 13. (Cont.)

(j)

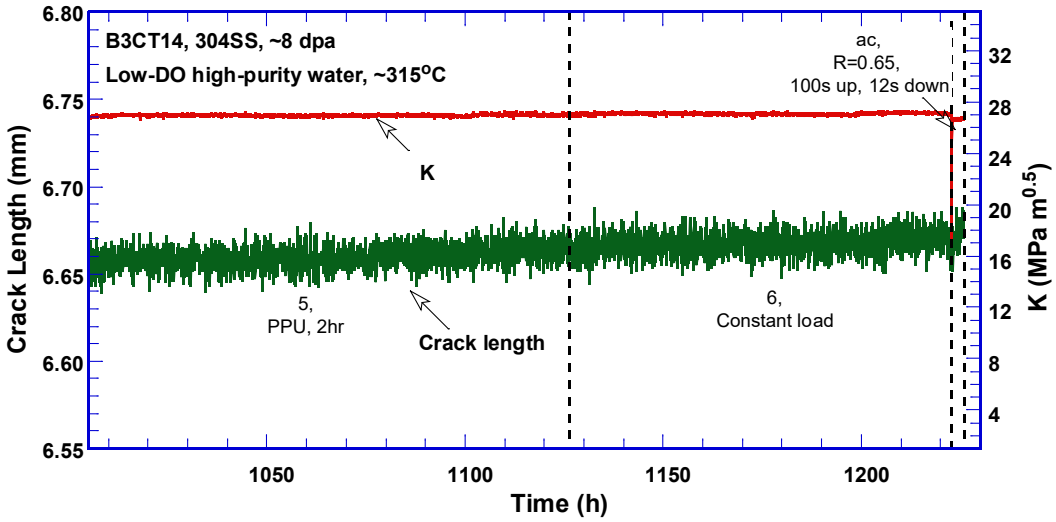

Figure 13. (Cont.)

The cyclic CGRs are plotted in Figure 14 as a function of fatigue growth rate in air. Compared with the 0.06-dpa sample, the cracking seems more difficult to initiate in this 8-dpa specimen. The crack growth stalled several times during the cyclic test, resulting in several data points below the diagonal line in Figure 14. Environmental enhancement was also more difficult to establish in this sample. Once started, however, the degree of enhancement remained stable.

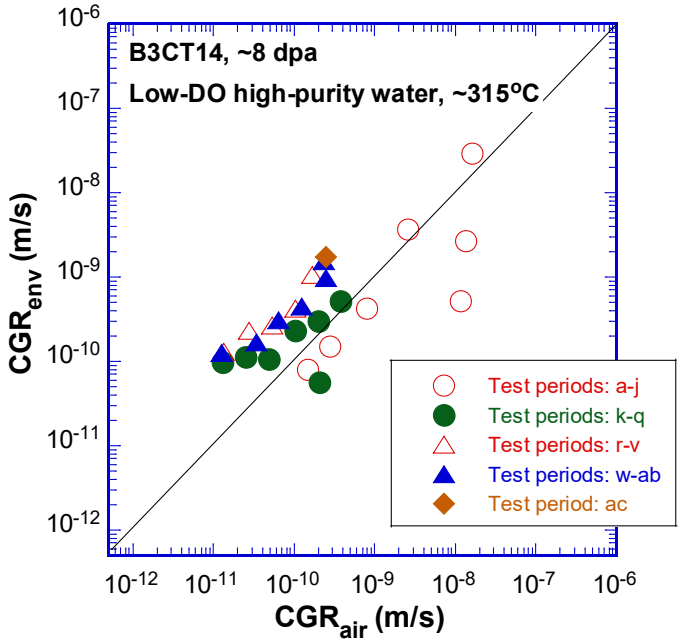

Figure 14. Cyclic CGRs of Specimen B3CT14 (~8 dpa) tested in low-DO, high-purity water

All SCC CGRs of this sample are below the NUREG-0313 curve, as shown in Figure 15. Although the CGRs with PPU are similar to those of the 0.06-dpa sample, the CGRs without PPU are slightly higher. No K dependence can be seen between 17 and 27 MPa $m^{1/2}$ in this sample.

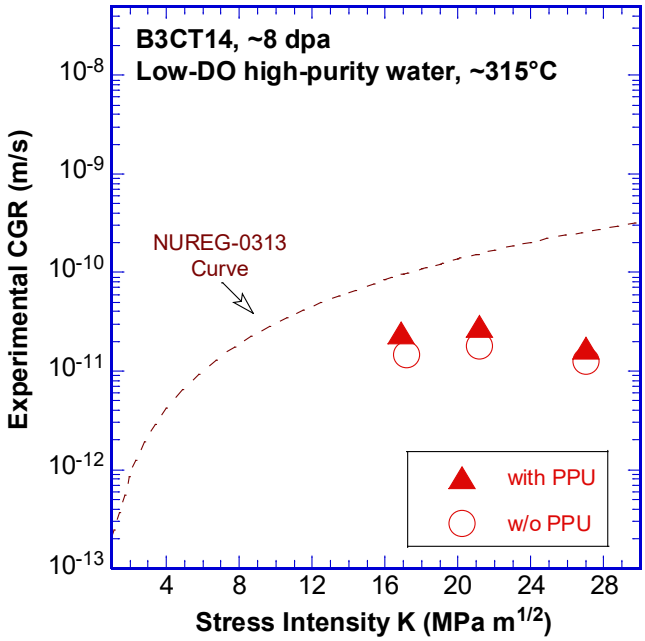

Figure 15. SCC CGRs of Specimen B3CT14 (~8 dpa) tested in low-DO, high-purity water

4.2.2 Fracture Toughness J-R Curve

After the CGR test, a fracture toughness J-R curve test was conducted on the same sample in the test environment. The ratio of a/W for the starter crack was about 0.56. The obtained J-Δa data are shown in Figure 16. The Δa_{max} can be measured with this sample is also included in the figure. The J_{max} value is more than 410 kJ/m^2, significantly higher than the J-R curve shown in the figure. The obtained J-Δa data are fitted to a power-law relationship, $J = 113 \times \Delta a^{0.07}$. Note that because only one data point is between the exclusion lines, data outside the validated crack extension region are included for the curve fitting. The J-R curve intercepts the 0.2-mm offset line at 103 kJ/m^2, similar to that obtained at 0.06 dpa. However, the power exponent of the J-R curve of this sample is much lower, indicating severe embrittlement at this dose level.

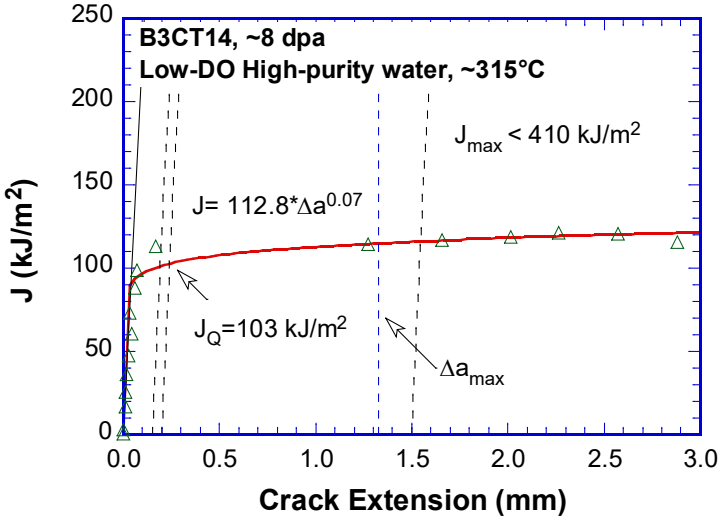

Figure 16. J-R curve of Specimen B3CT14 (~8 dpa) tested at ~315°C

4.2.3 Fracture Morphology

After the J-R curve test, the sample was broken open under fatigue cyclic loading in air at room temperature. Several replicas were produced from the fracture surface and examined under a SEM. The curing of the replica material was not very successful, and some details of the fracture surface around the edges were not captured. Figure 17 shows the center of the fracture surface, and the cracking direction is from bottom to top. The initial fracture morphology during the cyclic loading was TG, as shown in Figure 18a. Some crystallographic facets can be seen from the very beginning of the test. As the crack advanced into the SCC region, the morphology became fully intergranular (IG) as shown in Figure 18b. The J-R test region shows a dimple fracture (Figure 19) similar to that in the 0.06-dpa specimen. Finally, the post-JR fatigue region shows a mixed mode of IG and dimple fracture, as illustrated in Figure 20. The IG cracking in the post-JR region is unexpected, and is different from that observed in the 0.06-dpa sample.

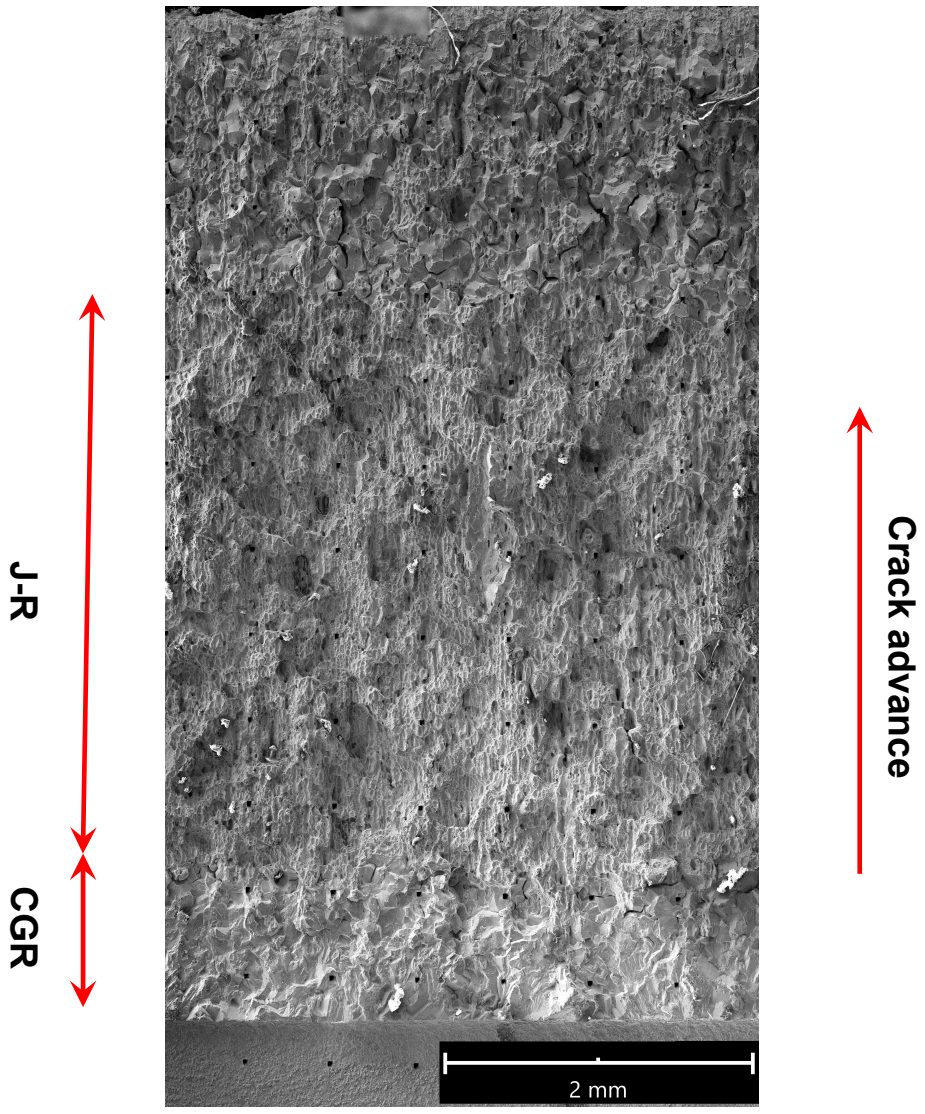

Figure 17. Fracture surface of Specimen B3CT14, ~8 dpa

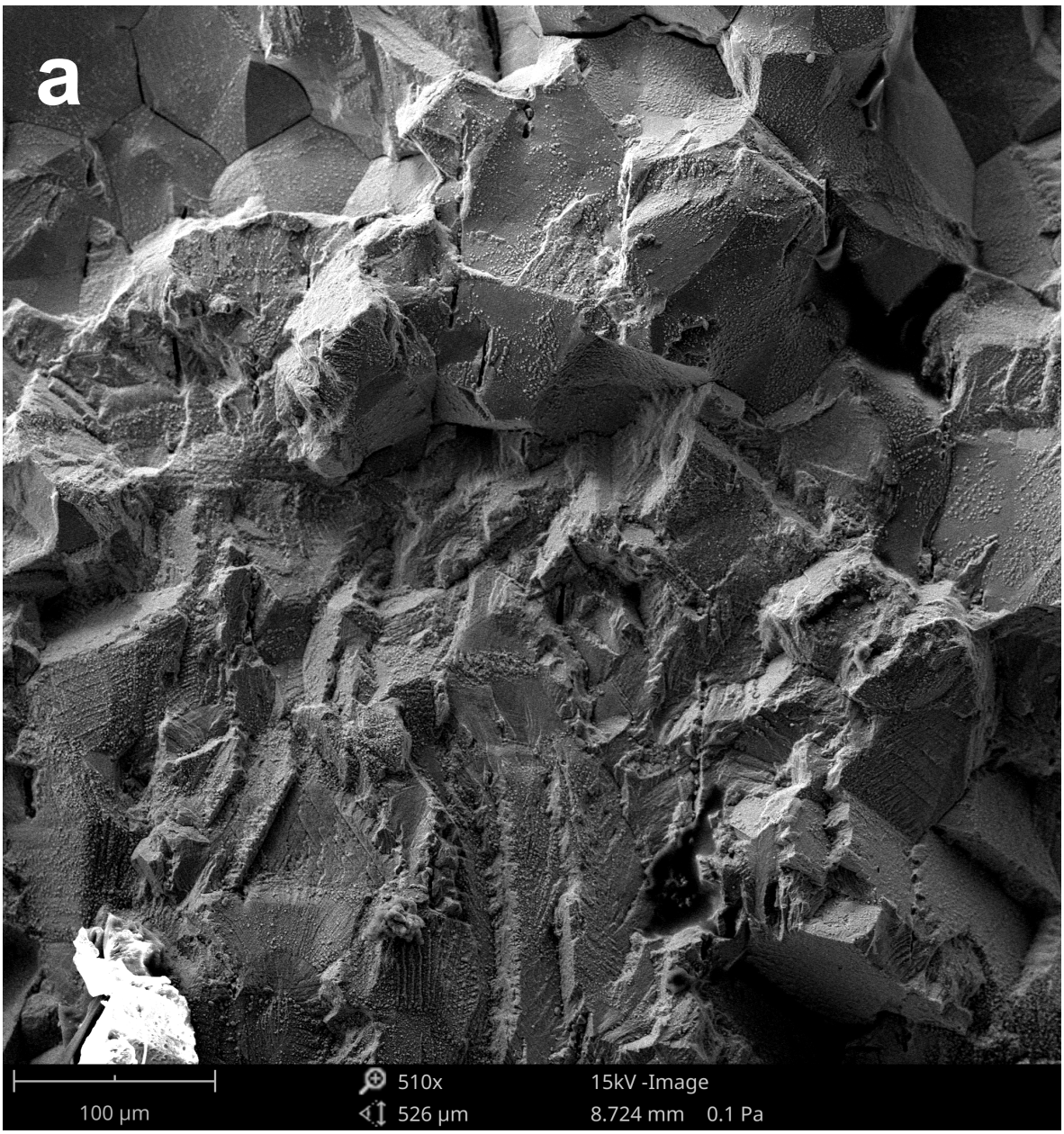

Figure 18. Fracture morphology in Specimen B3CT14: (a) initial CGR test region, and (b) IG cracking at the end of the CGR test

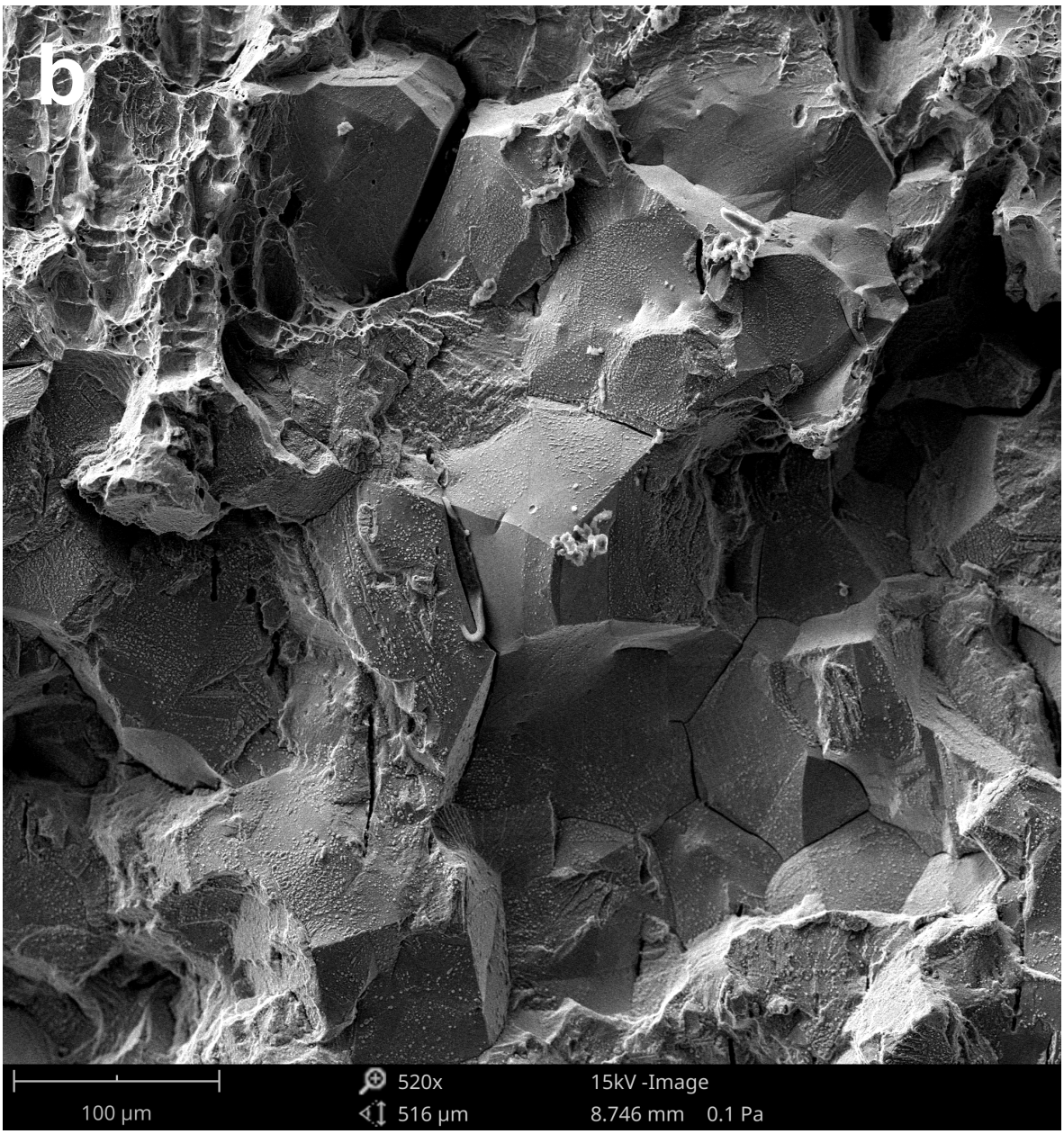

Figure 18 (Cont.)

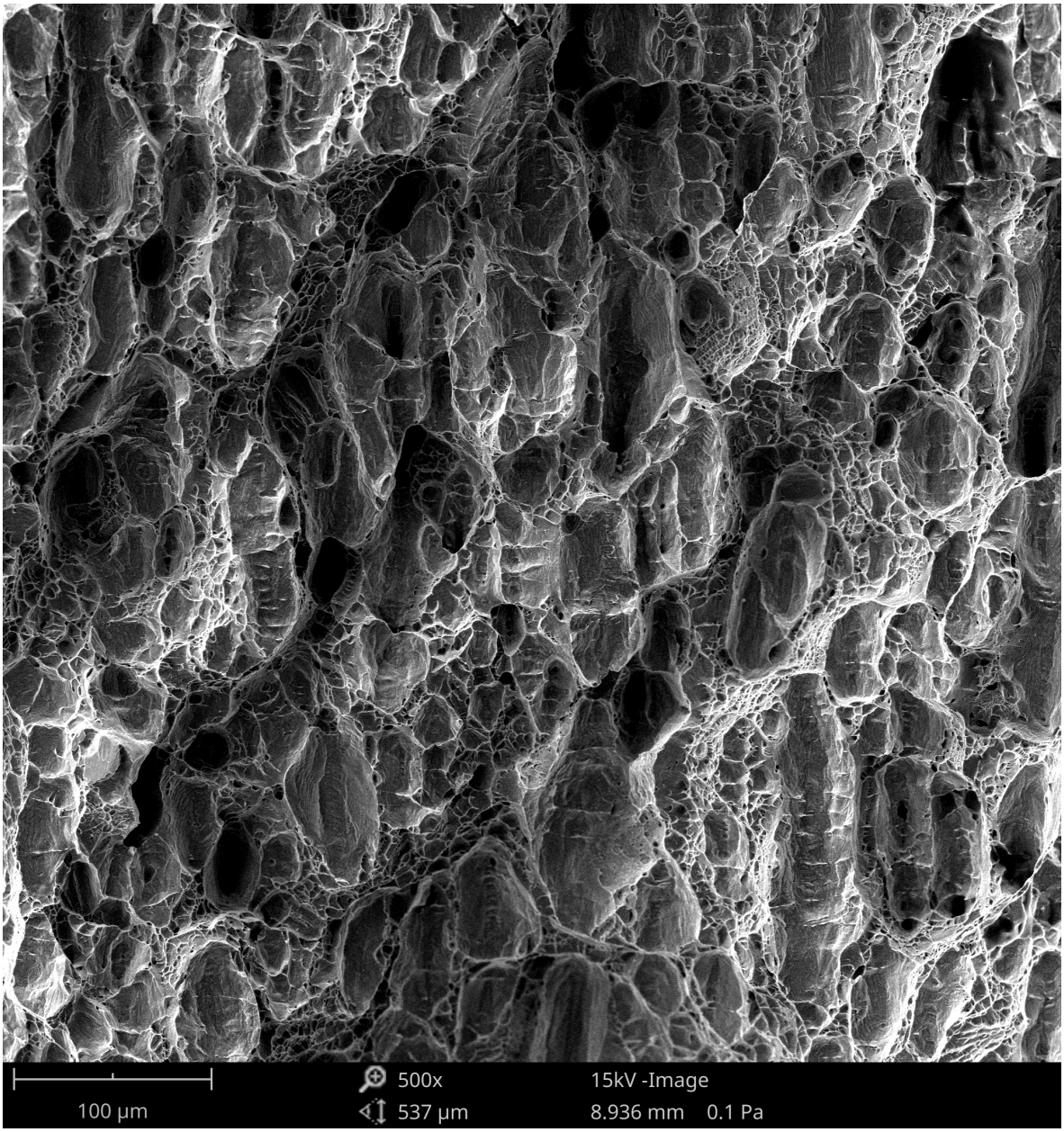

Figure 19. Dimple fracture during the JR curve test of Specimen B3CT14

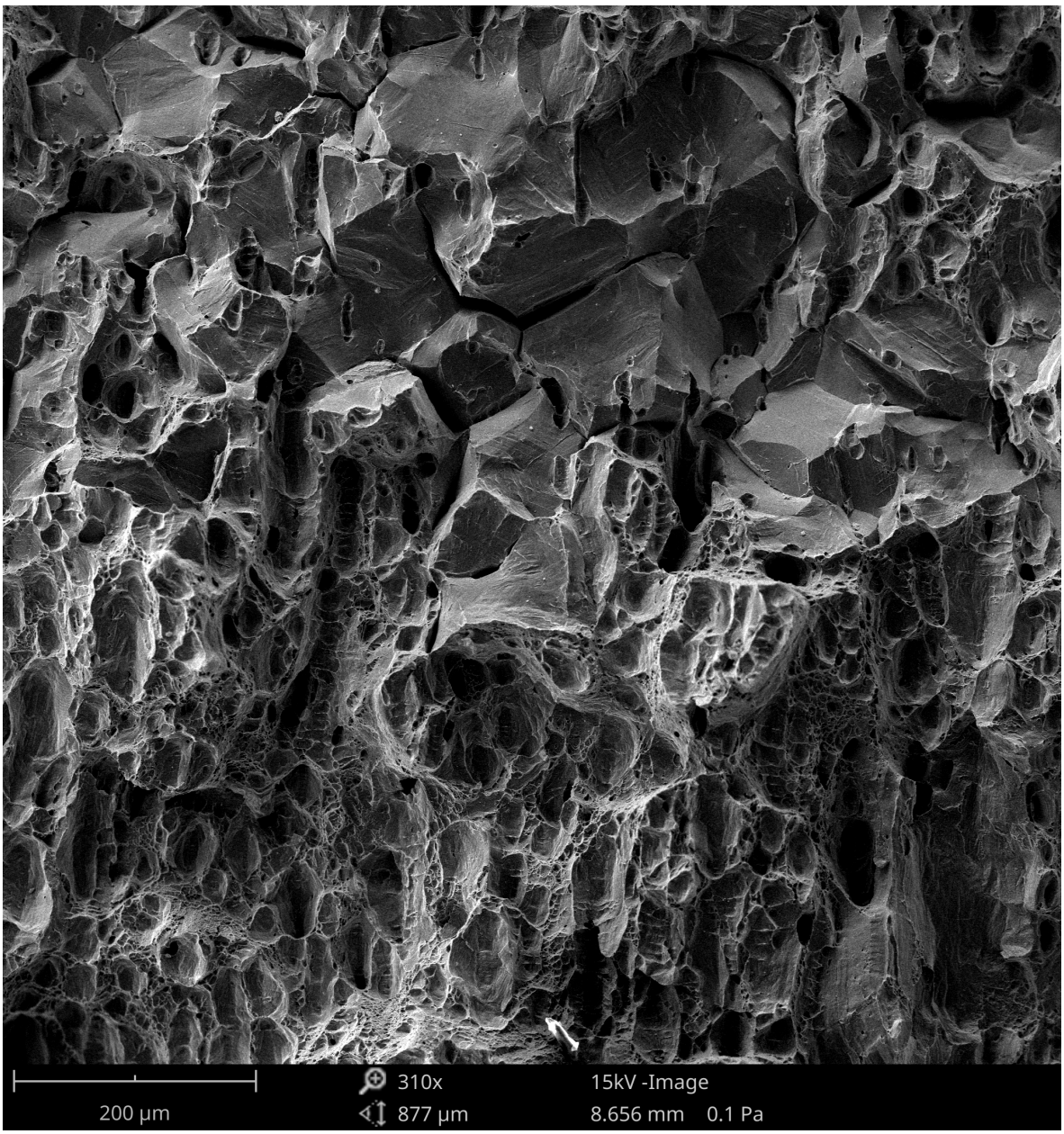

Figure 20. Mix of IG and dimple fracture in Specimen B3CT14 resulting from the post-test fatigue loading in air at room temperature

4.3 Specimen ACT03, ~15 dpa

Specimen ACT03 was cut from the source material "A," a baffle plate facing the reactor core. The plate was 29 mm thick, and the sample was machined from its outside surface. The average damage dose for this sample was about 15.3 dpa according to the dose calculation [1].

4.3.1 Crack growth rates

The CGR tests on this sample were performed in low-DO, high-purity water. After the specimen was loaded into the autoclave, the system was pressurized and heated slowly under a constant tensile load of ~25 lb. Prior to the start of the test, the sample was soaked in the test environment for 5 days to stabilize its condition. All CGR results obtained from this sample are summarized in Table 5.

Figure 21 shows the time history of crack length and applied K for this sample. Cyclic loading started with a triangle waveform at 0.5 Hz and a K_{max} of ~14 MPa $m^{1/2}$. This initial K_{max} appeared to be too low for this sample, and no substantial crack growth was observed until K_{max} increased to ~15.5 MPa $m^{1/2}$. After ~200 μm crack extension, the load ratio and rise time were gradually increased to encourage the development of environmental enhancement. After repeated attempts, a CGR slightly below the fatigue growth rate was obtained with a K_{max} of ~16 MPa $m^{1/2}$ and a load ratio of ~0.5. With some further increases in the rise time, the environmental enhancement stabilized and the measured CGR was about a factor of 8 higher than that of the expected fatigue growth rate in air. The test was then set to a constant K of ~16.4 MPa $m^{1/2}$ with a PPU every 2 hours. A SCC CGR of 1.0×10^{-11} m/s was measured over 5 μm crack extension. After the PPU was removed, the CGR only decreased slightly, to 9.6×10^{-12} m/s.

Next, the sample was cyclically loaded again to advance the crack front for another measurement at a K_{max} of ~20 MPa $m^{1/2}$. No jump in crack length was observed when the load was increased (see Figure 21g). The environmental effect appeared to be stronger, as shown in Figure 22. After a total of ~75 μm crack extension, the test was transitioned to a constant-K test with PPU every 2 hours. A CGR of 1.4×10^{-12} m/s was recorded over ~100 hours. After the PPU was removed, the CGR declined to about 5.9×10^{-12} m/s.

After the SCC CGR measurement at ~20 MPa $m^{1/2}$, the K was increased once again to about 26 MPa $m^{1/2}$ with cyclic loading. Again, no jump in the crack length history plot was observed, and the environmental enhancement remained strong as shown in Figure 22. After ~130 μm crack extension, the test was set to a constant K with PPU every 2 hours. A SCC CGR of 3.7×10^{-11} m/s was recorded over ~130 hours. After the PPU was removed, a slightly lower CGR of 2.5×10^{-11} m/s was registered over ~120 hours. The CGR test then concluded and the sample was prepared for a J-R curve test.

Table 5. Crack growth rates of Specimen ACT03 (~15 dpa) in low-DO, high-purity water

Test Period [1]	Test Time (hr)	Test Temp. (°C)	Load Ratio	Rise Time (s)	Return Time (s)	Hold Time (s)	K_{max} (MPa $m^{1/2}$)	ΔK (MPa $m^{1/2}$)	CGR in Env. (m/s)	CGR in Air (m/s)	Crack Length (mm)
Start	2.0										5.640
a	6.7	314	0.24	0.8	0.8	0.2	13.8	10.5	1.84E-11	1.54E-08	5.644
b	21.8	314	0.24	7.8	7.8	2.2	13.9	10.5	negligible	1.57E-09	5.639
c	29.9	314	0.24	0.8	0.8	0.2	14.2	10.9	2.10E-10	1.72E-08	5.645
d	45.1	314	0.24	7.9	7.9	2.1	14.2	10.8	negligible	1.71E-09	5.641
e	55.3	314	0.35	0.8	0.8	0.2	14.7	9.6	4.89E-10	1.33E-08	5.653
f	68.7	314	0.35	3.8	3.8	1.2	14.6	9.6	negligible	2.66E-09	5.652
g	81.1	314	0.35	0.4	0.4	0.1	15.0	9.8	2.08E-09	2.85E-08	5.685
h	95.4	314	0.34	1.9	1.9	0.6	15.0	9.8	1.03E-09	5.80E-09	5.707
i	105.8	314	0.35	0.8	0.8	0.2	15.2	9.9	2.52E-09	1.50E-08	5.747
j	117.8	314	0.34	1.5	1.5	0.5	15.5	10.2	5.23E-09	8.05E-09	5.834
k [2]	126.2	314	0.35	0.8	0.8	0.2	15.6	10.2	2.22E-08	1.65E-08	6.002
l	141.4	314	0.45	3.6	3.6	1.4	15.1	8.3	5.56E-10	1.95E-09	6.026
m [2]	165.0	314	0.45	1.4	1.4	0.6	15.5	8.5	7.06E-09	5.37E-09	6.186
n	189.3	314	0.51	3.5	3.5	1.5	15.4	7.6	1.05E-09	1.61E-09	6.220
o	197.9	314	0.51	1.7	1.7	0.8	15.5	7.6	2.19E-09	3.25E-09	6.246
p	236.9	314	0.51	3.4	3.4	1.6	15.4	7.6	1.01E-09	1.63E-09	6.296
q	296.9	314	0.54	6.7	3.4	3.3	15.6	7.1	2.06E-10	6.88E-10	6.320
r	314.0	314	0.55	6.7	3.4	3.3	15.8	7.2	2.83E-10	7.10E-10	6.329
s	335.9	314	0.55	3.4	3.4	1.6	16.0	7.3	7.93E-10	1.49E-09	6.351
t	363.8	314	0.54	20.4	3.4	9.6	16.1	7.4	1.92E-10	2.64E-10	6.365
u	406.0	314	0.53	40.9	3.4	19.1	16.2	7.6	1.81E-10	1.39E-10	6.380
v	436.5	314	0.54	101.6	8.1	48.4	16.2	7.5	1.84E-10	5.35E-11	6.395
w	477.2	314	0.53	204.4	8.2	95.6	16.2	7.6	1.26E-10	2.81E-11	6.405
x	525.3	314	0.53	340.7	8.2	159.3	16.1	7.6	9.96E-11	1.70E-11	6.416
y	551.2	314	0.52	686.8	8.2	313.2	16.4	7.8	7.13E-11	9.17E-12	6.419
1	623.7	313	0.50	12.0	12.0	7200	16.4	8.2	9.95E-12	9.95E-13	6.426
2	717.0	313	1	-	-	-	16.4	-	9.59E-12	-	6.434
z	741.1	314	0.61	68.3	8.2	31.7	20.1	7.8	6.11E-10	9.90E-11	6.470
aa	765.9	313	0.60	172.4	8.3	77.6	20.4	8.1	3.01E-10	4.37E-11	6.489
ab	787.8	314	0.61	342.2	8.2	157.8	20.3	7.9	1.94E-10	2.06E-11	6.498
ac	813.0	314	0.60	690.6	8.3	309.4	20.4	8.2	1.72E-10	1.13E-11	6.510
3	917.4	314	0.58	12.0	12.0	7200	20.7	8.7	1.35E-11	1.29E-12	6.514
4	1,175.8	314	1	-	-	-	20.7	-	5.87E-12	-	6.524
ad	1,196.9	314	0.69	68.3	8.2	31.7	25.9	8.0	1.02E-09	1.16E-10	6.570
ae	1,221.7	314	0.69	136.9	8.2	63.1	26.1	8.2	5.15E-10	6.07E-11	6.600
af	1,251.7	315	0.68	344.3	8.3	155.7	26.3	8.4	3.07E-10	2.62E-11	6.621
ag	1,317.6	316	0.68	687.0	8.2	313.0	26.5	8.4	2.19E-10	1.33E-11	6.657
5	1,447.9	315	0.66	12	12	7200	26.5	9.0	3.74E-11	1.57E-12	6.678
6	1,581.2	316	1	-	-	-	26.9	-	2.25E-11	-	6.691
Complete											

[1] Cyclic test periods are named in alphabetical order, and constant-K test periods are named in numerical order.
[2] Crack growth rate in the later part of the test period is reported.

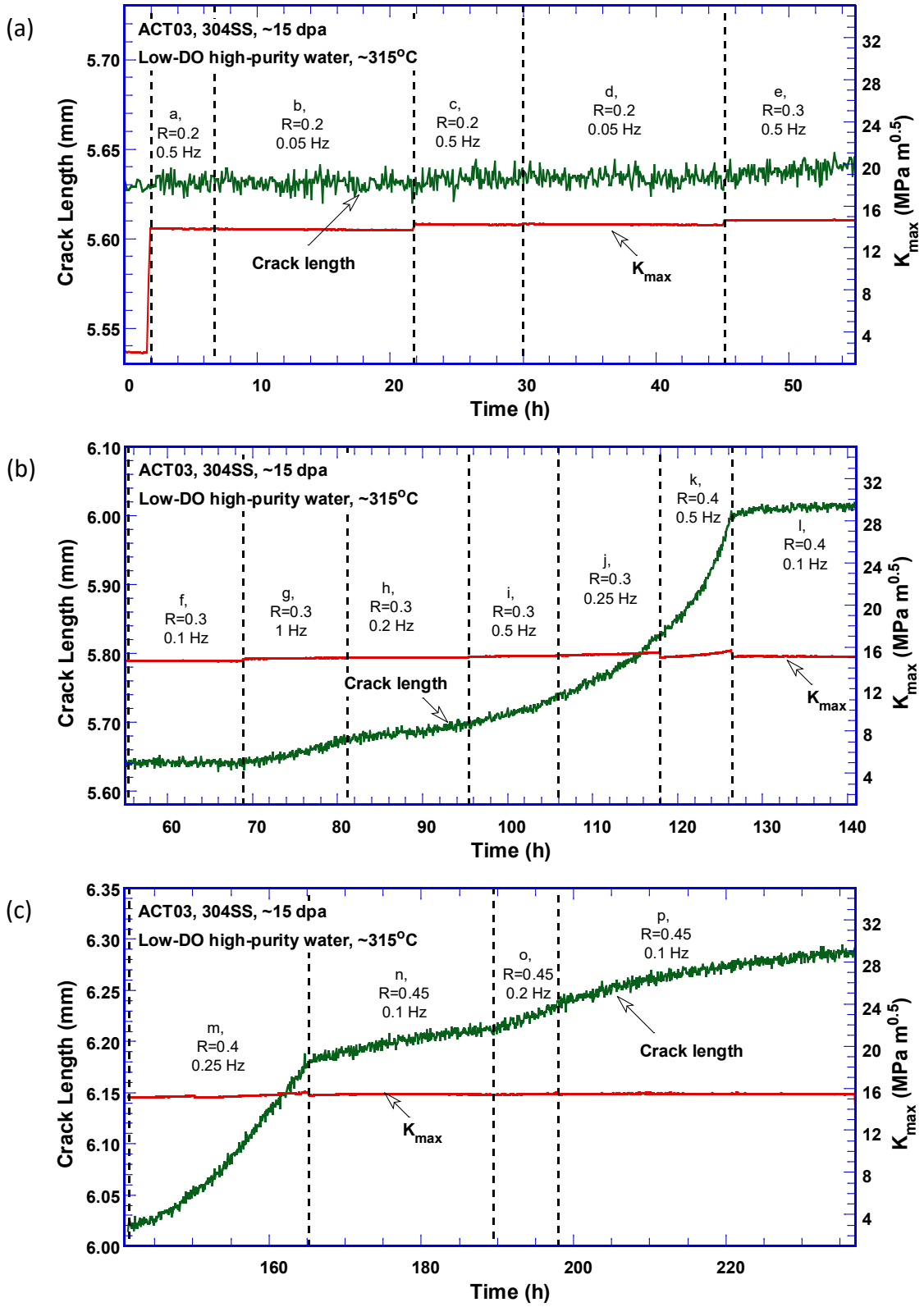

Figure 21. Crack-length-vs.-time plot of Specimen ACT03 (~15 dpa) tested in low-DO, high-purity water: test periods (a) a–e, (b) f–l, (c) m–p, (d) q–u, (e) v–y, (f) 1–2, (g) z–ac, (h) 3–4, (i) ad–ag, and (j) 5–6

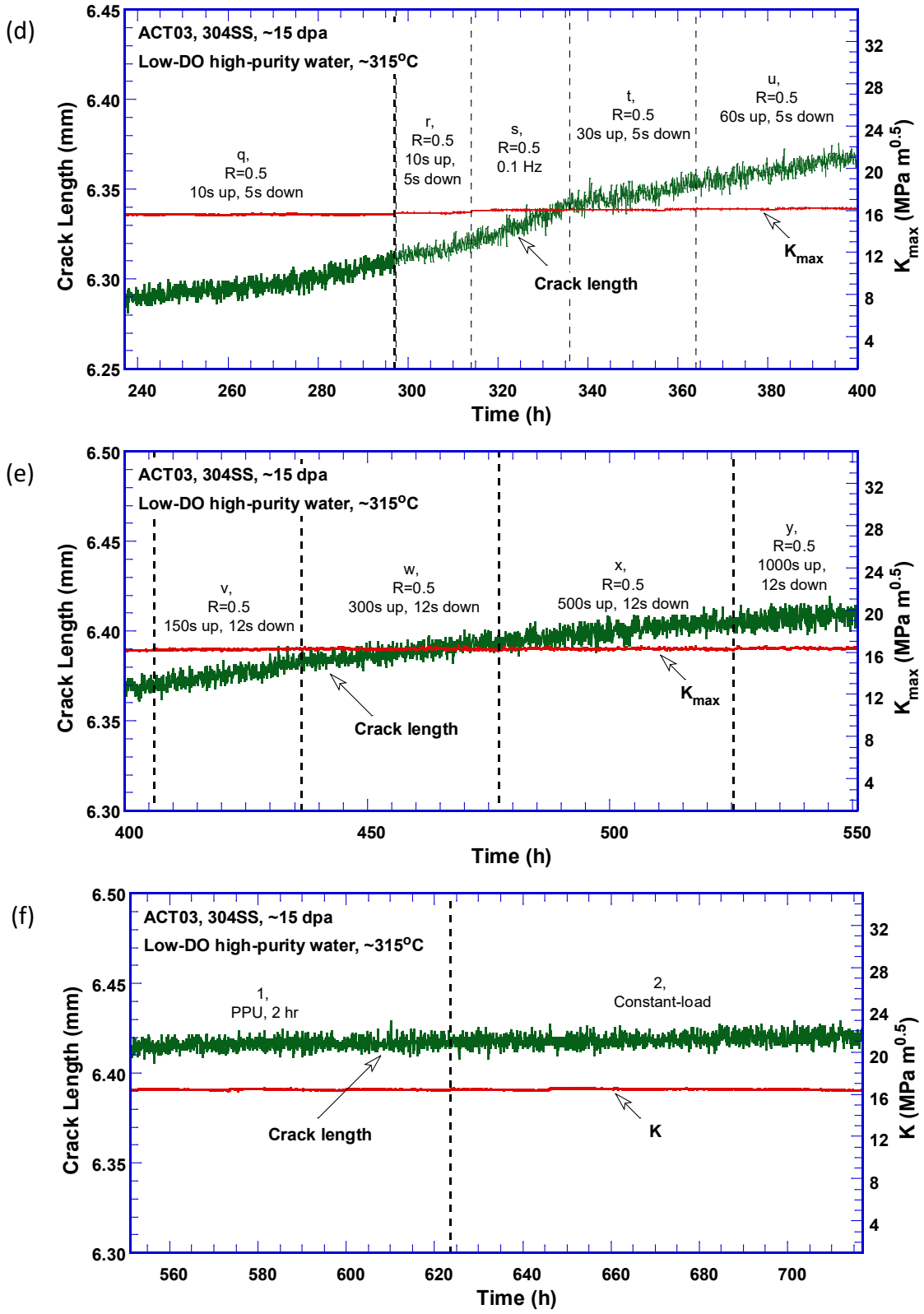

Figure 21. (Cont.)

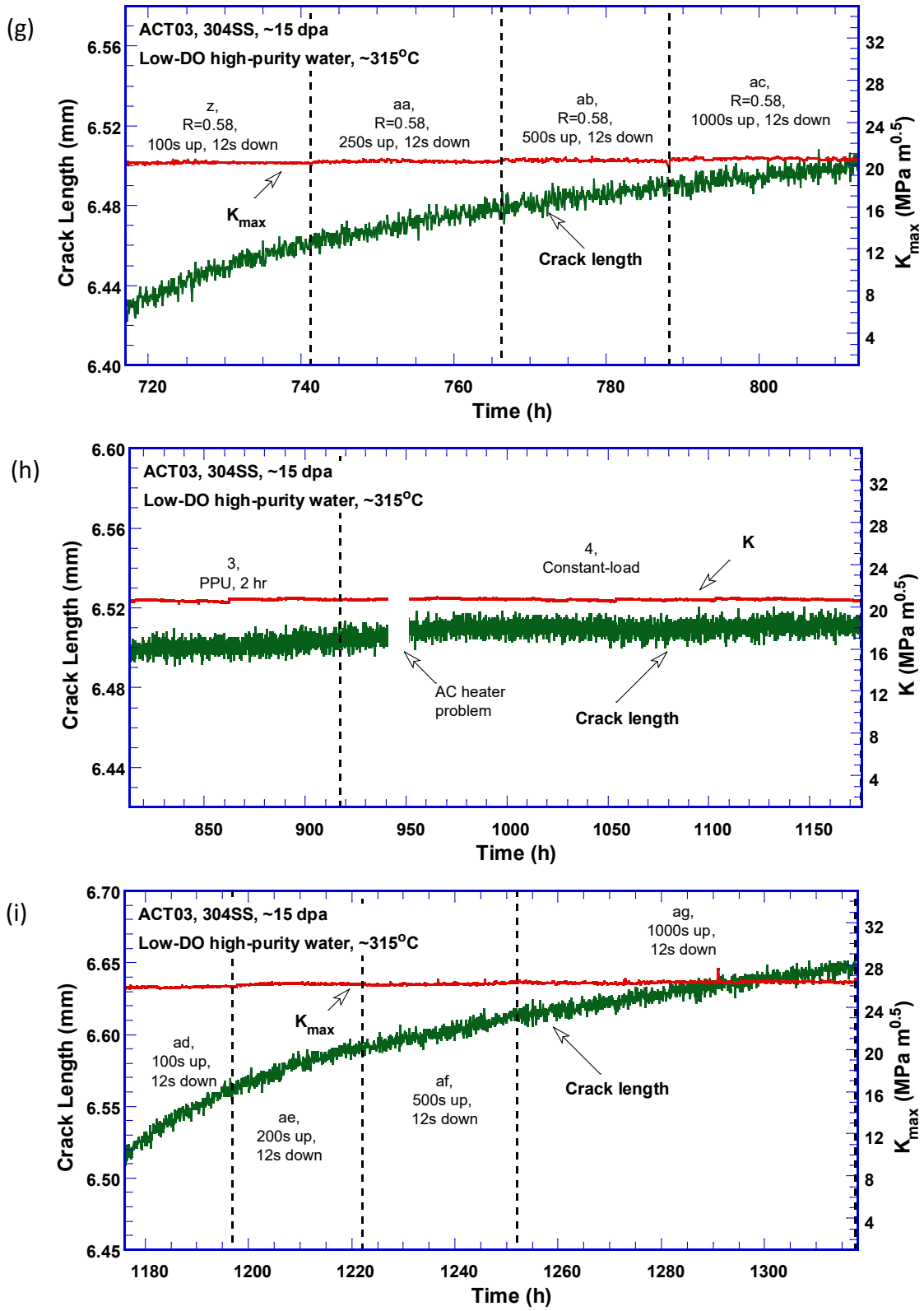

Figure 21. (Cont.)

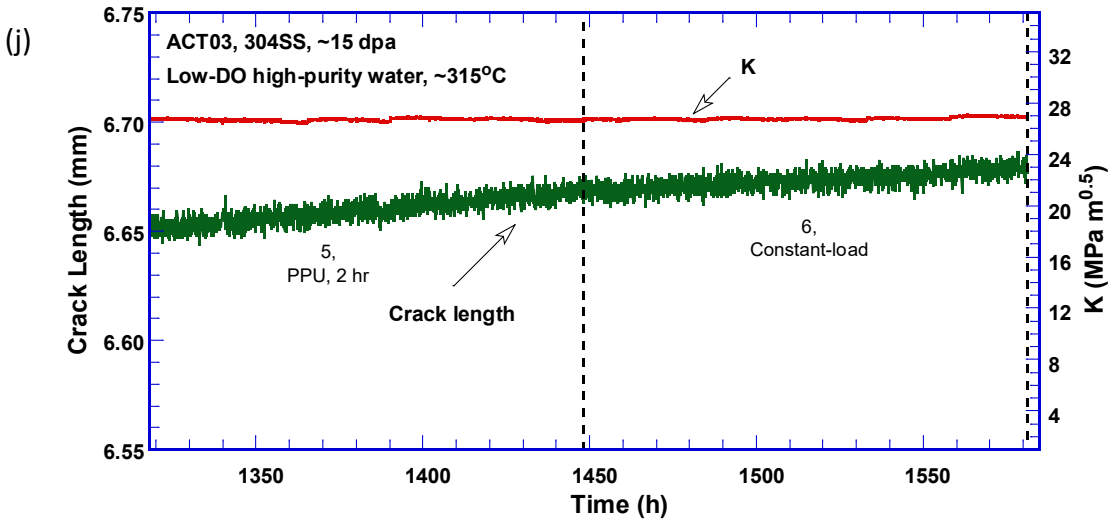

Figure 21. (Cont.)

Figure 22 shows the cyclic CGRs in water as a function of the expected fatigue growth rates in air under the same loading conditions. The crack was more difficult to initiate and stalled often in this sample, as shown by the data below the diagonal line. Repeated attempts had to be made to induce environmentally enhanced cracking in this sample. However, once initiated, the enhancement was stable, and became stronger over time as exhibited by the cyclic test periods to advance the crack from a low K level to a higher one.

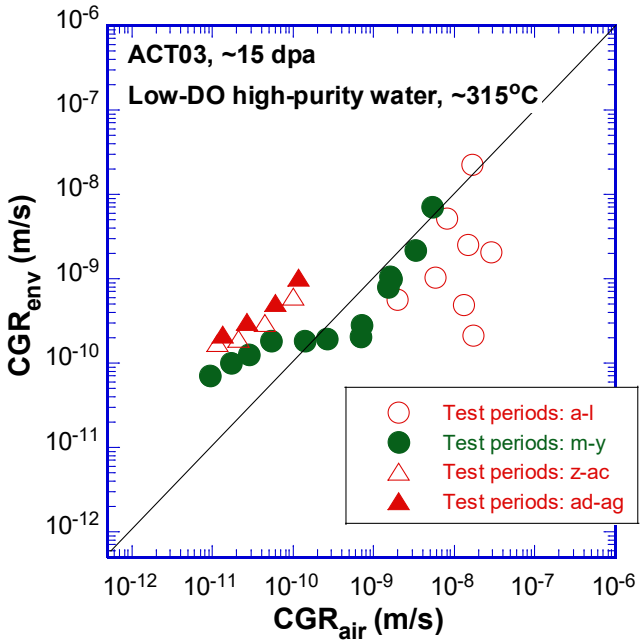

Figure 22. Cyclic CGRs of Specimen ACT03 (~15 dpa) tested in low-DO, high-purity water

Figure 23 shows the SCC CGRs as a function of applied K along with the NUREG-0313 disposition curve. Similar to the samples at lower doses, this specimens shows a low cracking susceptibility in the test environment. The CGRs measured with PPU increase with the applied K, which is different from that observed in the 0.06- and 8-dpa samples.

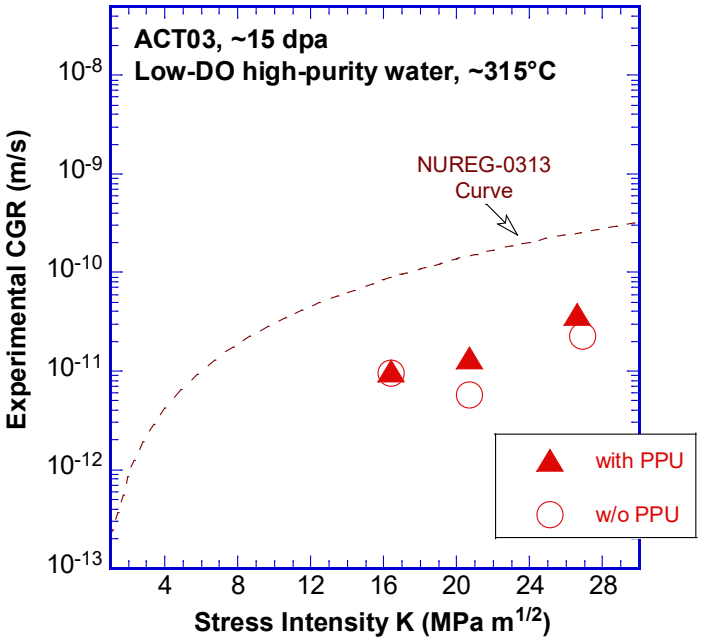

Figure 23. SCC CGRs of Specimen ACT14 (~15 dpa) tested in low-DO, high-purity water

4.3.2 Fracture Toughness J-R Curve

After the CGR test, a J-R curve test was performed on the same sample. With the SCC crack as a starter crack, the sample has an a/W of 0.56. Figure 24 shows the obtained J-Δa data along with the Δa_{max} for this sample. Thanks to the irradiation hardening, the maximum J value can be determined with this sample is much higher than the J-Δa data obtained in this test. The J-Δa data was fitted to a power-law relationship of $J = 92 \times \Delta a^{0.13}$. The J value at the 0.2-mm off-set line was about 77 kJ/m^2. Note that the data points outside the exclusion lines had to be used for the curve fitting because the crack advanced rapidly during the test after initiation. As a result, the J_Q value cannot be validated for J_{1C} per the ASTM standard. Nonetheless, this J_Q value is lower than those of the 0.06- and 8-dpa samples, implying an increasing degree of embrittlement at this dose level.

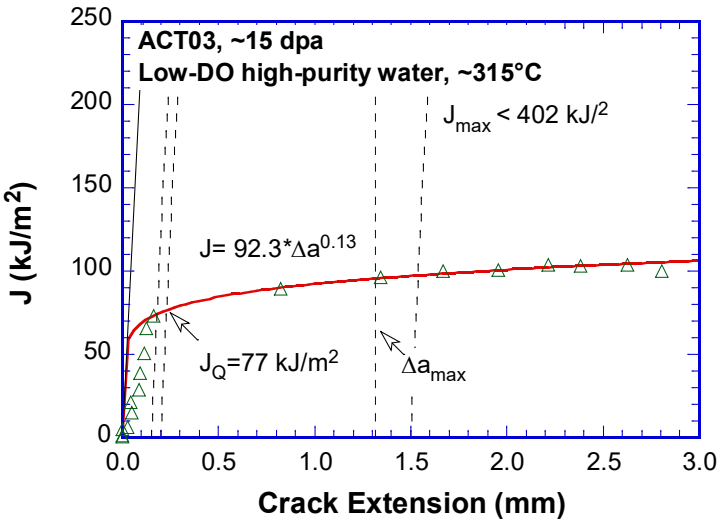

Figure 24. J-R curve of Specimen ACT03 (~15 dpa) tested at ~315°C

4.3.3 Fracture Morphology

After the J-R curve test, the sample was cyclically loaded in air at room temperature to break the remaining ligament. After decontamination, the fracture surface was examined with replicas under a SEM. Figure 25 shows the entire fracture surface of Specimen ACT03. The CGR crack front is quite straight, suggesting well-controlled loading during the test. The CGR test region showed a TG morphology at the beginning but transitioned to an IG morphology gradually as the crack advanced. Figure 26 shows an enlarged view of the region along the sample's centerline. The crack propagation direction is from bottom to top in the picture. The contrast between the CGR and J-R test regions is evident. Details of the beginning and later stages of CGR test appear in Figure 27 and Figure 28, respectively.

The J-R test region is a mixed mode fracture, as shown in Figure 29. Elongated brittle areas parallel to the cracking direction can be seen on the fracture surface. These narrow brittle regions may be related stringers or inclusions in the materials. A large amount of fracture surface shows ductile dimples, suggesting some remaining ductility at ~15 dpa. Similar to that observed in the 8-dpa sample, IG morphology was also observed in the post-JR region fractured in air at room temperature (see Figure 30). This unexpected IG morphology was more evident in this sample than that in the ~8-dpa specimen, suggesting a cracking behavior sensitive to neutron dose.

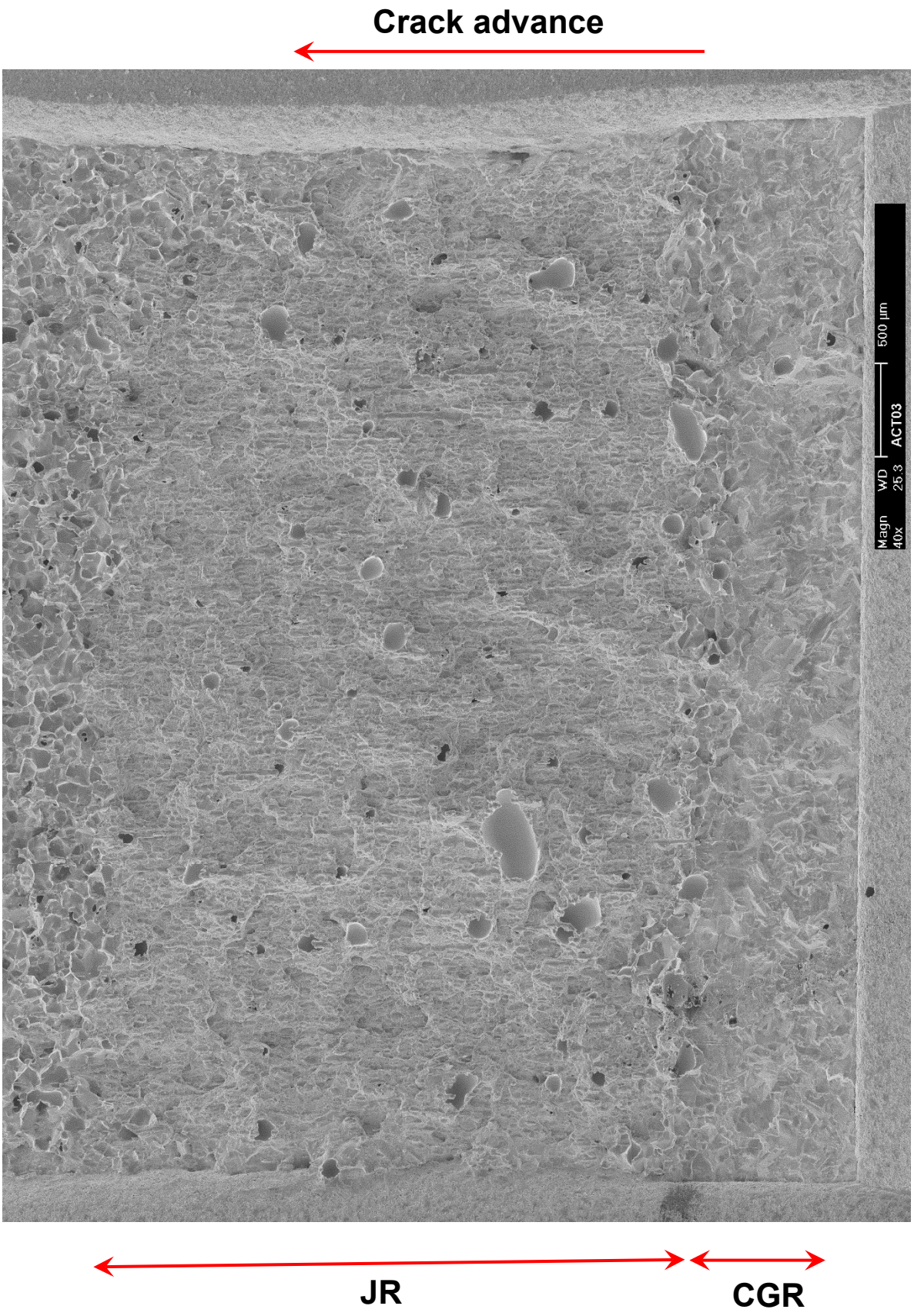

Figure 25. Fracture surface of Specimen ACT03, ~15 dpa

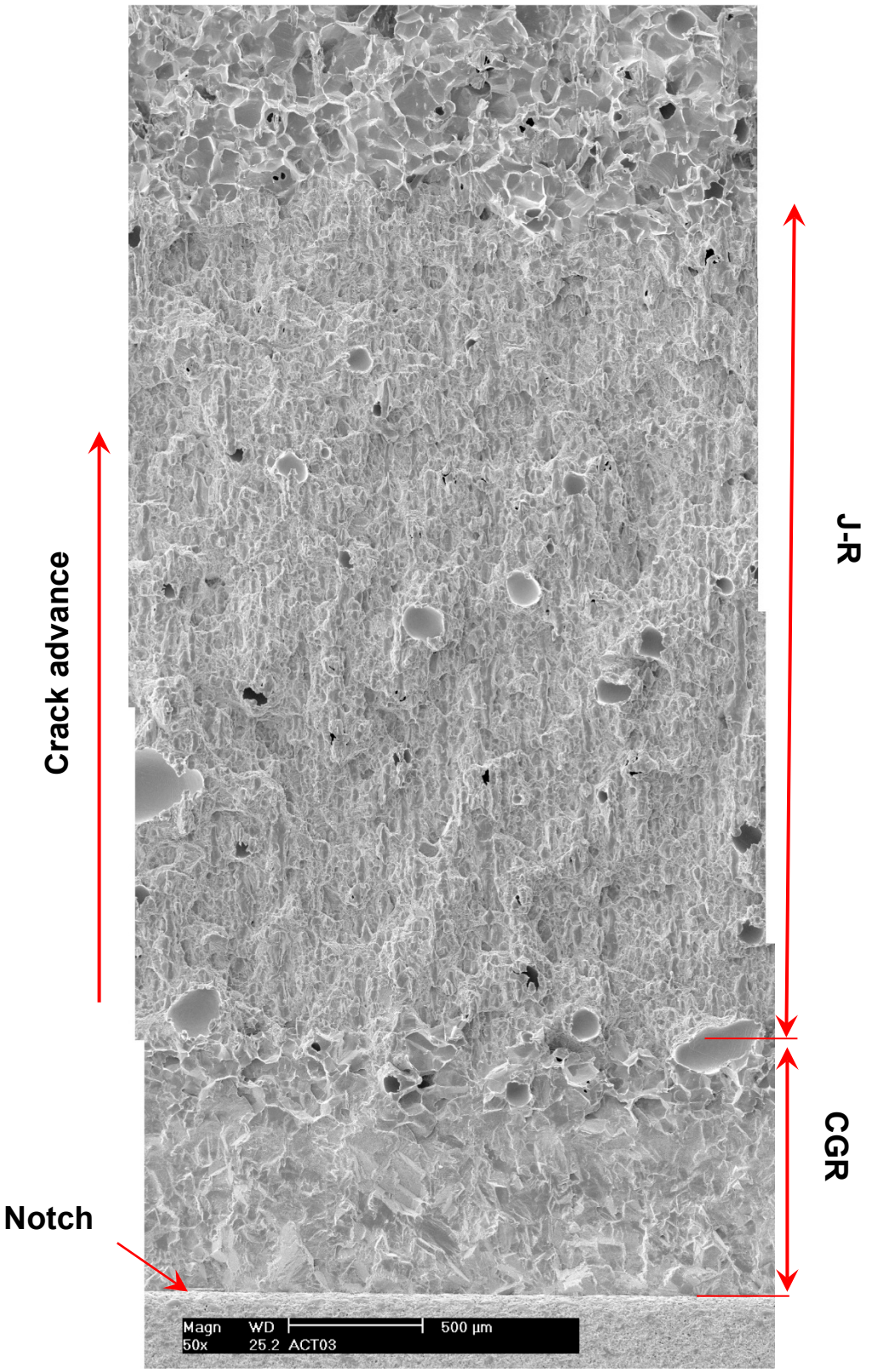

Figure 26. Enlarged view along the centerline of Specimen ACT03, ~15 dpa

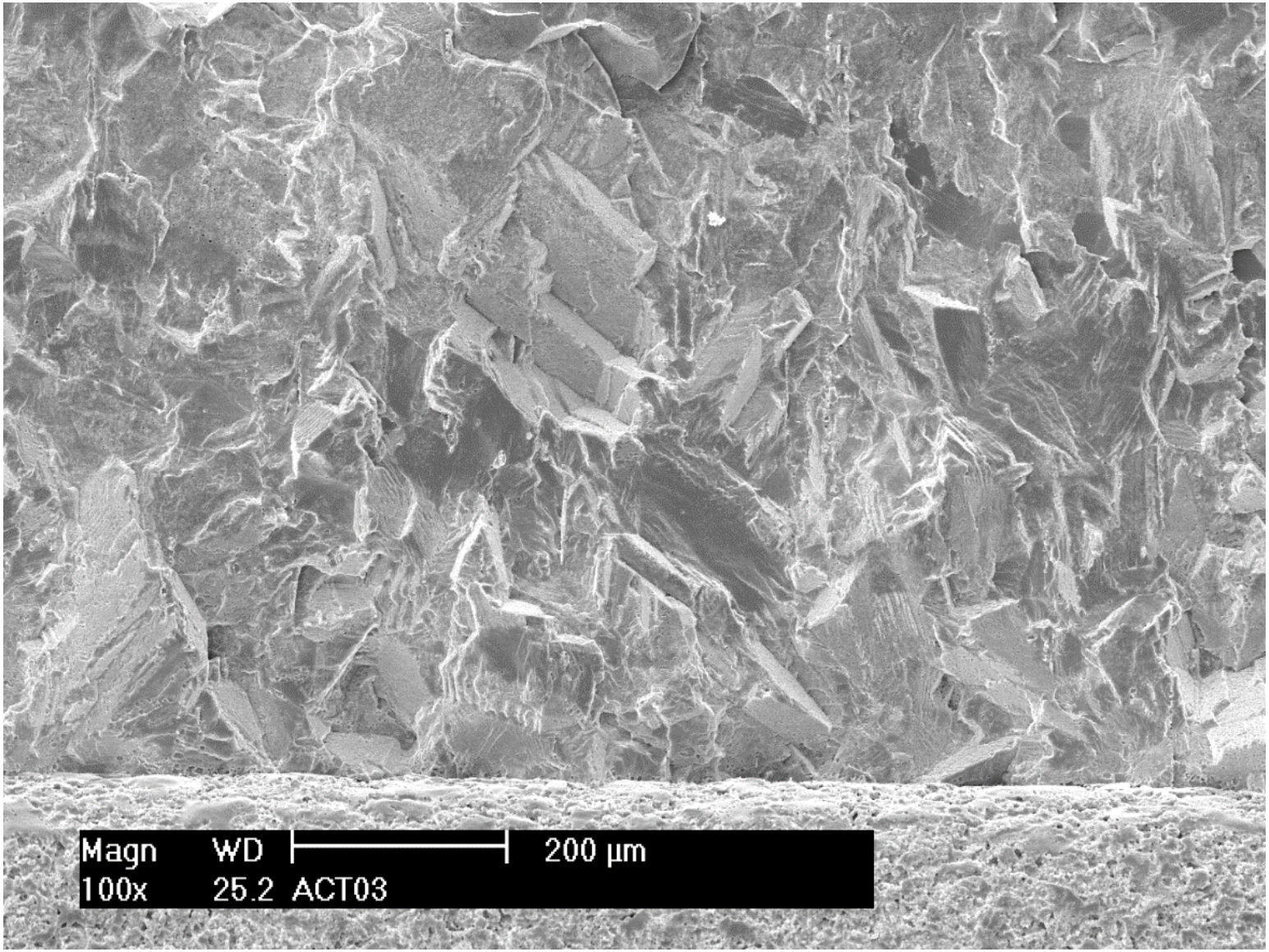

Figure 27. TG morphology at the beginning of the CGR test of Specimen ACT03

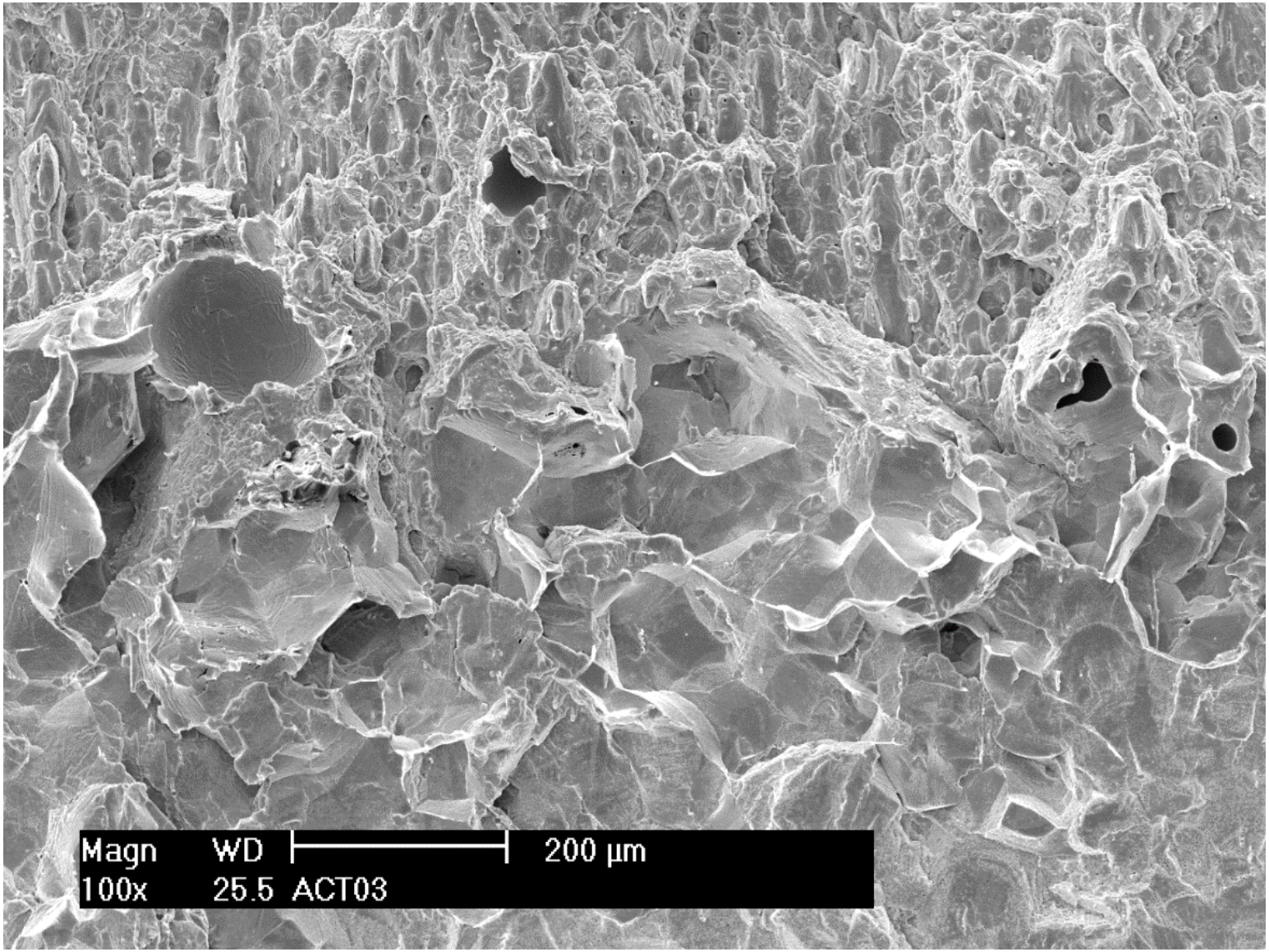

Figure 28. Transition region from the CGR to J-R curve test in Specimen ACT03

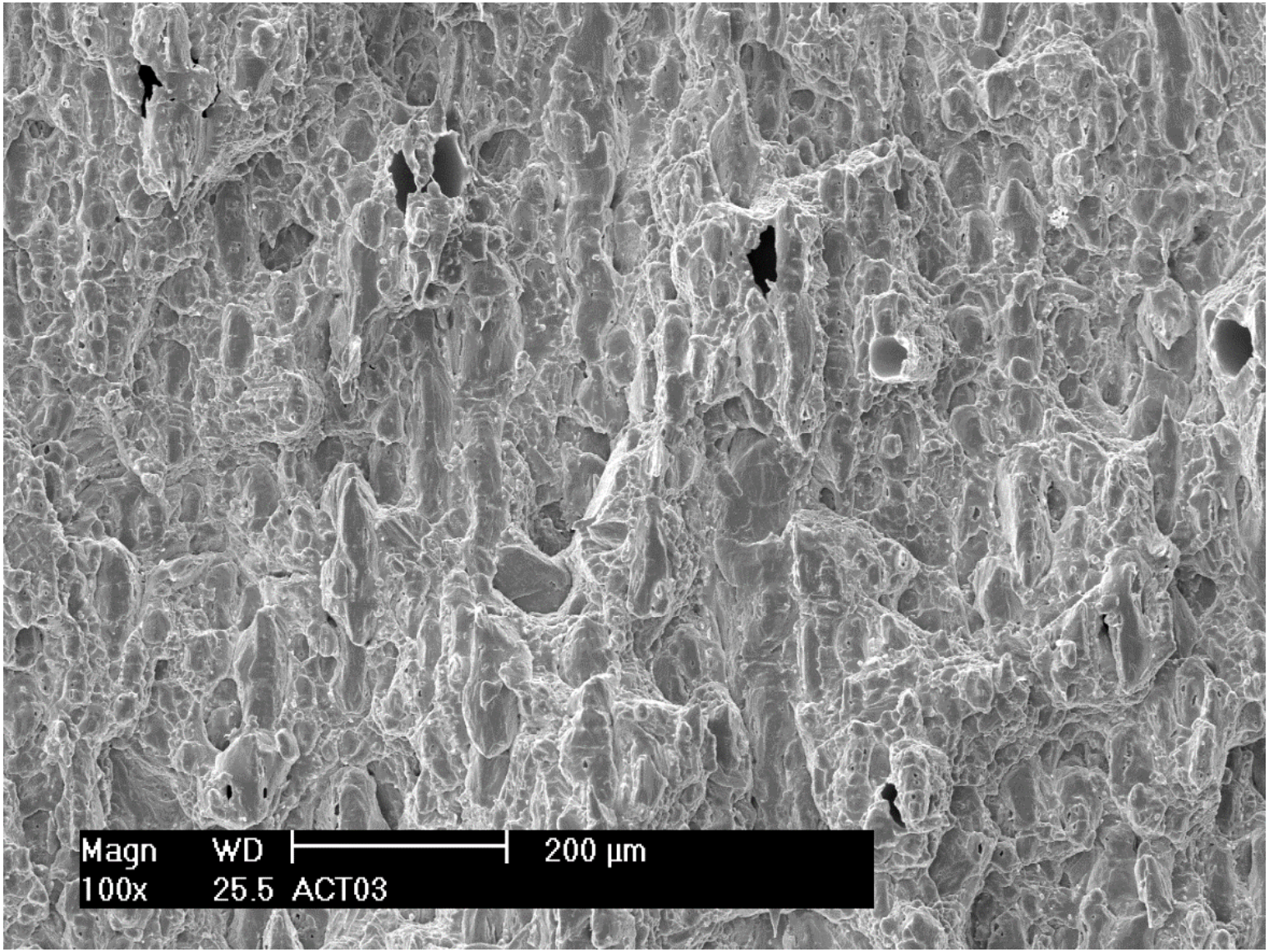

Figure 29. Mixed mode fracture during the J-R curve test in Specimen ACT03

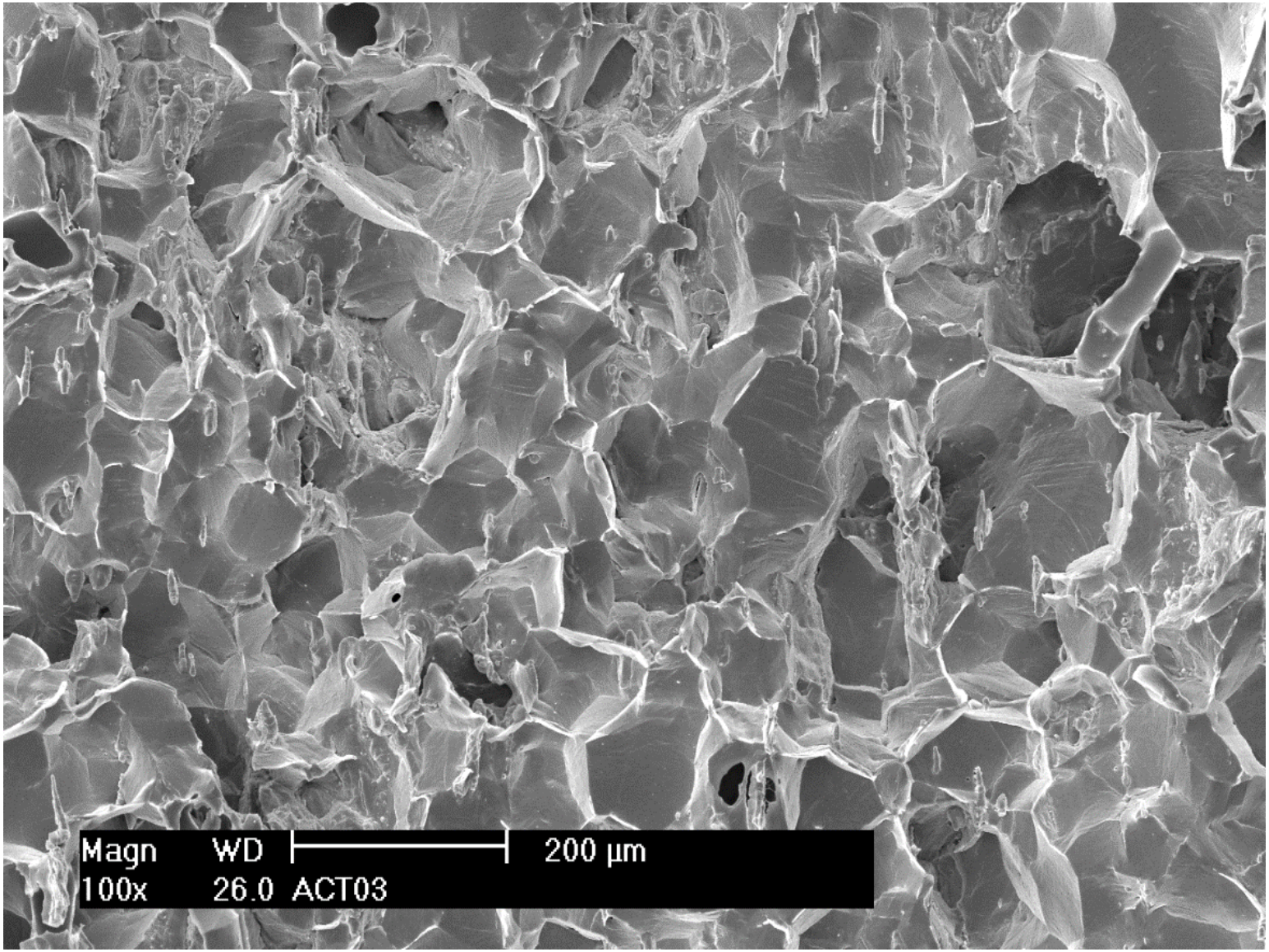

Figure 30. IG morphology resulting from the post-test cyclic loading at room temperature in Specimen ACT03

4.4 Specimen B1CT07, ~39 dpa

Specimen B1CT07 was cut from the source material "B1," which was a plate located at a convex corner of reactor core baffle. Because there were fuel assemblies next to two normal edges of this plate, the neutron fluence accumulated in this source material was fairly high. The sample was machined from the area close to the plate's outer surface (away from the reactor core), and its estimated damage dose was ~39 dpa.

4.4.1 Crack Growth Rates

The sample was tested in a low-DO, high-purity water at ~315°C. After the sample was installed in the autoclave, the system was pressurized and heated slowly to the test temperature. A constant load of about 25 lb. was maintained on the sample during pressurizing and heating. The sample was soaked in the test environment for 6 days prior to the test.

All CGR results obtained from this sample are summarized in Table 6. Figure 31 shows time history plots of crack length and applied K in this test. The cyclic loading started with a K_{max} of ~13 MPa $m^{1/2}$ at a load ratio of ~0.35 and 1 Hz. The applied K_{max} was too low and no crack extension was observed until K_{max} was increased to ~15.5 MPa $m^{1/2}$. After ~150 μm crack extension, the load ratio and rise time were gradually increased. The measured CGR declined as expected, but eventually stalled when the load ratio was too high (~0.55). The crack had to be re-initiated at a higher K_{max}. Finally, steady crack growth behavior was observed in this sample with a K_{max} of ~16 MPa $m^{1/2}$. Following that, environmentally enhanced cracking also become evident with further increases in rise time. The measured cyclic CGR was about 1 order of magnitude higher than the expected fatigue growth rate in air by the end of cyclic loading test. The test was then set to a constant K (~16.8 MPa $m^{1/2}$) with PPU every 2 hours. A SCC CGR of 3.0×10^{-11} m/s was obtained over ~12 μm crack extension. A steam leak occurred inside the hot cell which interrupted the test for ~150 hours (see Figure 31g). After the system was recovered, a short cyclic test was performed to confirm that the SCC crack was still active. Indeed, the environmental enhancement remained strong and the measured CGR was more than 1 order of magnitude higher than that of fatigue growth rate in air. The SCC test then resumed at ~17 MPa $m^{1/2}$ with a constant K without PPU. A SCC CGR of 1.8×10^{-11} m/s was measured over ~5 μm crack extension.

Next, the crack was advanced with cyclic loading at a K_{max} of ~21 MPa $m^{1/2}$. A load ratio of ~0.56 was used to maintain a similar ΔK as that used at the lower K level. No jump in crack length was observed when the applied K was increased (Figure 31h). As the rise time increased gradually, the environmental enhancement remained stable as shown in Figure 32. After ~125 μm crack extension, the test was set to a constant K with PPU every 2 hours. A SCC CGR of 3.0×10^{-11} m/s was obtained over ~19 μm crack extension. After the PPU was removed, the CGR was lowered to 1.8×10^{-11} m/s.

The crack was advanced once again under cyclic loading with a K_{max} of ~26 MPa $m^{1/2}$. No jump was observed when the K was increased. With the increasing rise time, the environmental enhancement factor was similar to that at lower K_{max}. After ~150 μm crack extension, the test was set again to a constant K with PPU every 2 hours. A SCC CGR of 3.9×10^{-11} m/s was measured over ~20 μm crack extension. After the PPU was removed, a lower CGR of 1.5×10^{-11} m/s was obtained. At the end of this SCC test period, a few loading cycles (20-30 cycles) were applied on the sample with a K_{max} of ~26 MPa $m^{1/2}$. Again, no jump in crack length was observed within the resolution of the DCPD measurement.

Table 6. Crack growth rates of Specimen B1CT07 (~39 dpa) in low-DO, high-purity water

Test Period [1]	Test Time (hr)	Test Temp. (°C)	Load Ratio	Rise Time (s)	Return Time (s)	Hold Time (s)	K_{max} (MPa $m^{1/2}$)	ΔK (MPa $m^{1/2}$)	CGR in Env. (m/s)	CGR in Air (m/s)	Crack Length (mm)
Start	0.3										5.700
a	3.6	314	0.36	0.4	0.4	0.1	13.1	8.4	negligible	1.74E-08	5.711
b	8.7	314	0.36	0.4	0.4	0.1	14.1	9.0	3.45E-10	2.19E-08	5.708
c	26.7	314	0.33	0.4	0.4	0.1	14.5	9.7	negligible	2.62E-08	5.713
d	35.9	314	0.33	0.4	0.4	0.1	15.0	10.1	1.06E-09	2.97E-08	5.730
e [2]	54.4	315	0.34	0.4	0.4	0.1	15.5	10.2	2.28E-08	3.18E-08	5.855
f [2]	69.5	315	0.43	0.8	0.8	0.2	15.9	9.0	1.63E-08	1.21E-08	6.051
g	80.0	314	0.54	1.4	1.4	0.6	15.5	7.1	1.59E-09	3.17E-09	6.075
h	94.9	314	0.59	3.5	3.5	1.5	15.4	6.4	1.21E-10	9.64E-10	6.084
i [2]	104.0	314	0.44	1.9	1.9	0.6	15.7	8.9	4.78E-09	4.59E-09	6.122
j	128.4	314	0.49	3.7	3.7	1.3	15.6	8.0	8.26E-10	1.78E-09	6.151
k	166.4	316	0.53	10.8	3.6	4.2	15.5	7.3	1.31E-10	4.74E-10	6.160
l	174.4	316	0.49	1.5	1.5	0.5	15.6	8.0	1.12E-09	4.40E-09	6.168
m	192.1	316	0.50	7.4	3.7	2.6	15.9	8.0	5.21E-10	9.01E-10	6.189
n	221.0	317	0.53	21.6	3.6	8.4	15.7	7.5	1.04E-10	2.49E-10	6.198
o	238.6	317	0.45	3.8	3.8	1.2	16.2	8.9	2.08E-09	2.37E-09	6.244
p	262.9	313	0.50	7.3	3.7	2.7	16.1	8.1	4.06E-10	9.42E-10	6.266
q	287.4	313	0.49	22.2	3.7	7.8	16.4	8.3	2.86E-10	3.38E-10	6.284
r	311.7	314	0.49	44.4	8.9	15.6	16.5	8.5	3.72E-10	1.76E-10	6.303
s	335.4	314	0.49	110.8	8.9	39.2	16.5	8.5	2.75E-10	7.03E-11	6.319
t	360.1	314	0.49	184.1	8.8	65.9	16.4	8.4	2.35E-10	4.14E-11	6.335
u	383.8	316	0.48	371.7	8.9	128.3	16.7	8.7	1.59E-10	2.30E-11	6.343
v	410.4	312	0.48	745.0	8.9	255.0	16.8	8.8	1.17E-10	1.18E-11	6.350
1	513.4	309	0.50	12	12	7200	16.8	8.4	3.03E-11	1.06E-12	6.362
w	679.8	313	0.46	756.2	9.1	243.8	16.7	9.0	2.32E-10	1.23E-11	6.379
2	791.0	313	1	-	-	-	17.1	-	1.84E-11	-	6.384
x	799.5	314	0.57	75.1	9.0	24.9	20.9	8.9	2.54E-09	1.33E-10	6.439
y	814.6	312	0.57	188.1	9.0	61.9	21.0	9.0	6.05E-10	5.53E-11	6.465
z	838.5	312	0.56	377.7	9.1	122.3	21.0	9.2	4.14E-10	2.94E-11	6.489
aa	863.5	311	0.56	757.4	9.1	242.6	21.4	9.4	2.40E-10	1.54E-11	6.508
3	959.6	312	0.60	12	12	7200	21.3	8.5	3.01E-11	1.22E-12	6.527
4	1,059.3	312	1	-	-	-	21.1	-	1.82E-11	-	6.531
ab	1,079.5	312	0.67	72.4	8.7	27.6	25.5	8.5	1.34E-09	1.27E-10	6.605
ac	1,102.4	312	0.67	181.0	8.7	69.0	25.6	8.6	5.24E-10	5.25E-11	6.637
ad	1,126.7	312	0.67	362.0	8.7	138.0	26.0	8.6	3.53E-10	2.69E-11	6.660
ae	1,158.4	310	0.66	727.5	8.7	272.5	26.2	8.8	2.85E-10	1.44E-11	6.681
5	1,246.5	312	0.68	12	12	7200	26.0	8.3	3.94E-11	1.21E-12	6.701
6	1,347.7	311	1	-	-	-	26.2	-	1.47E-11	-	6.705
Complete											

[1] Cyclic test periods are named in alphabetical order, and constant-K test periods are named in numerical order.
[2] Crack growth rate in the later part of the test period is reported.

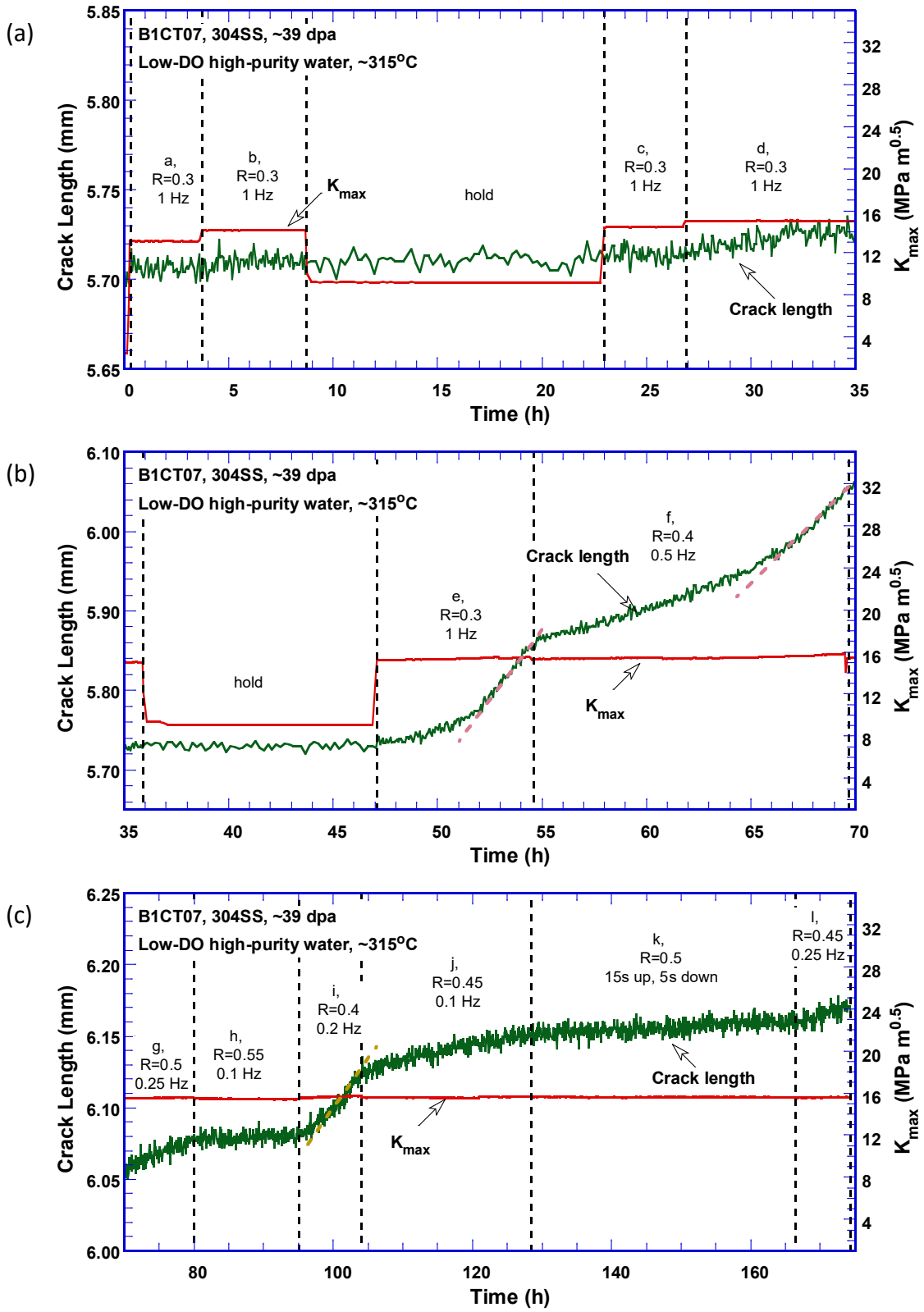

Figure 31. Crack-length-vs.-time plot of Specimen B1CT07 (~39 dpa) tested in low-DO high-purity water: test periods (a) a–d, (b) e–f, (c) g–l, (d) m–p, (e) q–s, (f) t–v, (g) 1–2, (h) x–aa, (i) 3–4, (j) ab–ae, and (k) 5–6

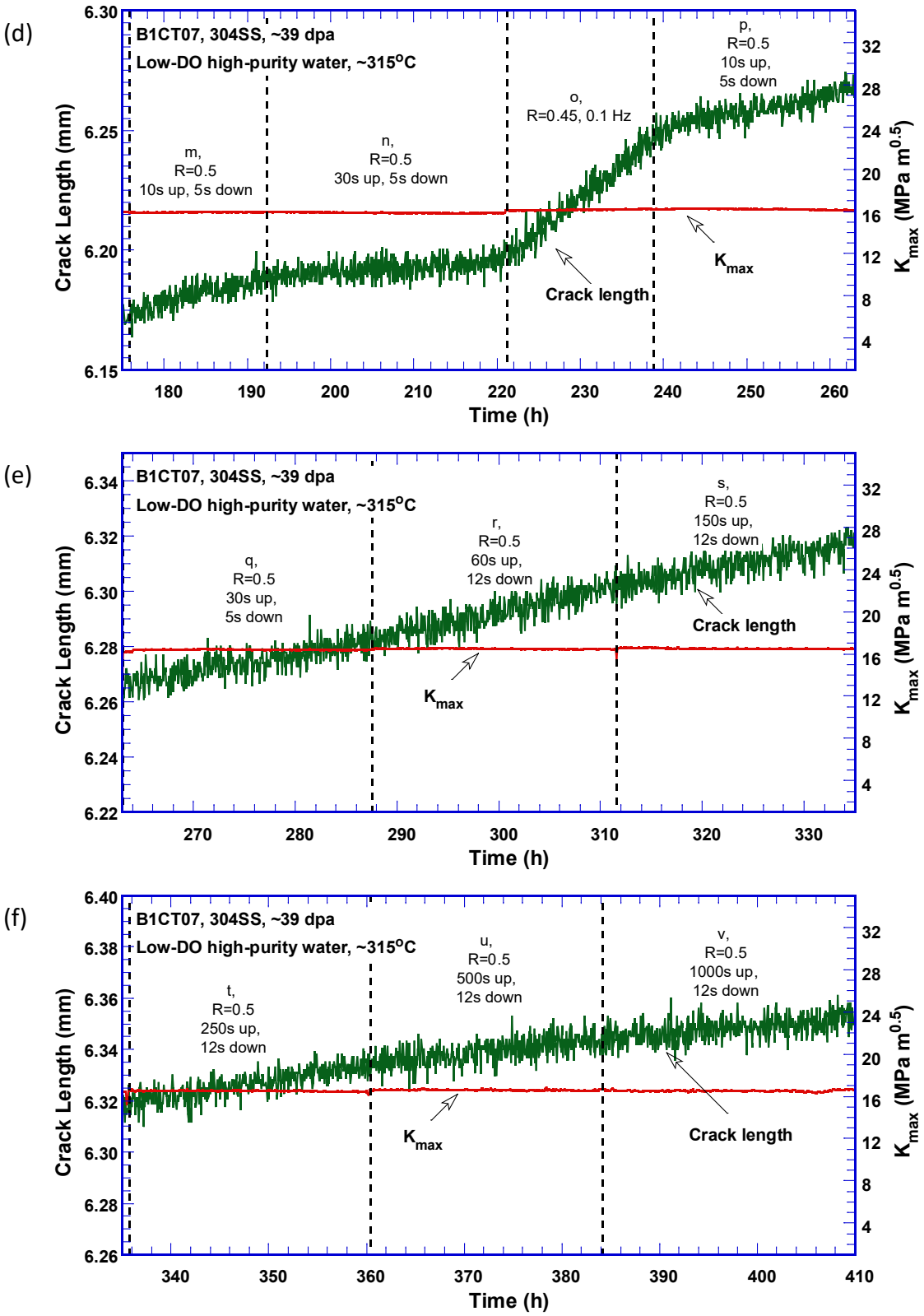

Figure 31. (Cont.)

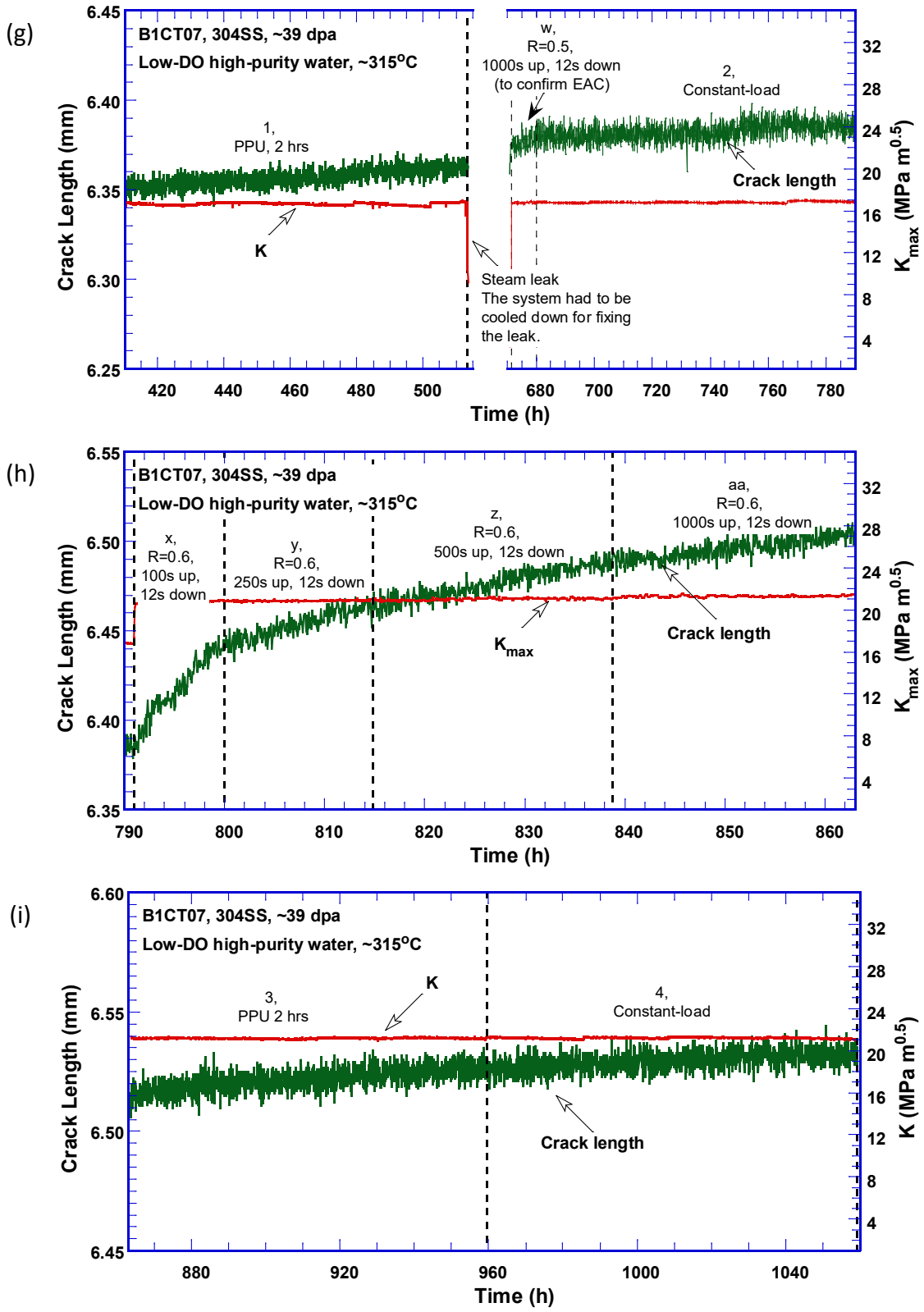

Figure 31. (Cont.)

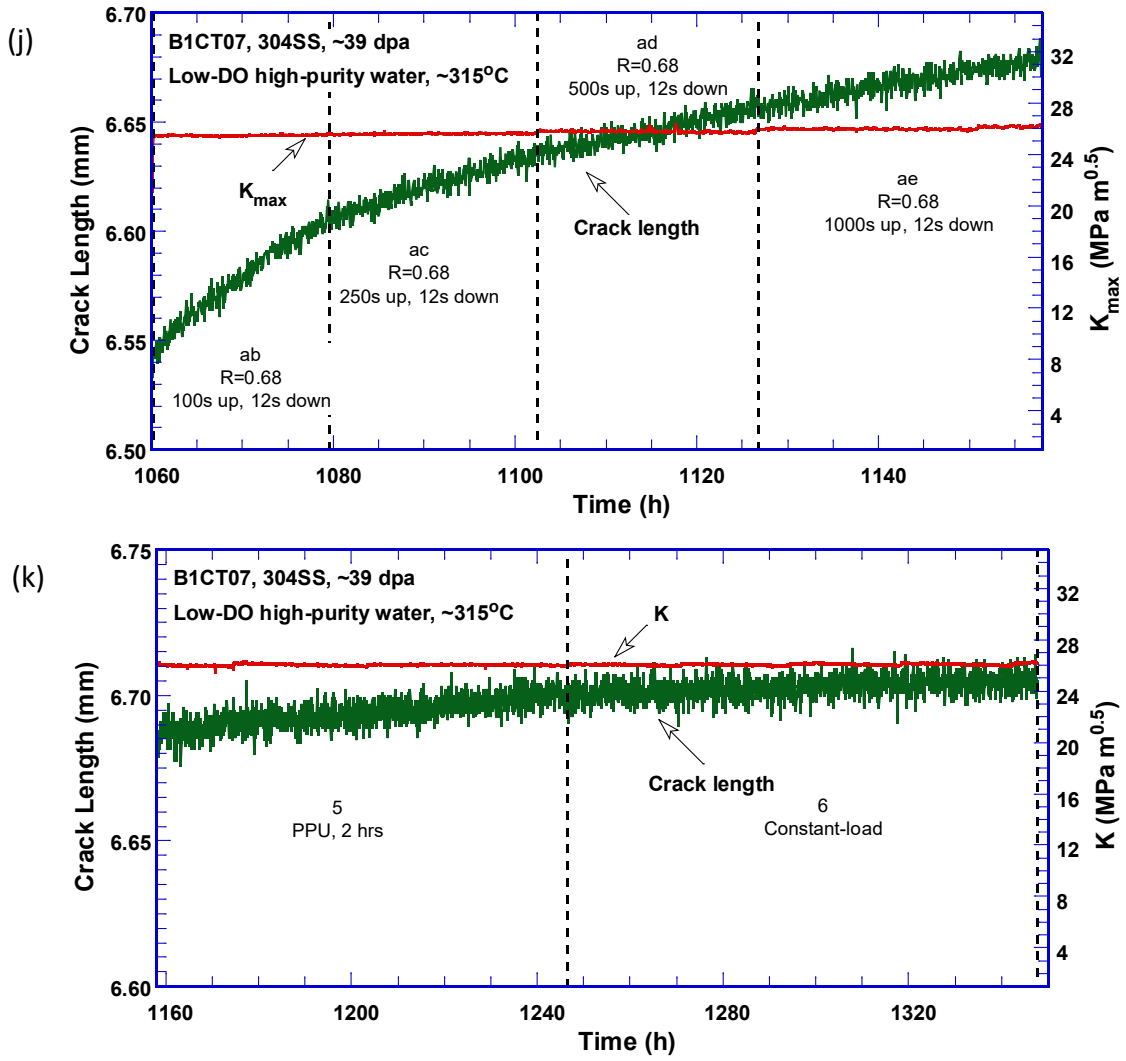

Figure 31. (Cont.)

Figure 32 shows the cyclic CGRs obtained from this sample as a function of fatigue growth rate in air under the same loading condition. Similar to the 15-dpa sample, quite a few data points are below the diagonal line at the upper-right part of the figure. This was caused by the difficulty in pre-cracking. However, once the cracking started, environmental enhancement was strong and remained stable over a long period. This corrosion fatigue behavior is somewhat different from that observed in the 0.06-dpa sample.

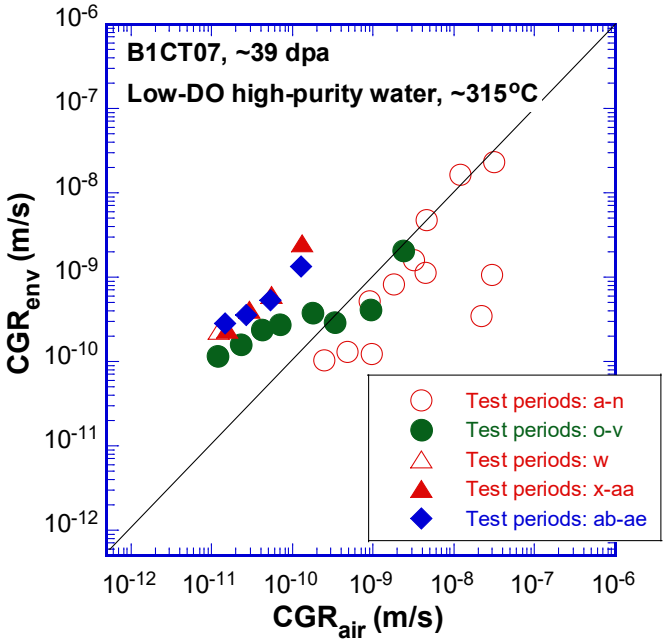

Figure 32. Cyclic CGRs of Specimen B1CT07 (~39 dpa) tested in low-DO, high-purity water

The SCC CGR results are shown in Figure 33. All CGRs with and without PPU are below the NUREG-0313 disposition curve, suggesting good SCC resistance in the test environment. The CGRs obtained with PPU are slightly higher, but no K dependence can be seen in this sample.

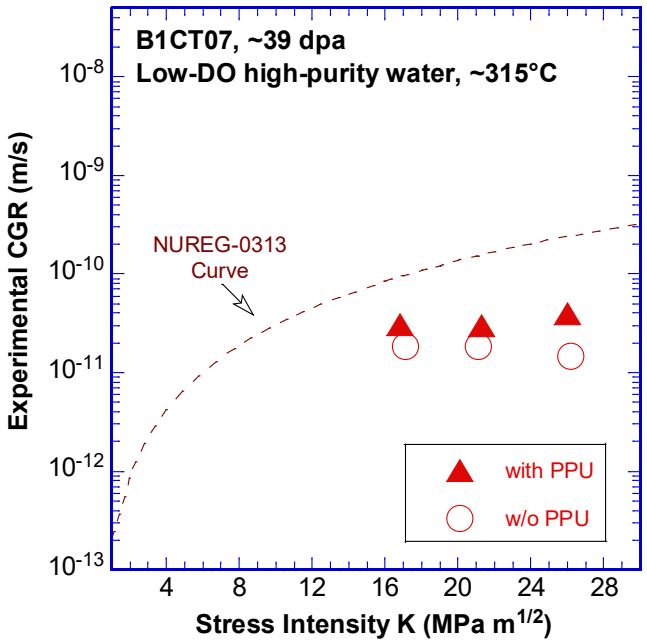

Figure 33. SCC CGRs of Specimen B1CT07 (~39 dpa) tested in low-DO, high-purity water

4.4.2 Fracture Toughness J-R Curve

After the CGR test, a fracture toughness J-R curve test was performed on the sample in the same test environment. With a SCC starter crack, the initial a/W for this sample is about 0.56. During the test, the sample was loaded with a constant displacement rate, and the crack extension was measured periodically with DCPD. The obtained J-Δa data are shown in Figure 34. The Δa_{max} and J_{max} are also given in the figure. A curve fitting of the J-Δa data gives rise to a power-law correlation of $J = 80 \times \Delta a^{0.12}$. Note that the data points outside the exclusion lines are used for the curve fitting. The power exponent of the J-R curve is quite low for this sample, similar to that obtained from the samples at ~15 dpa. The J value at the 0.2-mm offset line is about 71 kJ/m^2. Note that this J_Q value cannot be validated for J_{1C} per the ASTM standard because the straightness of the final crack front is invalid.

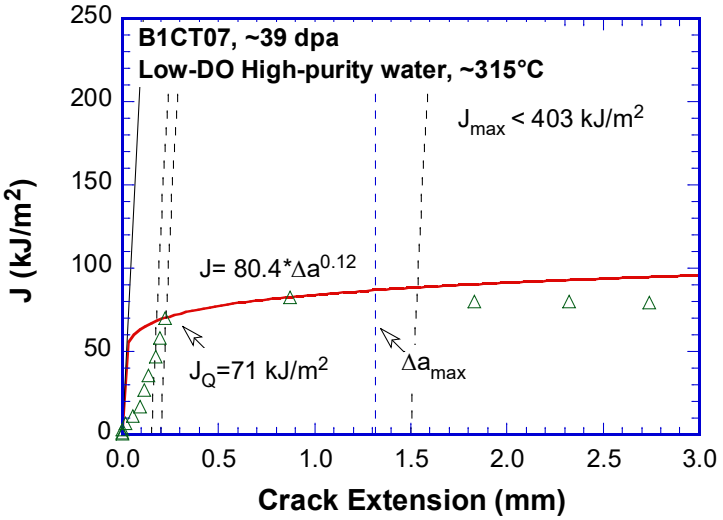

Figure 34. J-R curve of Specimen B1CT07 (~39 dpa) tested at ~315°C

4.4.3 Fracture Morphology

After the J-R curve test, the sample was broken open in air at room temperature with cyclic loading. Multiple replicas were produced from the sample fracture surface and were decontaminated for SEM examination. Figure 35 shows the entire fracture surface. The crack front of the CGR test region is relatively straight indicating well-controlled loading in the test. Figure 36 is an enlarged view along the sample centerline. The CGR region shows a mixed-mode fracture of TG and IG morphologies. As shown in Figure 37, the fracture is mostly TG at the beginning of the CGR test with some IG facets. As the crack grew deeper, IG cracking became more evident at the end of the CGR test (see Figure 38). In the J-R test region, the fracture mode is mostly ductile with some elongated brittle features as shown in Figure 39. Beyond the J-R curve test, the fracture morphology is 100% IG as shown in Figure 40. This unexpected brittle morphology generated at room temperature in air under cyclic loading was very similar to that observed in the 15-dpa sample, suggesting severe irradiation embrittlement of the sample at this dose level.

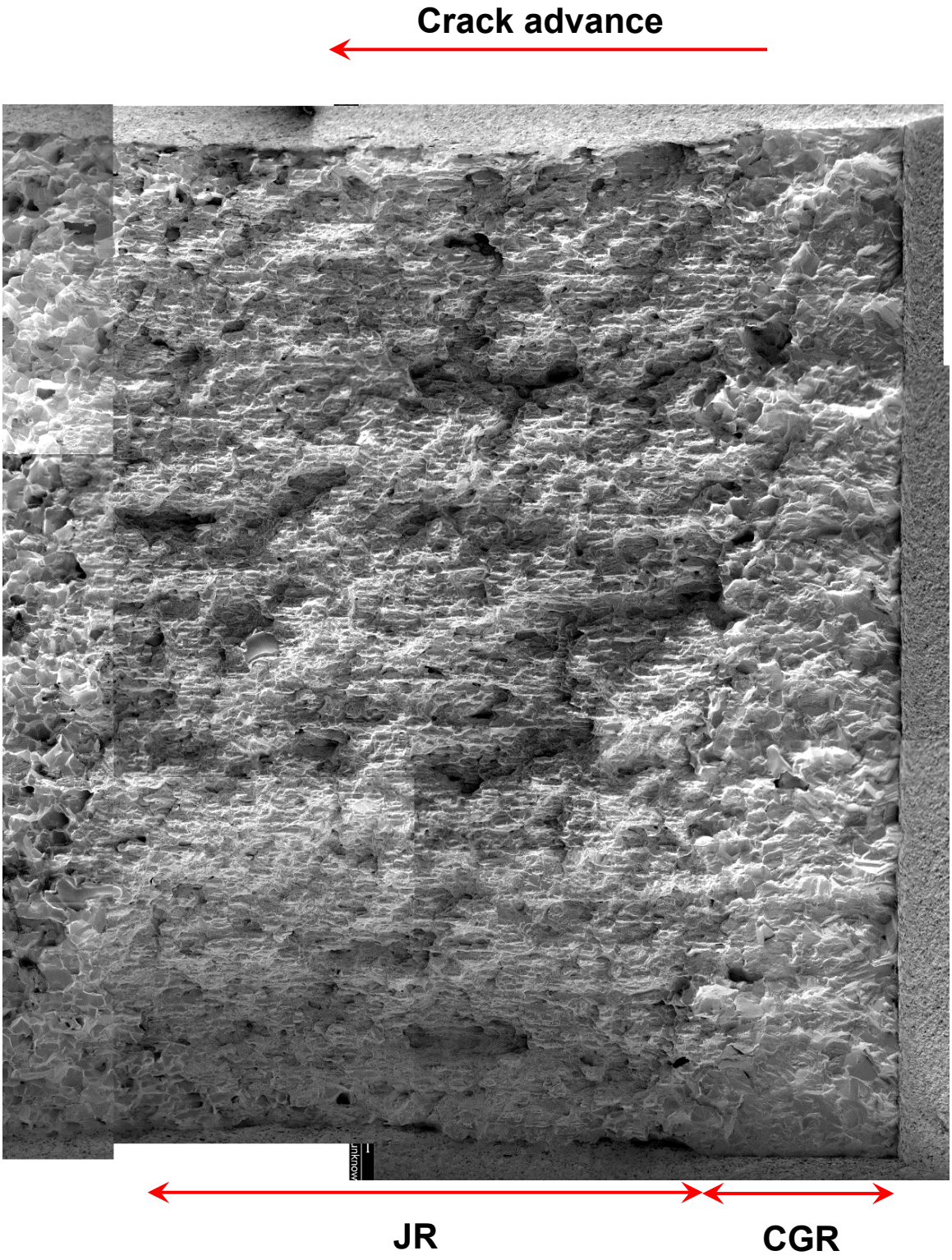

Figure 35. Fracture surface of Specimen B1CT07, ~39 dpa

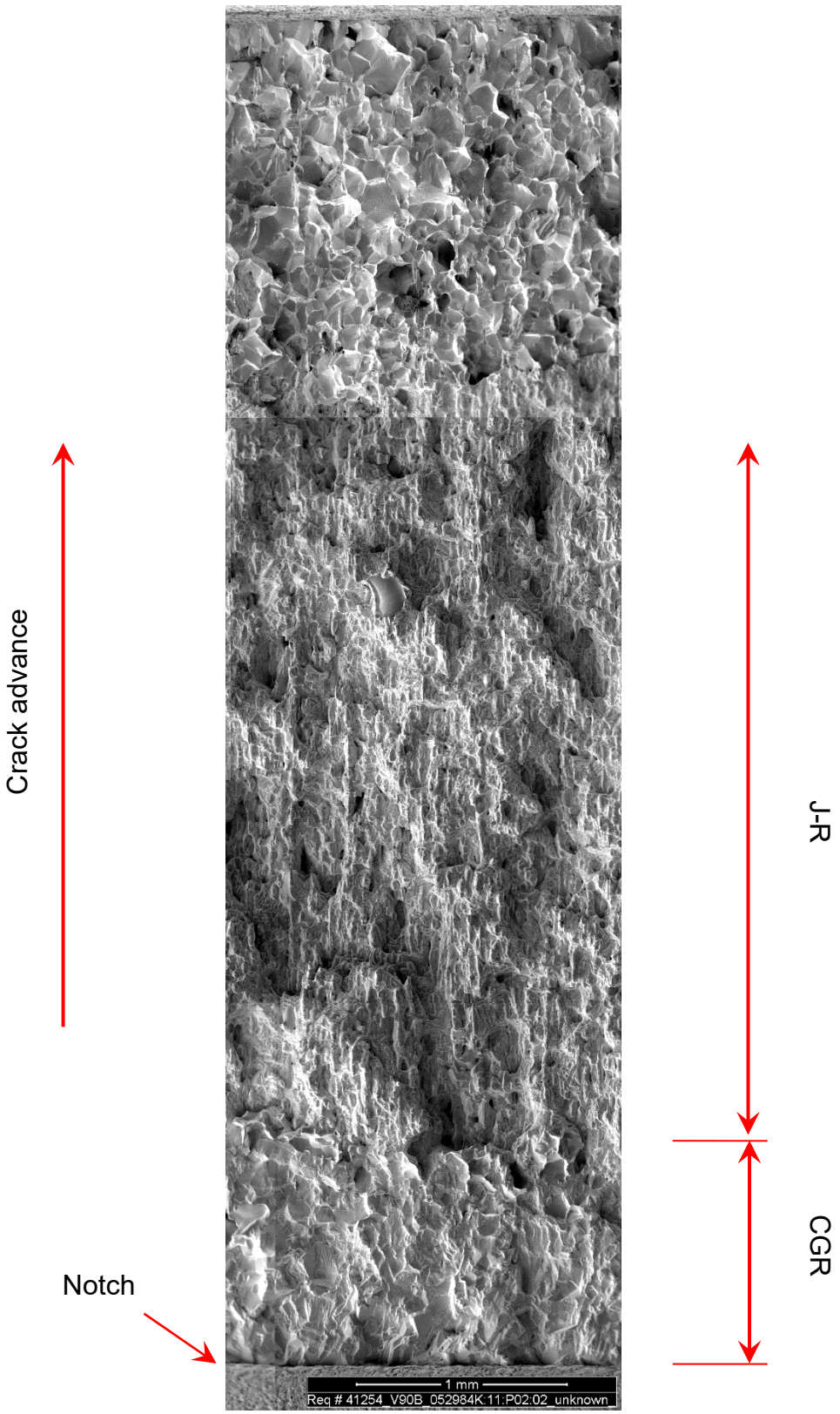

Figure 36. Enlarged view along the centerline of Specimen B1CT07

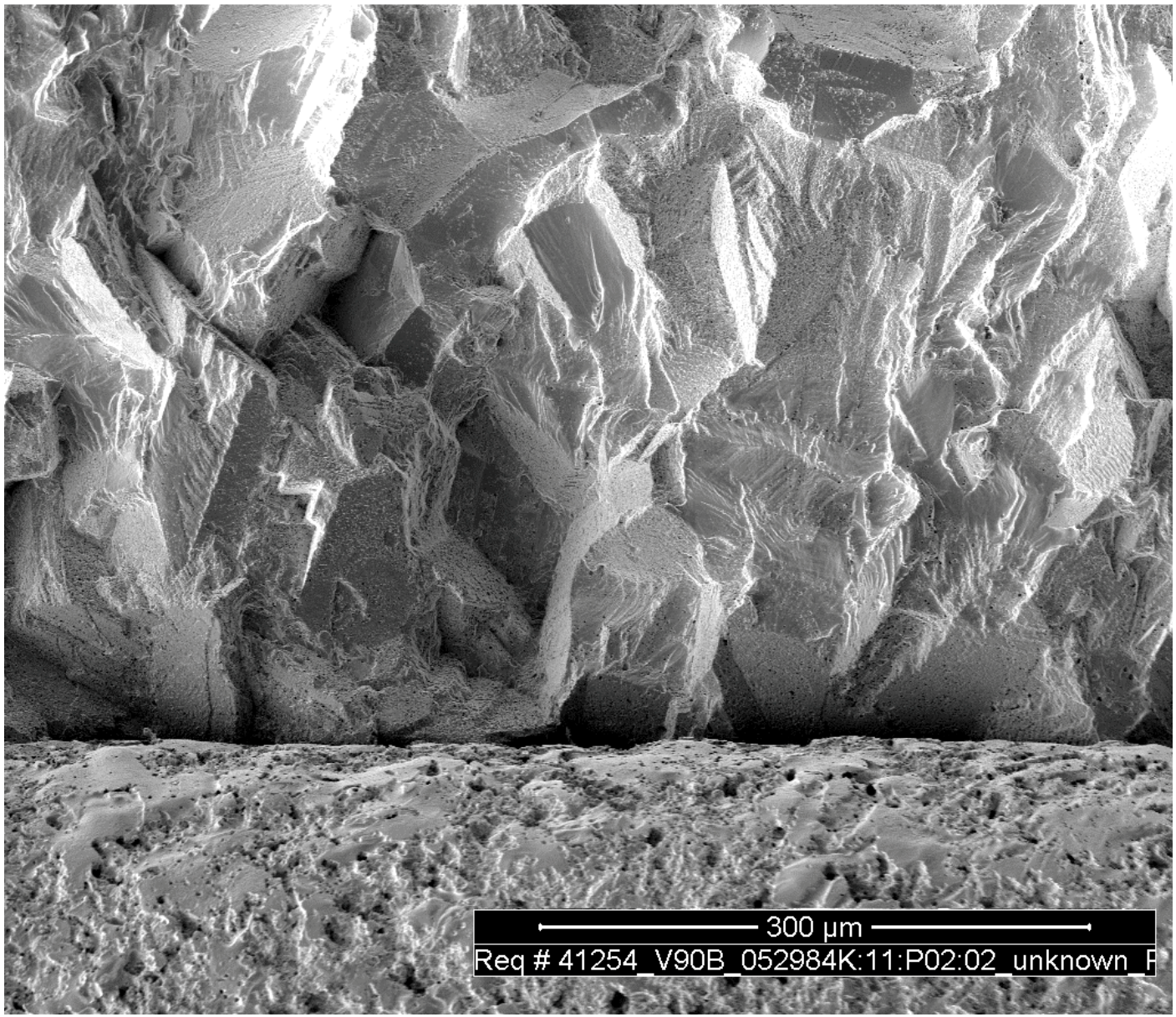

Figure 37. Cracking morphology at the beginning of the CGR test of Specimen B1CT07

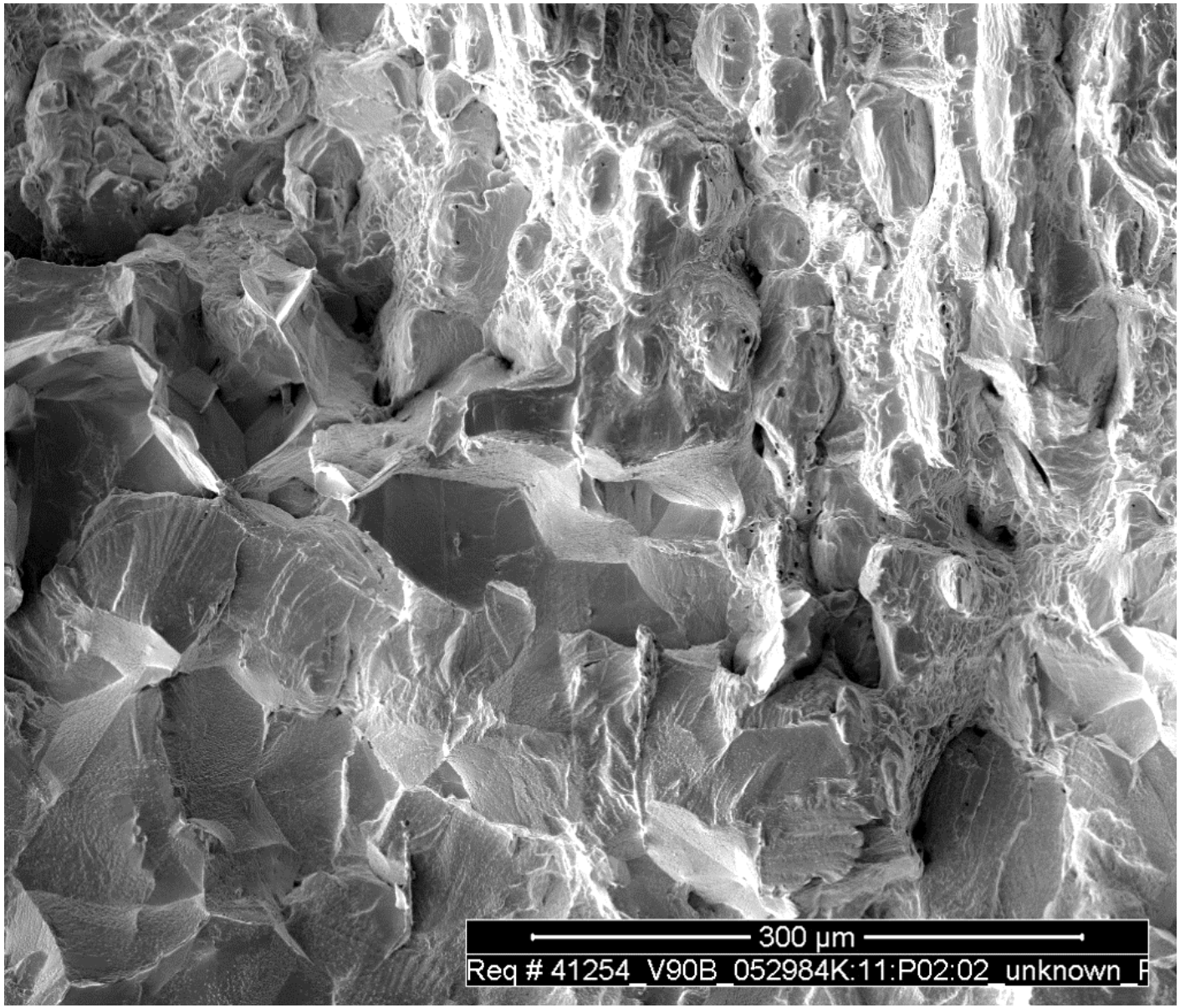

Figure 38. The transition region from the CGR to J-R curve test of Specimen B1CT07

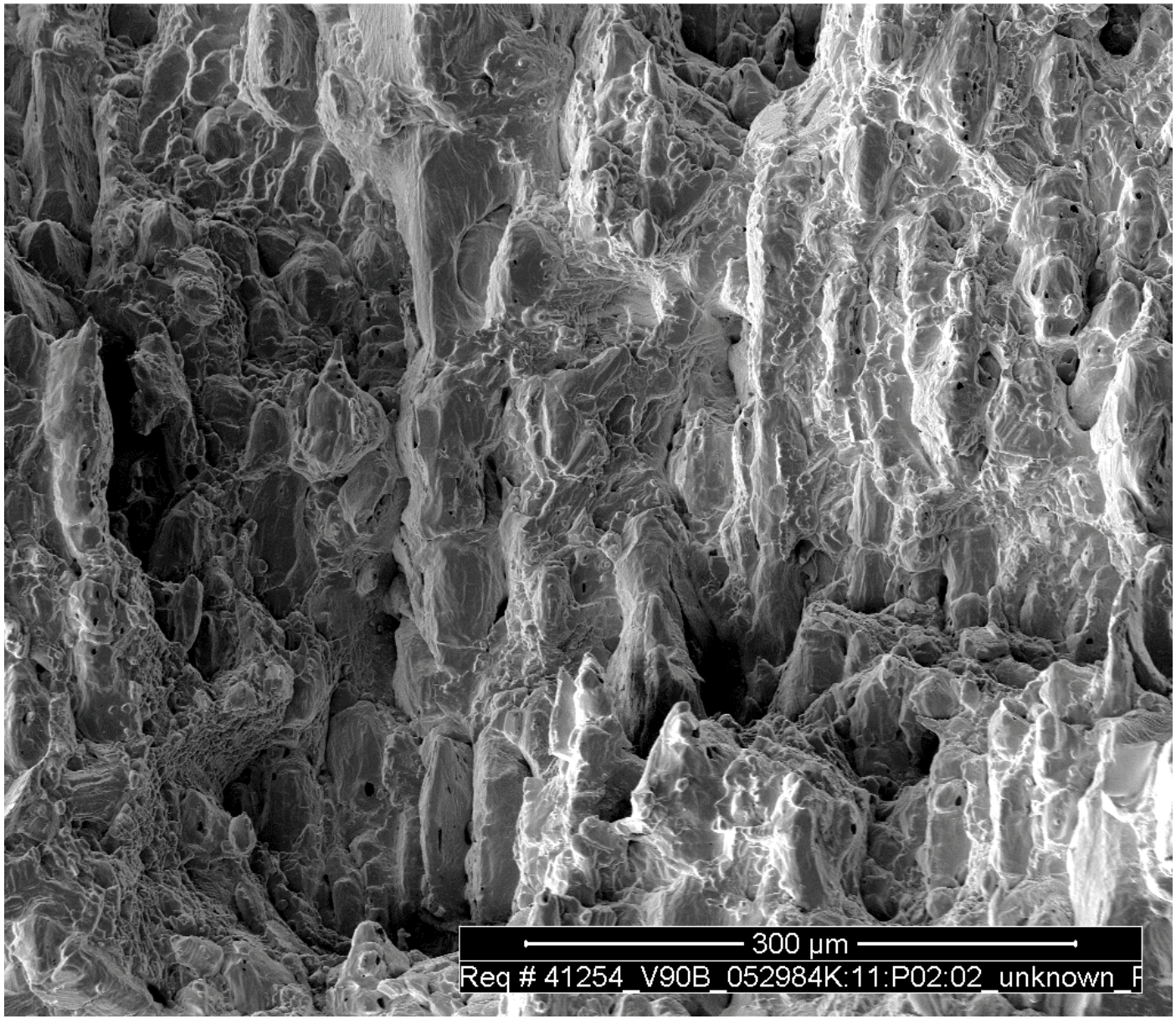

Figure 39. The J-R curve test region of Specimen B1CT07

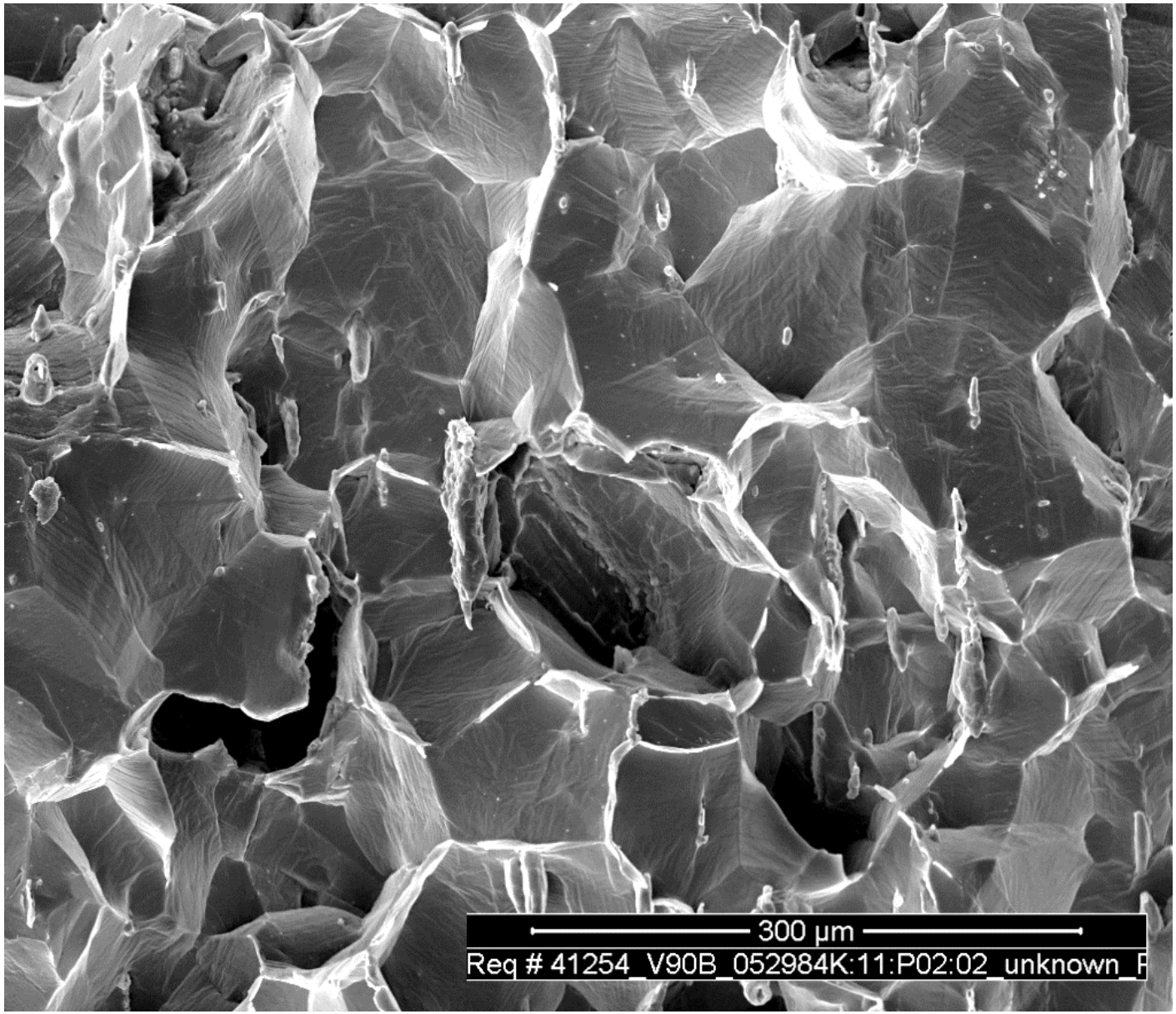

Figure 40. IG cracking in the post-JR fatigue region of Specimen B1CT07 in air at room temperature

4.5 Specimen B1CT09, ~47 dpa

Specimen B1CT09 was also cut from the source material "B1," the same convex corner plate used for the 39-dpa sample. The sample is machined from the area facing the reactor core, and therefore has the highest dose accumulation available in this study. The calculated displacement damage dose is about 47 dpa.

4.5.1 Crack Growth Rates

After the sample was loaded into the autoclave remotely with manipulators, the system was pressurized and heated to the test condition. During the process, a small tensile load of about 20 lb. was maintained on the sample. Next, the sample was soaked in the test environment for 9 days to stabilize the test condition. Table 7 summarizes all CGR results obtained from this sample. The time history of crack length and applied K are shown in Figure 41.

The test started with a triangle wave form at 1 Hz and a K_{max} of ~11.5 MPa $m^{1/2}$. The intention was to crack the sample at the lowest possible K_{max}, and gradually ramp up to higher K levels. As shown in Figure 41a, this initial K_{max} was too low and no crack extension was observed. After K_{max} was increased to ~15 MPa $m^{1/2}$, a CGR comparable to the anticipated fatigue growth rate under the same loading condition started to appear. The crack quickly stalled with increasing rise time and load ratio. After the crack was re-activated at ~16 MPa $m^{1/2}$, a well-behaved fatigue crack was finally obtained. Next, the load ration and rise time were gradually increased to induce environmentally enhanced cracking. The obtained cyclic CGRs are shown in Figure 42 as a function of the expected fatigue growth rate in air. After an enhancement factor (CGR_{env}/CGR_{air}) of 6.5 was obtained, the test was transitioned to a constant K test to measure the sample's SCC response. The first SCC test period (see Figure 41f) was conducted with a PPU every 2 hours. A CGR about 1.2×10^{-11} m/s was obtained over ~11 μm crack extension. After the PPU was removed, a slightly lower CGR of 8.0×10^{-12} m/s was recorded over ~9 μm crack extension.

Next, the crack was advanced under cyclic loading with a K_{max} of ~ 20 MPa $m^{1/2}$. No jump in the crack length was observed upon the increase of K_{max} (see Figure 41g). The degree of environmental enhancement remained strong as shown in Figure 42. After about 74 μm crack extension under cyclic loading, the test was set again to a constant K with PPU every 2 hours. A CGR of 1.8×10^{-11} m/s was recorded over 8 μm crack extension. Without PPU, the CGR declined to ~1.2×10^{-11} m/s.

The test was set to a cyclic mode one more time to increase the K_{max} to ~25 MPa $m^{1/2}$. Again, the environmentally enhanced cracking was evident, and the measured cyclic CGRs were more than 1 order of magnitude higher than that expected fatigue growth rates in air. With about 100 μm crack extension, the test was put back to a constant-K test with PPU every 2 hours. A SCC CGR of 2.5×10^{-11} m/s was measured over 9 μm crack extension. After the PPU was removed, a CGR of 1.0×10^{-11} m/s was measured over another 8 μm crack extension. After about 280 hours, the SCC CGR test concluded, and the sample was prepared for a J-R curve test in the test environment.

Table 7. Crack growth rates of Specimen B1CT09 (~47 dpa) in low-DO, high-purity water

Test Period [1]	Test Time (hr)	Test Temp. (°C)	Load Ratio	Rise Time (s)	Return Time (s)	Hold Time (s)	K_{max} (MPa $m^{1/2}$)	ΔK (MPa $m^{1/2}$)	CGR in Env. (m/s)	CGR in Air (m/s)	Crack Length (mm)
Start											5.710
a	5.3	315	0.34	0.4	0.4	0.1	11.5	7.6	5.12E-10	1.25E-08	5.714
b	24.6	314	0.33	0.4	0.4	0.1	12.5	8.3	negligible	1.64E-08	5.714
c	46.6	315	0.33	0.4	0.4	0.1	13.5	9.0	negligible	2.09E-08	5.713
d	50.8	314	0.33	0.4	0.4	0.1	14.5	9.7	negligible	2.64E-08	5.717
e [2]	80.5	315	0.30	0.4	0.4	0.1	14.9	10.5	2.98E-09	3.22E-08	5.757
f [2]	99.1	314	0.30	0.4	0.40	0.1	15.1	10.5	1.77E-08	3.32E-08	5.934
g	113.9	314	0.39	1.9	1.9	0.6	14.5	8.9	2.49E-10	4.35E-09	5.948
h [2]	137.2	314	0.35	0.8	0.8	0.2	15.1	9.9	1.26E-08	1.43E-08	6.103
i [2]	166.1	314	0.39	1.9	1.9	0.6	15.0	9.1	2.68E-09	4.74E-09	6.204
j	209.8	314	0.45	3.7	3.7	1.3	14.8	8.1	3.20E-10	1.79E-09	6.228
k [2]	234.2	314	0.45	1.5	1.5	0.5	15.2	8.3	4.68E-09	4.78E-09	6.314
l	281.5	314	0.50	3.6	3.6	1.4	15.0	7.5	2.75E-10	1.45E-09	6.333
m	290.2	314	0.50	1.8	1.8	0.7	15.9	7.9	2.11E-09	3.49E-09	6.352
n	307.4	314	0.50	3.7	3.7	1.3	15.9	8.0	7.23E-10	1.77E-09	6.368
o	330.9	314	0.49	7.4	3.7	2.6	16.1	8.1	3.64E-10	9.30E-10	6.387
p	354.4	314	0.50	22.1	3.7	7.9	16.0	8.1	2.11E-10	3.07E-10	6.396
q	377.9	314	0.46	75.1	9.0	24.9	16.3	8.7	2.17E-10	1.14E-10	6.410
r	402.1	314	0.47	186.3	8.9	63.7	16.2	8.5	1.70E-10	4.20E-11	6.417
s	425.8	314	0.47	373.5	9.0	126.5	16.3	8.6	1.09E-10	2.17E-11	6.425
t	449.7	314	0.47	746.5	9.0	253.5	16.2	8.6	6.93E-11	1.08E-11	6.428
1	570.0	314	0.50	12	12	7200	16.4	8.2	1.20E-11	9.97E-13	6.439
2	714.3	314	1	-	-	-	16.6	-	7.98E-12	-	6.448
u	737.7	314	0.48	191.6	9.20	58.4	19.8	10.3	6.39E-10	7.77E-11	6.500
v	762.0	314	0.53	373.6	8.97	126.4	19.8	9.3	2.17E-10	2.99E-11	6.514
w	786.3	314	0.55	739.1	8.87	260.9	19.9	8.9	1.48E-10	1.35E-11	6.522
3	882.1	314	0.55	12.0	12.00	7200.0	20.1	9.0	1.75E-11	1.43E-12	6.530
4	1,050.6	314	1	-	-	-	20.2	-	1.24E-11	-	6.540
x	1,073.6	314	0.59	189.6	9.10	60.4	24.9	10.1	8.29E-10	8.22E-11	6.600
y	1,105.6	314	0.62	371.7	8.92	128.3	25.0	9.4	2.37E-10	3.37E-11	6.617
z	1,145.7	314	0.62	744.4	8.93	255.6	25.1	9.5	1.77E-10	1.74E-11	6.639
5	1,241.6	314	0.62	12.0	12.00	7200.0	25.2	9.6	2.46E-11	1.85E-12	6.647
6	1,433.9	314	1	-	-	-	25.3	-	1.04E-11	-	6.657
Complete											

[1] Cyclic test periods are named in alphabetical order, and constant-K test periods are named in numerical order.
[2] Crack growth rate in the later part of the test period is reported.

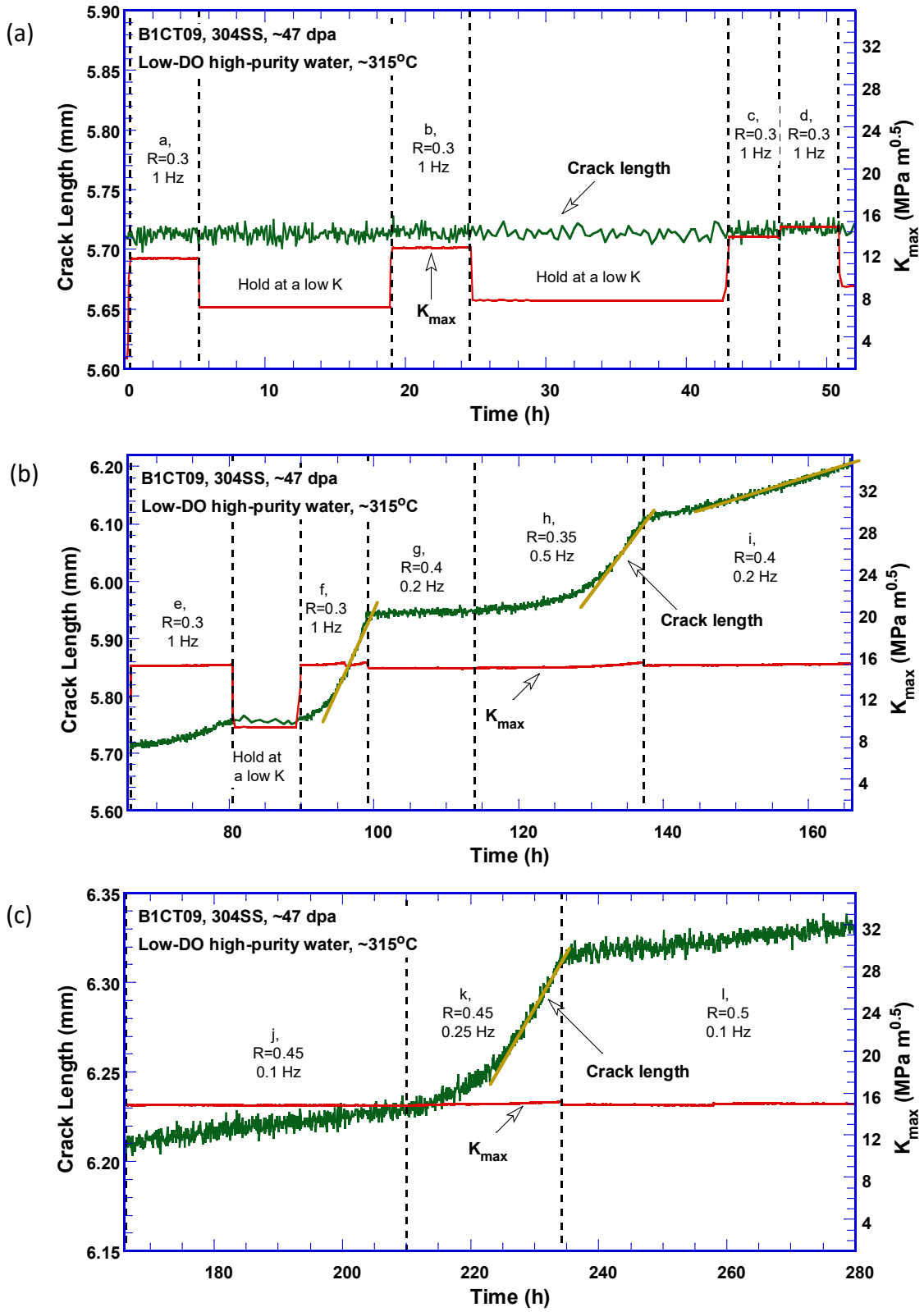

Figure 41. Crack-length-vs.-time plot of Specimen B1CT09 (~47 dpa) tested in low-DO, high-purity water: test periods (a) a–d, (b) e–i, (c) j–l, (d) m–p, (e) q–t, (f) 1–2, (g) u–w, (h) 3–4, (i) x–z, and (j) 5–6

(d)

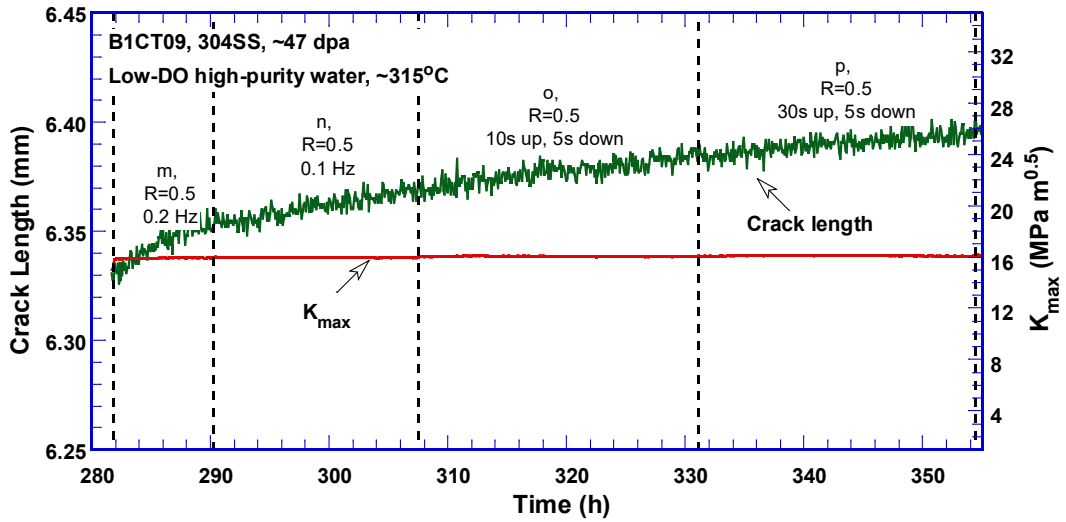

(e)

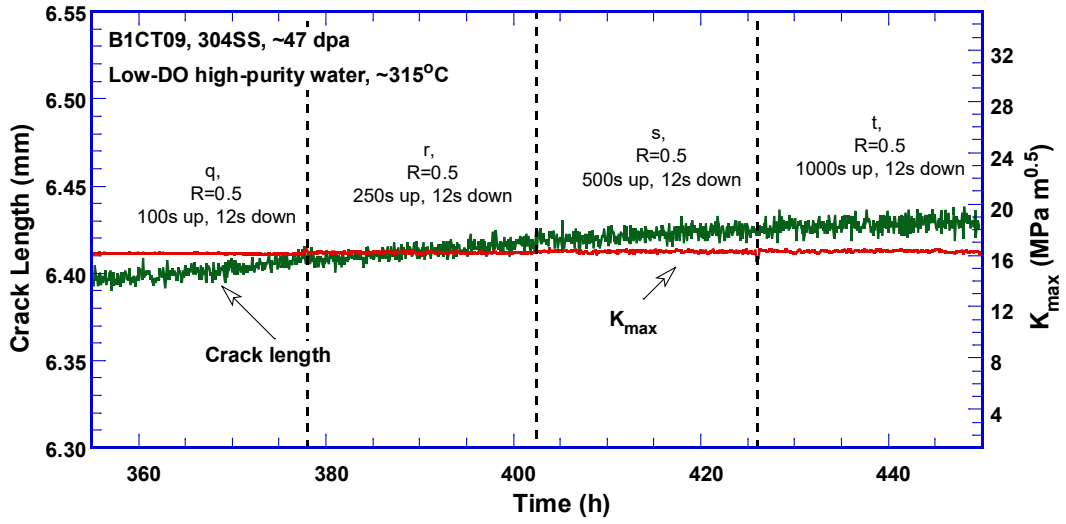

(f)

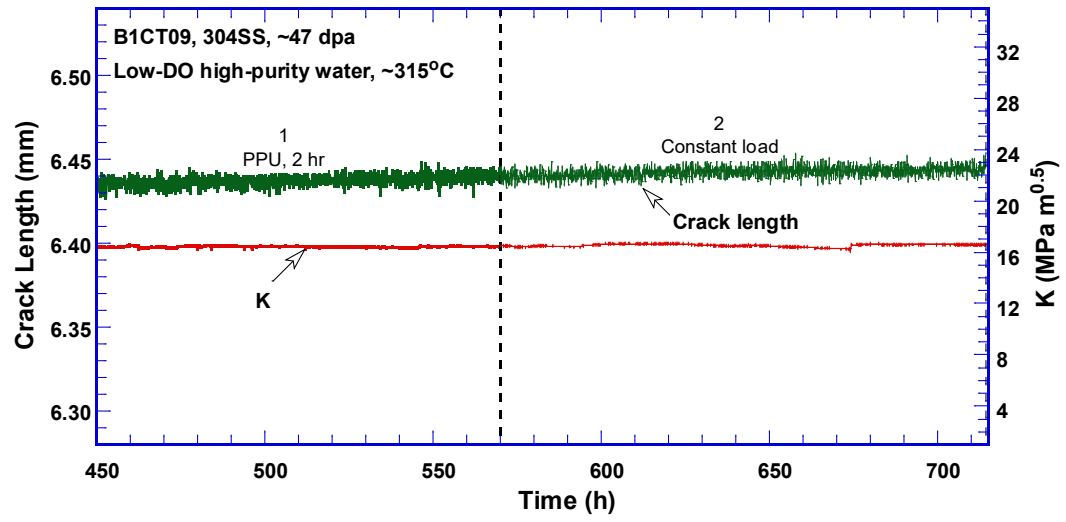

Figure 41. (Cont.)

(g)

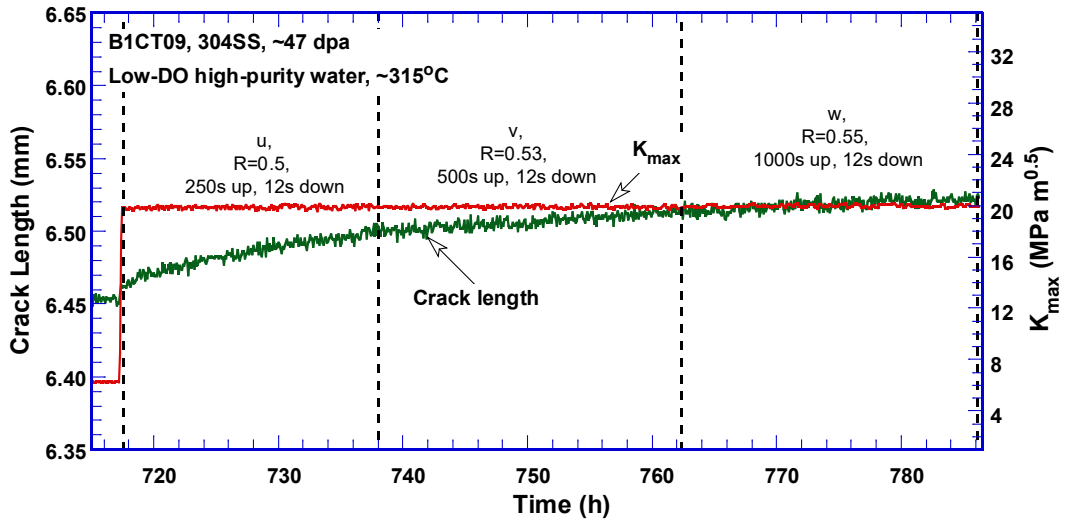

(h)

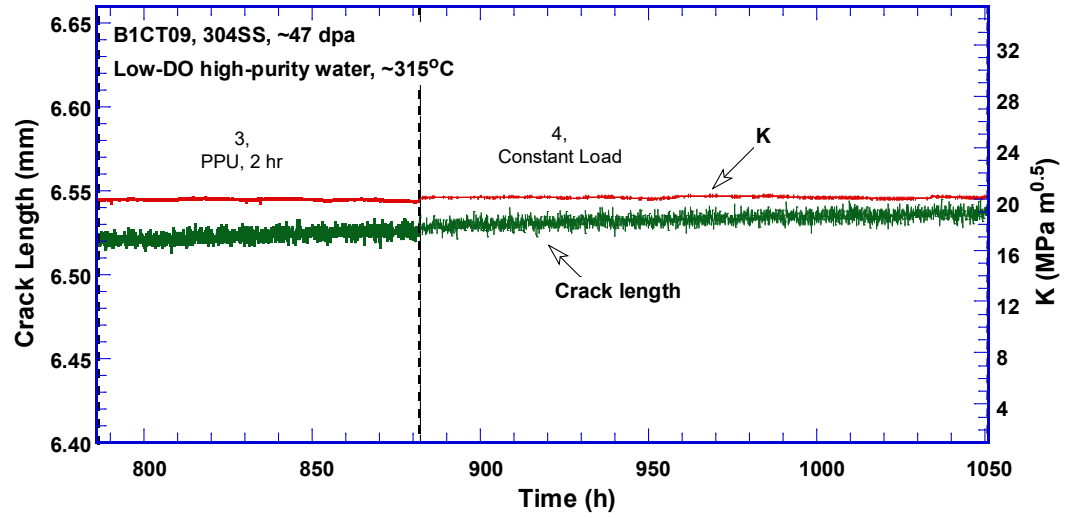

(i)

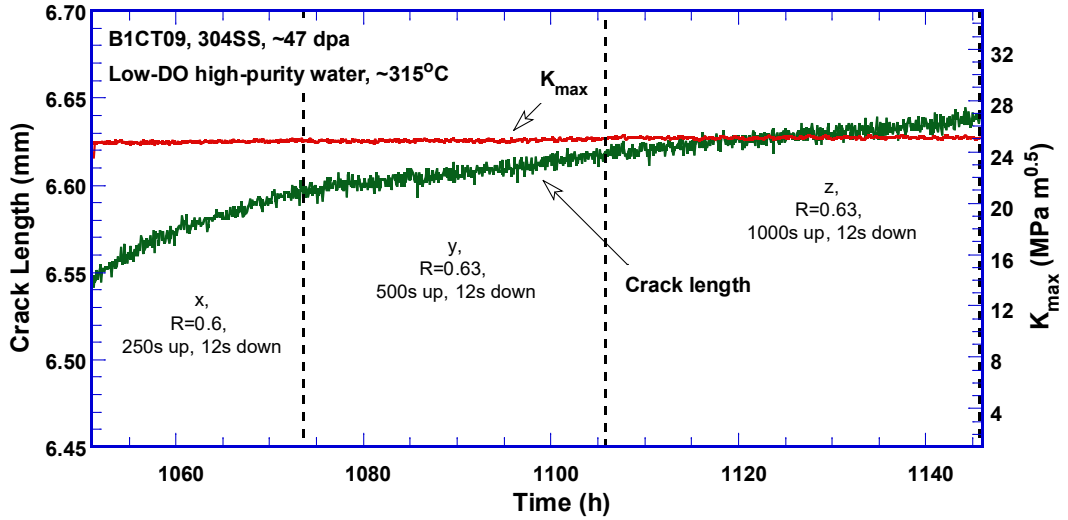

Figure 41. (Cont.)

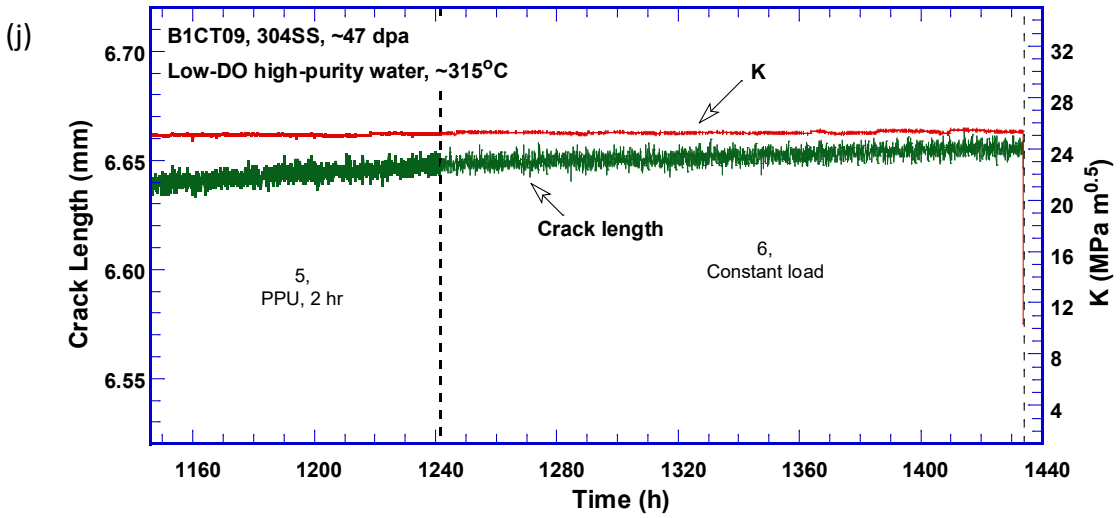

Figure 41. (Cont.)

Figure 42 shows the cyclic CGRs obtained from this sample as a function of fatigue growth rate in air. The cracking behavior of this sample is very similar to that of the 39-dpa sample with many failed attempts to initiate an enhanced cracking in the test environment (the data points below the diagonal line in the figure). When the environmental enhancement was established in the sample, an enhancement factor close to 10× could be maintained in this sample.

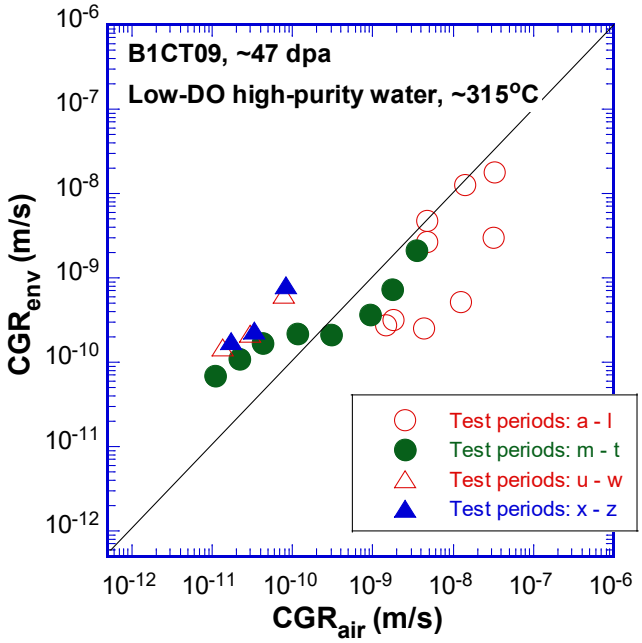

Figure 42. Cyclic CGRs of Specimen B1CT09 (~47 dpa) tested in low-DO, high-purity water

The SCC behavior of this sample is nearly identical to that of the 39-dpa specimen. All CGRs are below the NUREG-0313 disposition curve, and the differences between the data points with and without PPU are small. A weak K dependency can be seen for the CGRs with PPU.

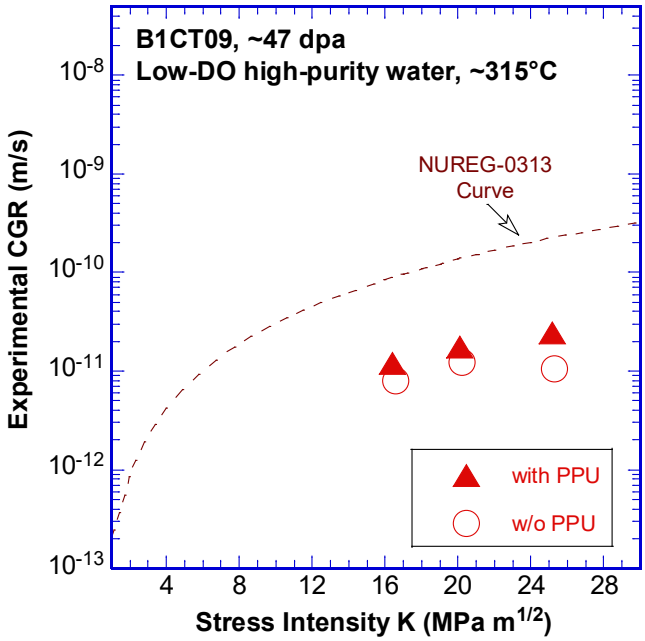

Figure 43. SCC CGRs of Specimen B1CT09 (~47 dpa) tested in low-DO, high-purity water

4.5.2 Fracture Toughness J-R Curve

Prior to the J-R curve test, the sample was cyclically loaded for about 10–20 cycles to break any unbroken ligaments that might have developed in the SCC test. No abnormal cracking behavior was observed during these cycles. With an initial a/W of 0.55, a J-R curve test was performed on this sample at a constant displacement rate of 0.08 mm/min. The resulting J-Δa data are shown in Figure 44. The Δa_{max} and J_{max} for the sample are also included in the figure. The J-Δa data was fitted to a power-law relationship, and a correlation of $J = 80 \times \Delta a^{0.04}$ was obtained. The J value at the 0.2-mm off-set line was about 75 kJ/m^2. Although this J_Q value is comparable to those of SS welds at ~15 and ~39 dpa, the power exponent of this J-R curve is near zero. It is clear that very little cracking resistance should be anticipated for the reactor core materials at this dose level.

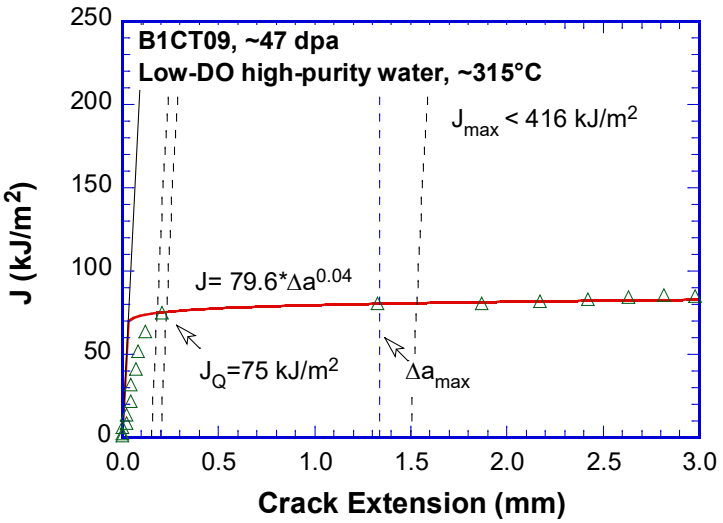

Figure 44. J-R curve of Specimen B1CT09 (~47 dpa) tested at ~315°C

4.5.3 Fracture Morphology

After the J-R curve test, the sample was cyclically loaded and pulled apart in air at room temperature. The sample was cleaned, and several replicas were produced from its fracture surface. After further decontamination, the replicas were examined with a SEM. Figure 45 shows the entire fracture surface. The CGR crack front tilts toward one side of the sample, indicating a small misalignment issue during the CGR test. Figure 46 is an enlarged view of the region along the sample's centerline. The crack propagation goes from bottom to top in the picture. The contrast between the CGR and J-R test regions is evident. Details of the CGR test region can be seen in Figure 47 and Figure 48. The initial CGR test region showed a mostly TG morphology with some IG facets. The IG morphology became more pronounced toward the end of CGR test, where a moderated CGR in the order of 1-3 × 10^{-11} m/s was recorded.

The J-R test region is a mixed-mode fracture, as shown in Figure 49. Elongated brittle areas parallel to the cracking direction can be seen on the fracture surface. These narrow brittle regions may be related ferrite stringers in the materials. Despite its low cracking resistance, ductile dimples remained the dominant fracture morphology in this sample during the J-R test. For the post-JR fatigue region, the fracture morphology was once again fully IG (see Figure 50), identical to those observed at ~15 and ~39 dpa. Note that this brittle IG cracking occurred at room temperature without high temperature water environments.

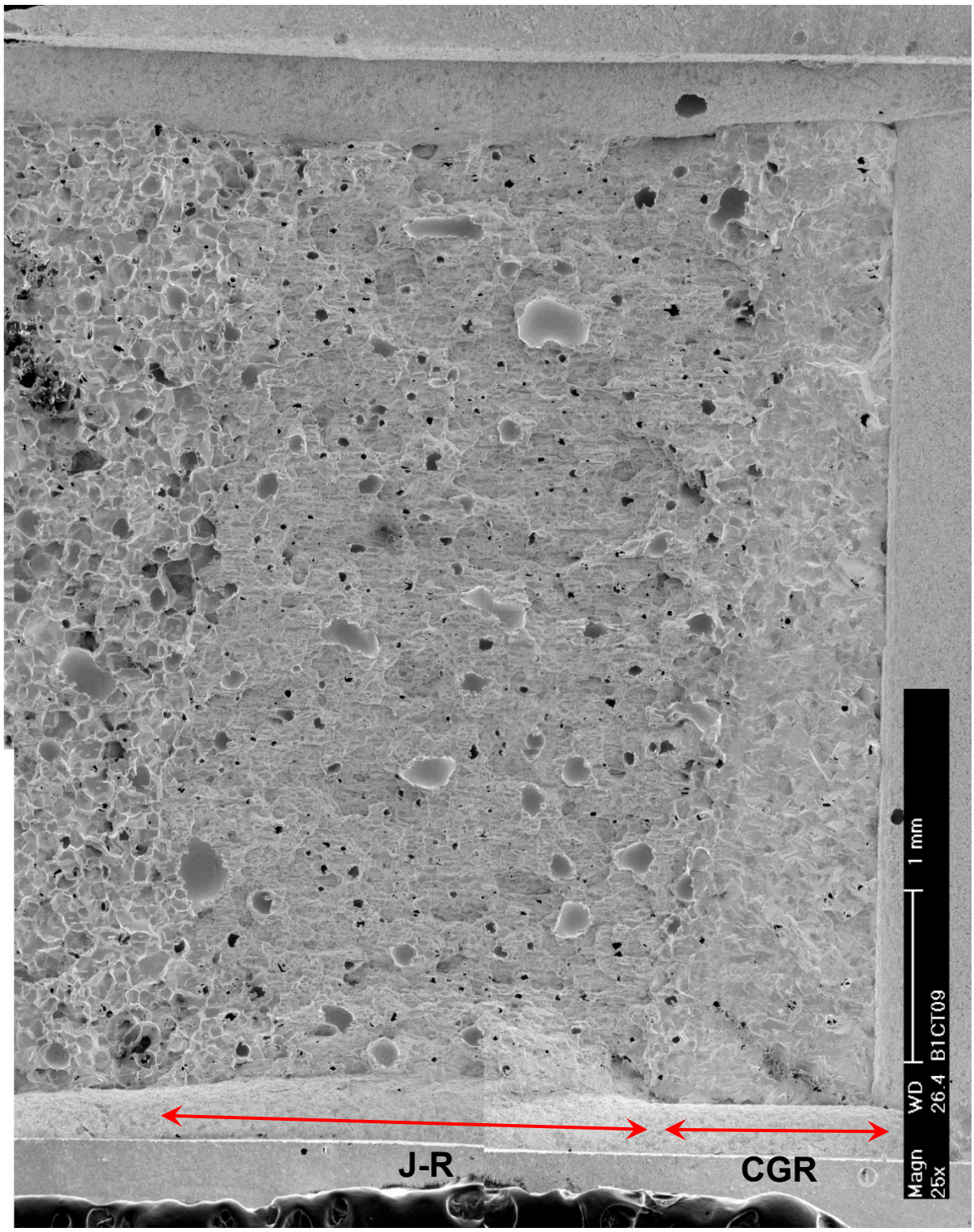

Figure 45. Fracture surface of Specimen B1CT09, ~47 dpa

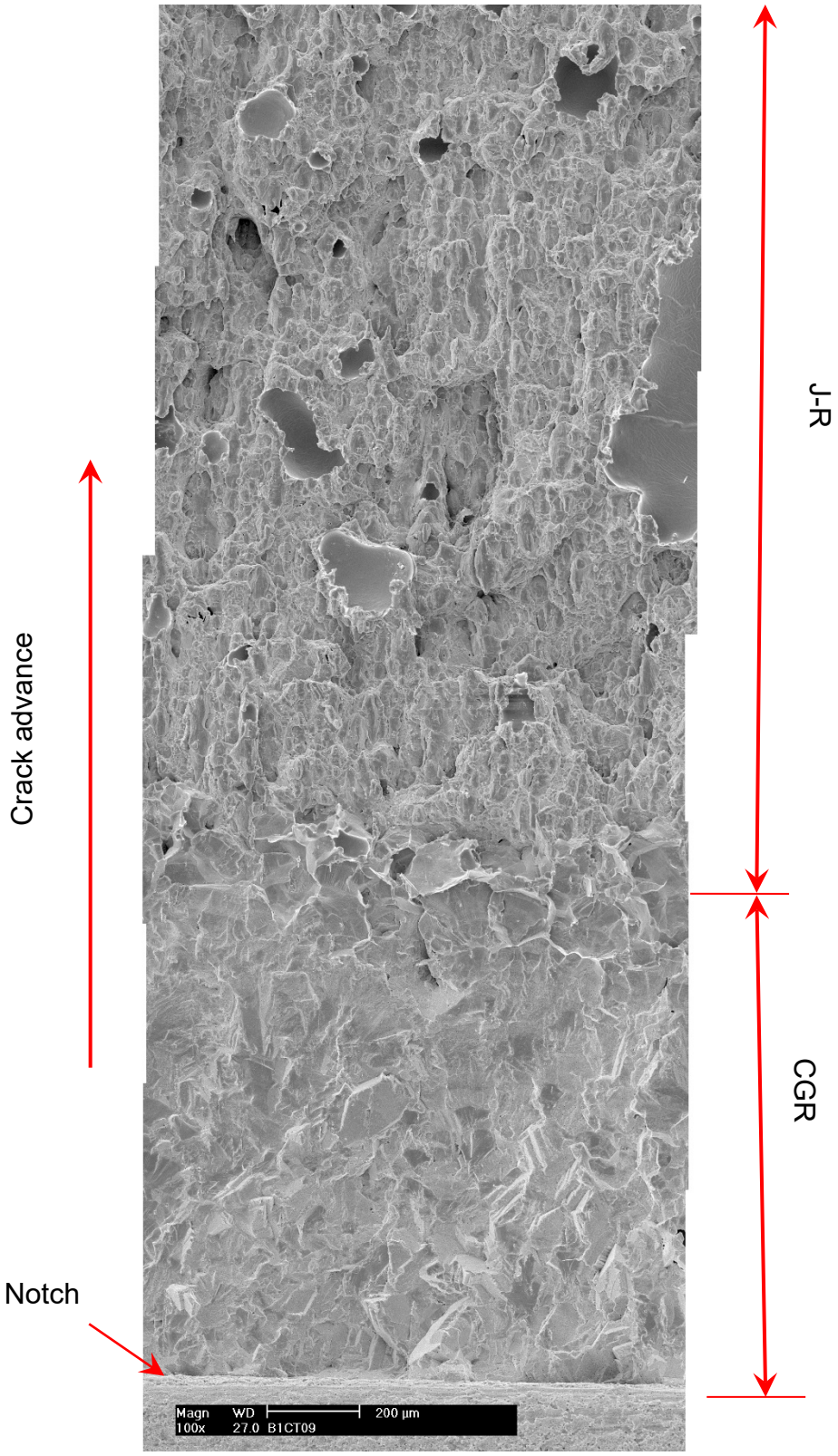

Figure 46. Enlarged view along the centerline of Specimen B1CT09

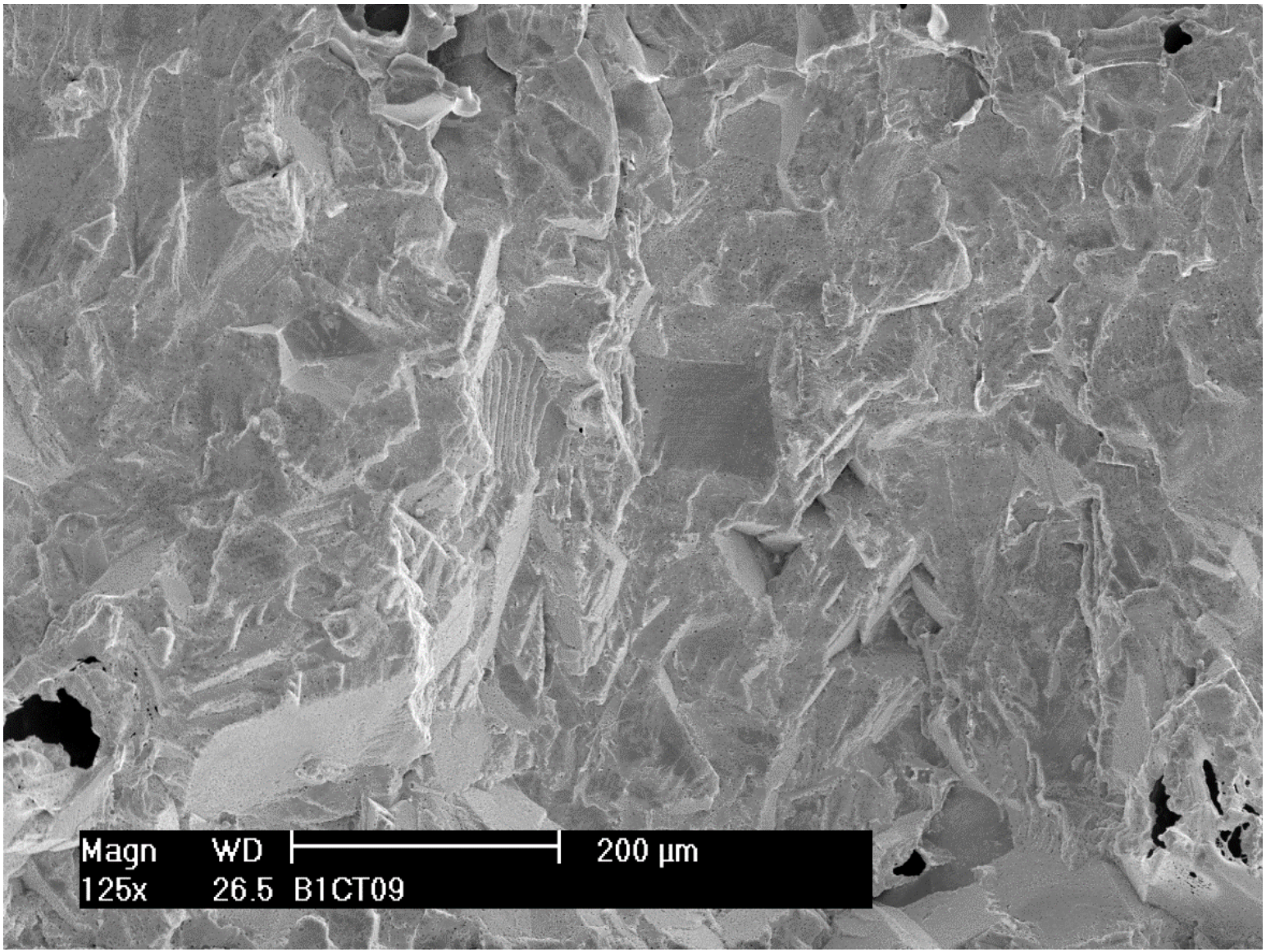

Figure 47. Mixed IG and TG morphology during the CGR test in Specimen B1CT09

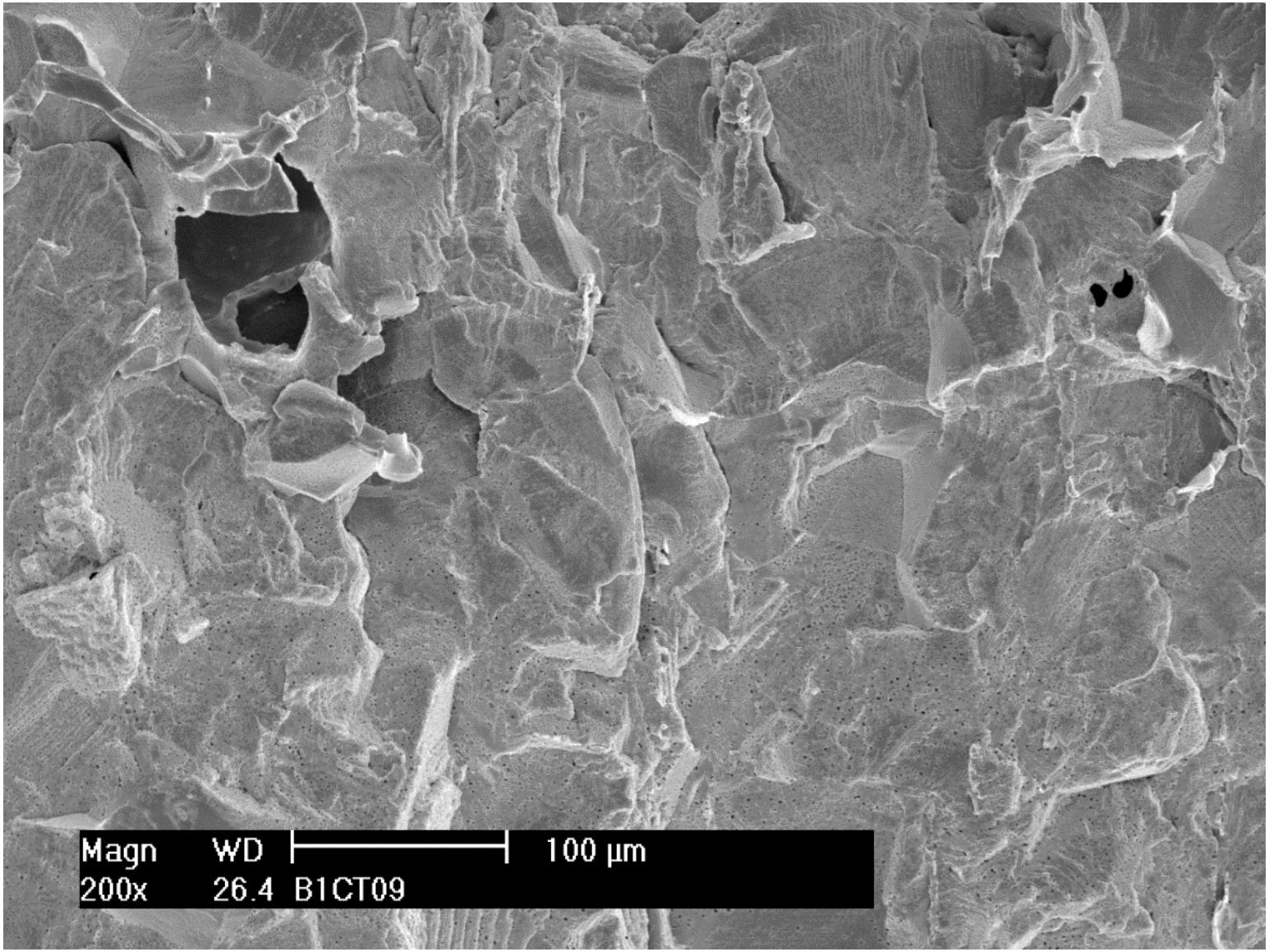

Figure 48. IG cracking at the end of CGR test in Specimen B1CT09

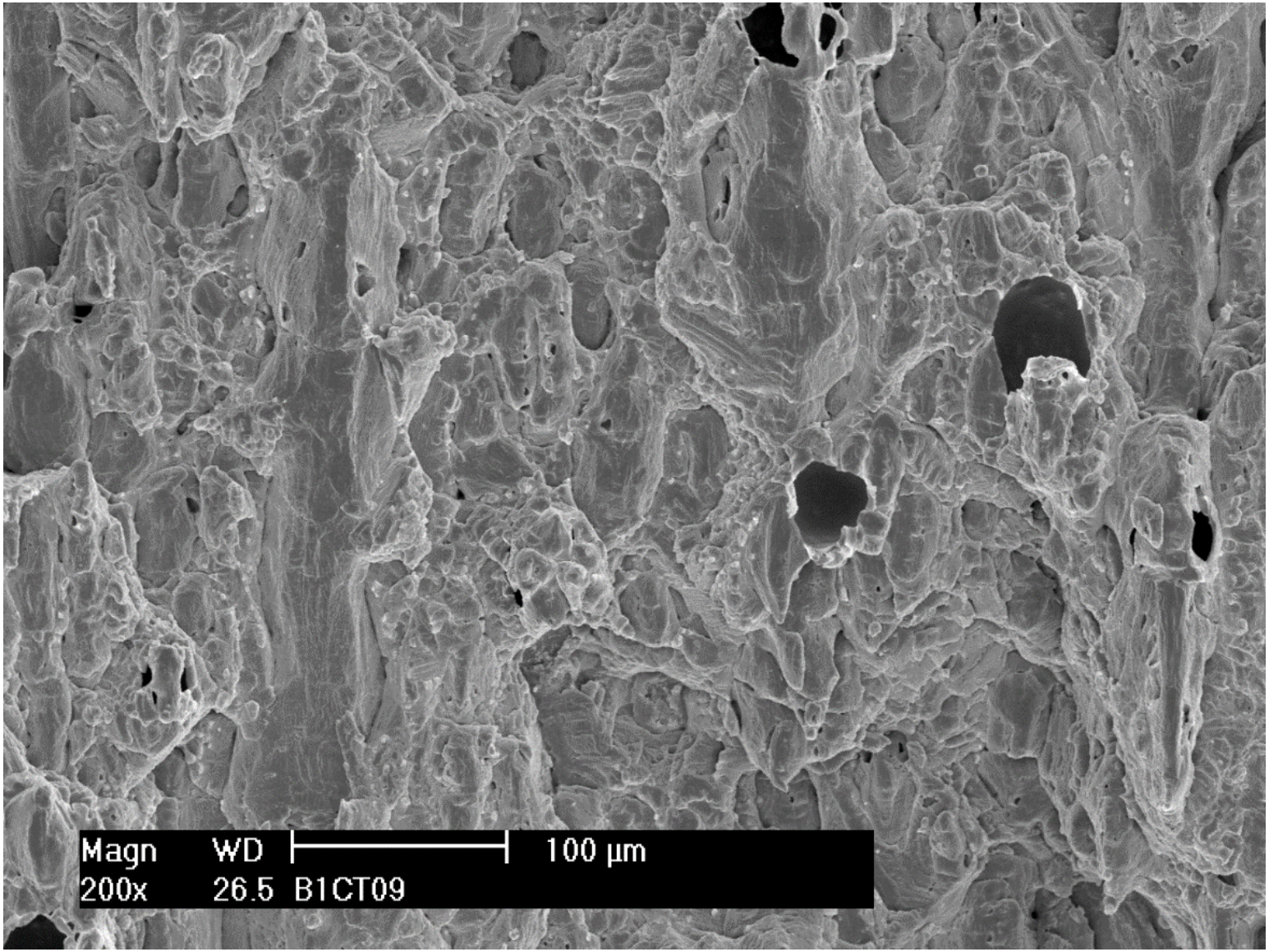

Figure 49. Stringers and mixed mode fracture during the J-R curve test in Specimen B1CT09

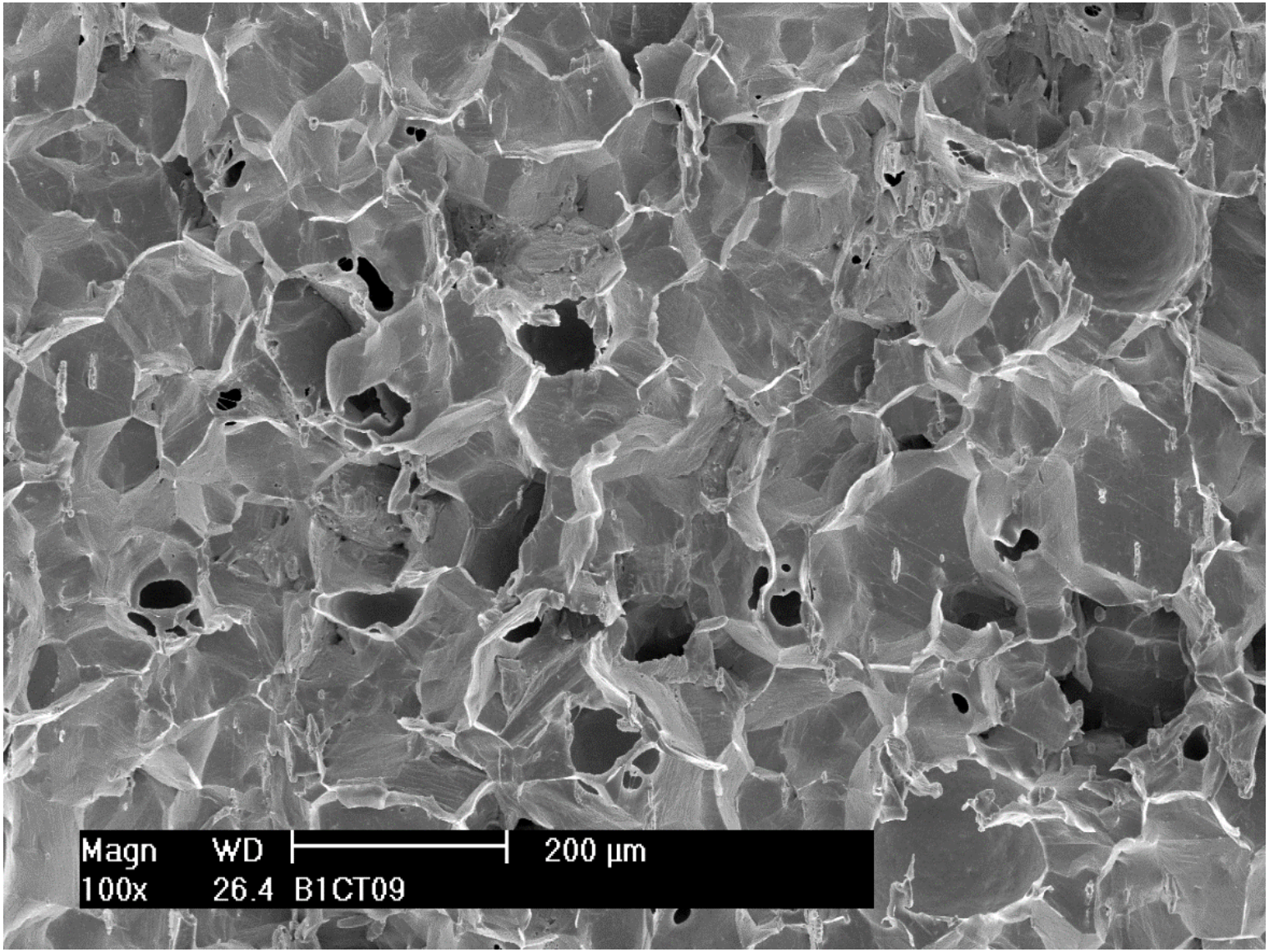

Figure 50. IG morphology resulting from the post-test cyclic loading at room temperature in Specimen B1CT09

4.6 Specimen B1CT08, ~47 dpa

Specimen B1CT08 was the second 47-dpa sample tested in this study. The sample was machined from the same location where Specimen B1CT09 was cut, and the two samples were essentially next to each other in the source material "B1." Because the source material was at the convex corner of the reactor core baffle, the dose gradient resulting from flux attenuation is relatively flat within the plate. The calculated dose of this sample was ~47 dpa.

4.6.1 Crack Growth Rates

After the sample was installed in the autoclave, the system was pressurized and heated slowly to ~315°C. A tensile load of about 70 lb. was maintained on the sample during heating. This load was higher than what we normally use (20-30 lb.). However, this applied load would only result in a K of ~7 MPa $m^{1/2}$, significantly lower than that could cause any damage to the sample. All CGR results from this sample are summarized in Table 8. Figure 51 shows the time history of crack length and applied K for this sample.

After the sample was soaked in the PWR water for 6 days, the cyclic CGR test was started with a K_{max} of ~12 MPa $m^{1/2}$ at a load ratio of 0.35 and 0.1 Hz. Similar to the first 47-dpa sample, pre-cracking proved to be difficult for this sample. The applied K_{max} had to be repeatedly increased to initiate the crack. Eventually, after ~380 hours of cyclic loading, a CGR slightly below the anticipated fatigue growth rate in air was obtained with a K_{max} of ~18 MPa $m^{1/2}$ (see Figure 51a). After ~136 μm crack extension, the measured CGR became comparable to the fatigue growth rate in air, and environmentally enhanced cracking started to appear as the rise time and load ratio increased. By the end of the cyclic CGR test, the measured CGR was about a factor of ~4 higher than that of fatigue growth rate in air.

Next, the test was set to a constant K with a PPU every 2 hours. The applied K was about 19.8 MPa $m^{1/2}$. A SCC CGR of 1.9×10^{-11} m/s was recorded over ~100 hours. After the PPU was removed, the measured CGR was lowered 9.0×10^{-12} m/s. These values are similar to those observed in the first 47-dpa sample at 16 and 20 MPa $m^{1/2}$.

After the SCC CGRs were measured at the first K level, the crack was advanced with cyclic loading at a K_{max} of ~23.5 MPa $m^{1/2}$. No jump in crack length was observed when the K was increased (see Figure 51e). The crack propagated as expected, and the degree of environmental enhancement remained at the same level as that in the previous cyclic CGR period. The test was then set to a constant K with PPU every 2 hours. The applied K was about 23.9 MPa $m^{1/2}$. A SCC CGR of 2.2×10^{-11} m/s was recorded over 126 hours.

Until this point, the SCC response of this sample was almost identical to that of the first 47-dpa sample. No elevated cracking susceptibility was observed. However, after the PPU was removed, the CGR started to increase unexpectedly (see Figure 51f). After about 2 hours under a constant K, a CGR of 4.1×10^{-9} m/s was recorded. This growth rate is more than 2 orders of magnitude higher than the CGR observed at the same K level with PPU. The CGR continued to increase over the next 18 hours, approaching 4.3×10^{-8} m/s at the highest. This extremely high growth rate challenged our load shedding scheme, which was designed for tests with much lower growth rates. Consequently, a near-constant K condition could no longer be maintained in the test, leading to a rising K condition. More details of test period 4 and its sub-segments are shown in Figure 51, panels g–k.

To preserve the remaining ligament, the applied K was reduced and held at ~5.5 MPa $m^{1/2}$. The measured CGR slowed considerably but was still higher than anticipated at such a low K level. After about 132 hours, the K was again increased to ~17 MPa $m^{1/2}$. A stepwise increase in the crack length, about ~70 μm, was observed upon the load increase. If this jump in crack length was counted toward crack growth in the test segment, the average CGR would be significantly higher (10×) than the stable crack growth measured with DCPD (see Figure 51h). At ~17 MPa $m^{1/2}$, the crack seemed stalled and the measured CGR was only 4.8×10^{-12} m/s. However, when the K was increased again, to ~30 MPa $m^{1/2}$, another huge jump in crack length was observed upon loading. Obviously, these large, unstable cracking events dominated crack propagation, and the stable crack advance during the test segments became secondary.

Note that, because of the unstable cracking behavior in this sample, the DCPD measurement significantly underestimated the crack length during the test, leading to a much lower estimate of the actual K for the moving crack front. This affected our judgement during the test to alter the applied K or load shed. Consequently, in the following test segments, the actual applied K values (after the post-test correction) were much higher than we thought during the test.

After the K was increased to ~30 MPa $m^{1/2}$, rapid growth behavior was noticed which was very different from what had been observed at lower Ks was noticed. Despite the fact that the applied load was reduced three times during the test segment *4g* (see Figure 51i), the crack did not slow; in fact, it accelerated over time, approaching 4.3×10^{-8} m/s at the end of the test segment. A single PPU was also applied during this test segment, resulting a stepwise increase of about 125 μm upon reloading. The high-CGR behavior persisted even when the K was decreased to ~32 MP $m^{1/2}$ (test segment *4i*) and then to ~25 MPa $m^{1/2}$ (test segment *4i*). The measured CGRs hovered around 5×10^{-8} m/s constantly. Only after the K was reduced to ~11 MPa $m^{1/2}$ (test segment *4j*), did the repaid growth start to disappear gradually, eventually reaching a stable growth rate of 2.3×10^{-11} m/s.

After ~128 hours, the applied K was increased again to ~66 MPa $m^{1/2}$. A huge stepwise increase of about 950 μm was observed upon loading. A stable growth rate of 4.3×10^{-8} m/s was sustained after this huge jump in crack length. After about 1 hour in this condition, the sample fractured unexpectedly, and the test was terminated. Both the large jumps at the load increases and the very high growth rates observed in this sample suggest unstable cracking behavior. The exact loading or material conditions that trigger such a cracking instability are not clear at present.

Table 8. Crack growth rates of Specimen B1CT08 (~47 dpa) in PWR water

Test Period [1]	Test Time (hr)	Test Temp. (°C)	Load Ratio	Rise Time (s)	Return Time (s)	Hold Time (s)	K_{max} (MPa $m^{1/2}$)	ΔK (MPa $m^{1/2}$)	CGR in Env. (m/s)	CGR in Air (m/s)	Crack Length (mm)
Start	1.1										5.580
Multiple trials	382.0	314	0.3-0.4	~1.7	~1.7	~0.3	12.3-17.5	7.9-12	negligible	~1.0E-8	5.596
a [2]	397.7	313	0.33	1.8	1.8	0.2	18.1	12.1	8.79E-09	1.24E-08	5.732
b	413.6	313	0.35	4.3	4.3	0.7	18.6	12.1	9.23E-09	5.05E-09	5.953
c	435.2	313	0.38	8.6	4.3	1.4	19.2	11.8	3.62E-09	2.47E-09	6.117
d	461.4	313	0.41	25.6	4.3	4.4	19.3	11.4	1.23E-09	7.49E-10	6.206
e	478.6	313	0.47	50.3	10.1	9.7	19.4	10.2	5.83E-10	2.82E-10	6.234
f	503.1	313	0.47	100.7	10.1	19.3	19.4	10.2	3.94E-10	1.44E-10	6.254
g	526.7	313	0.47	210.0	10.1	40.0	19.4	10.4	2.04E-10	7.11E-11	6.266
h	551.5	313	0.47	420.4	10.1	79.6	19.6	10.5	1.64E-10	3.67E-11	6.277
i	574.9	313	0.46	841.4	10.1	158.6	19.6	10.5	6.30E-11	1.87E-11	6.284
1	671.0	313	0.50	12	12	7200	19.8	9.9	1.88E-11	1.84E-12	6.299
2	767.0	313	1	-	-	-	19.8	-	9.00E-12	-	6.303
j	791.8	313	0.53	105.6	10.1	19.4	23.5	11.0	8.17E-10	1.84E-10	6.355
k	814.8	313	0.53	211.0	10.1	39.0	23.6	11.0	4.05E-10	9.26E-11	6.379
l	838.3	313	0.53	421.9	10.1	78.1	23.7	11.1	2.68E-10	4.69E-11	6.397
m	863.1	313	0.53	845.6	10.1	154.4	23.8	11.2	1.19E-10	2.45E-11	6.403
3	989.1	313	0.57	12	12	7200	23.9	10.3	2.19E-11	2.23E-12	6.424
4a	997.1	313	1	-	-	-	24.4	-	4.09E-09	-	6.493
4b	1,004.5	313	1	-	-	-	24.5	-	4.92E-10	-	6.510
4c [3]	1,015.0	313	1	-	-	-	24.3-26.0	-	9.06E-09	-	6.883
4d [3]	1,018.7	313	1	-	-	-	26.0-29.2	-	4.29E-08	-	7.446
4e	1,150.7	313	1	-	-	-	5.5	-	1.50E-11	-	7.496
4f	1,227.4	313	1	-	-	-	17.0	-	4.00E-12	-	7.564
4g [2,3]	1,234.8	313	1	-	-	-	30.0-39.0	-	4.28E-08	-	8.262
4h [2,3]	1,237.3	313	1	-	-	-	32.7-37.0	-	5.78E-08	-	8.891
4i [2,3]	1,241.0	313	1	-	-	-	25.3-30.9	-	5.35E-08	-	9.239
4j [2]	1,368.5	313	1	-	-	-	10.9	-	2.33E-11	-	9.449
4k [2,3]	1,369.5	313	1	-	-	-	66.5-77.6	-	4.34E-08	-	10.573
Complete											

[1] Cyclic test periods are named in alphabetical order, and constant-K test periods are named in numerical order.
[2] Crack growth rate in the later part of the test period is reported.
[3] A near-constant K condition cannot be maintained with the rapid crack growth. K values at the beginning and end of the test segment are reported instead.

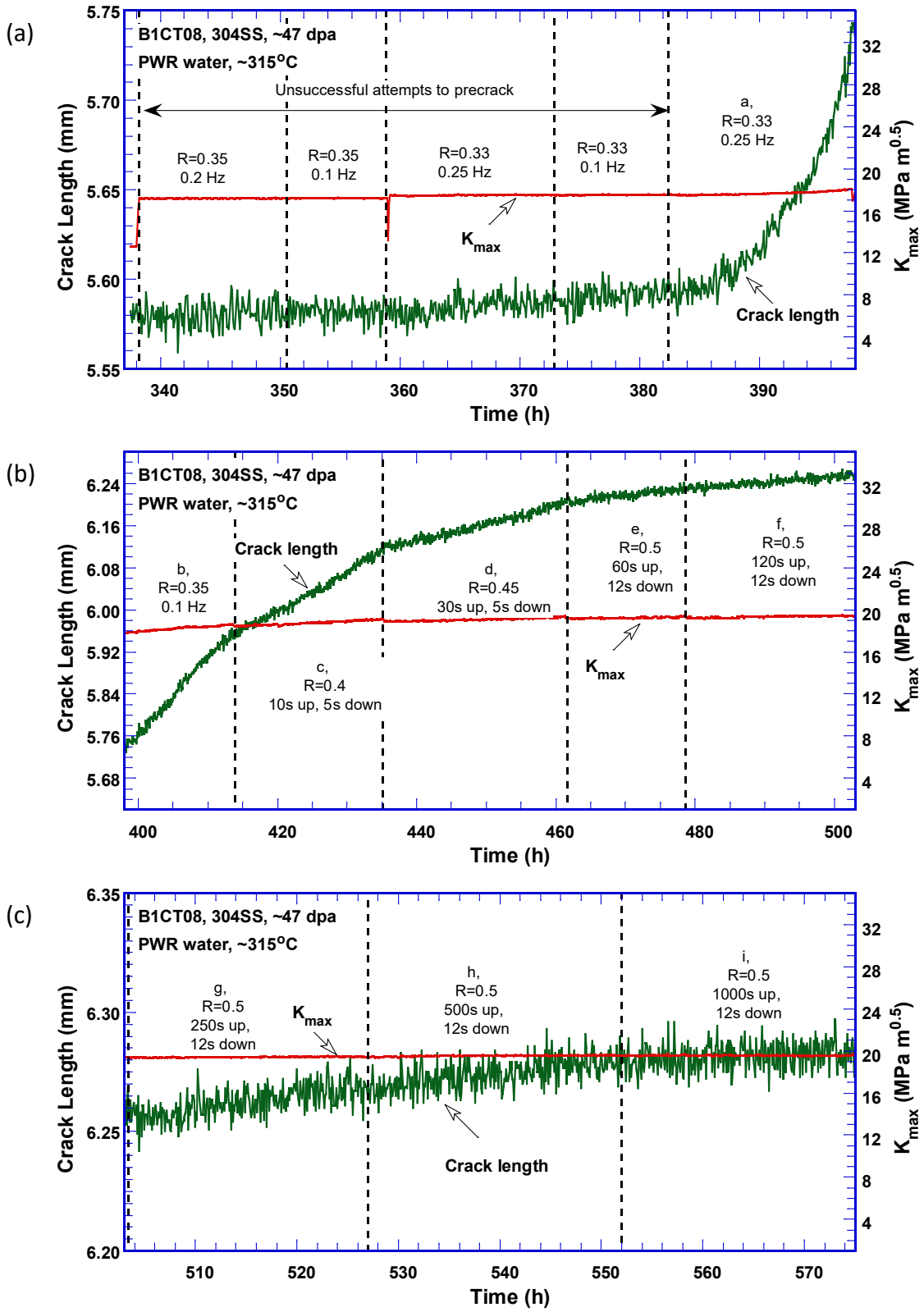

Figure 51. Crack-length-vs.-time plot of Specimen B1CT08 (~47 dpa) tested in PWR water: test periods (a) a, (b) b–f, (c) g–i, (d) 1–2, (e) j–m, (f) 3–4, and (g–k) details of test period 4

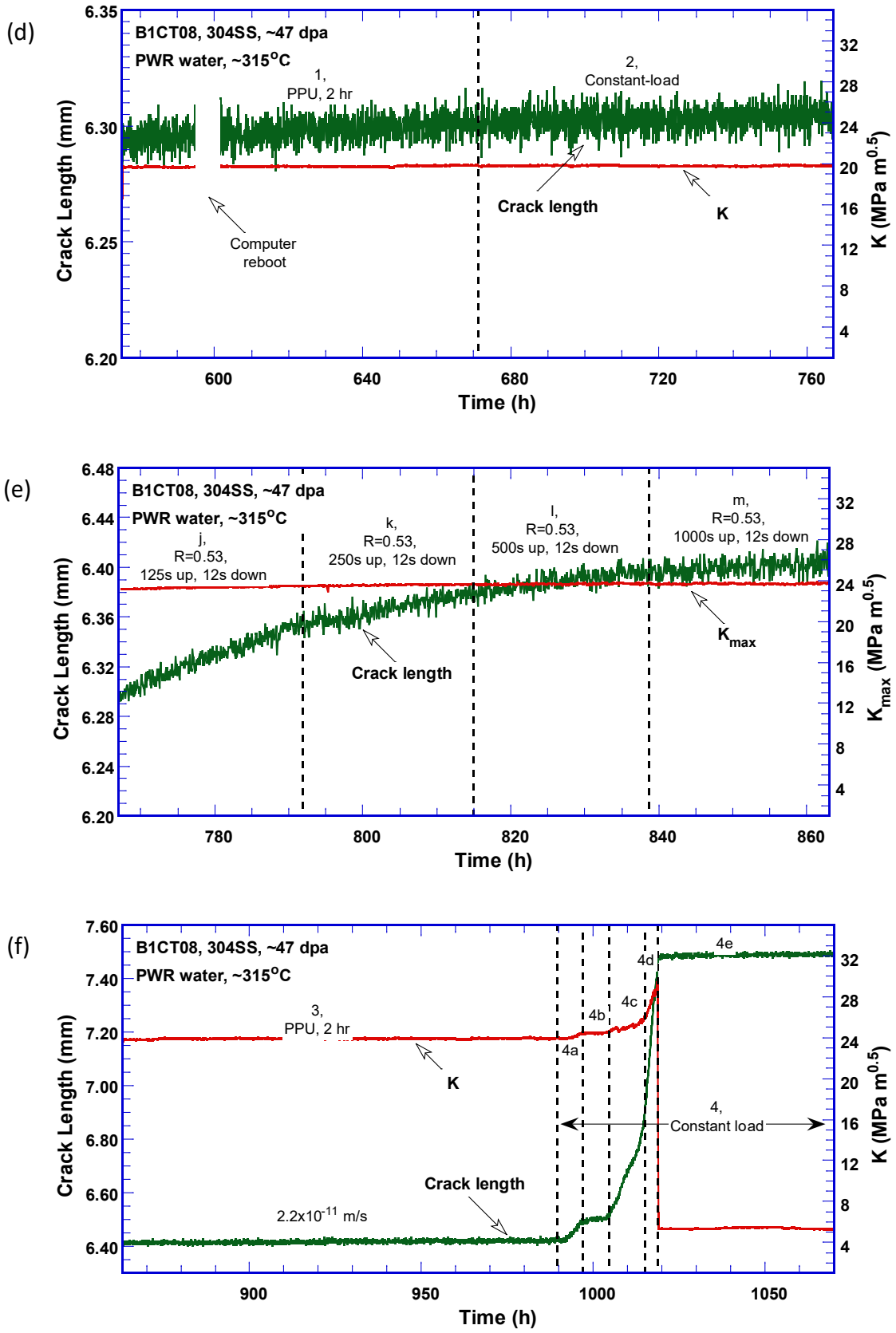

Figure 51. (Cont.)

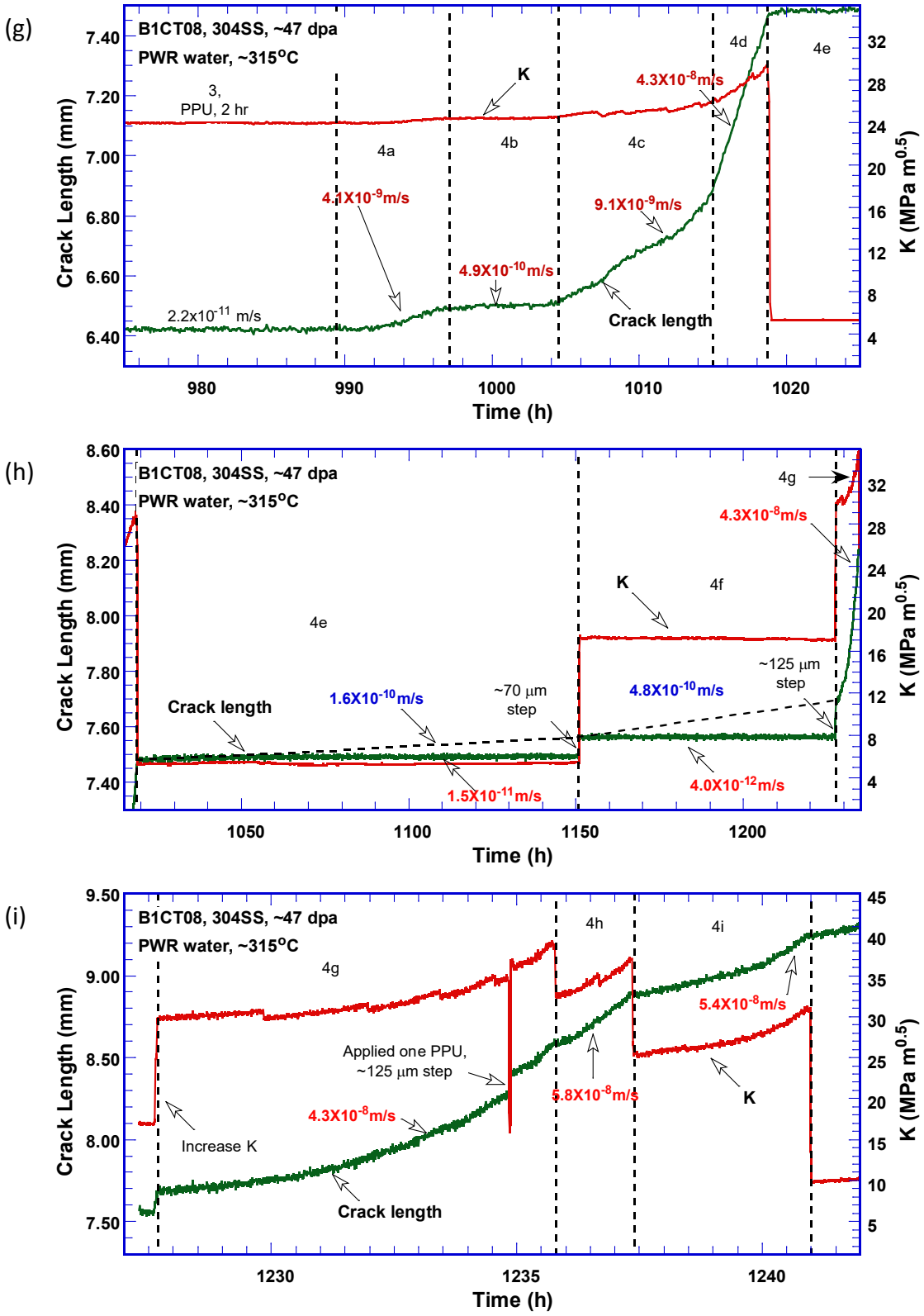

Figure 51. (Cont.)

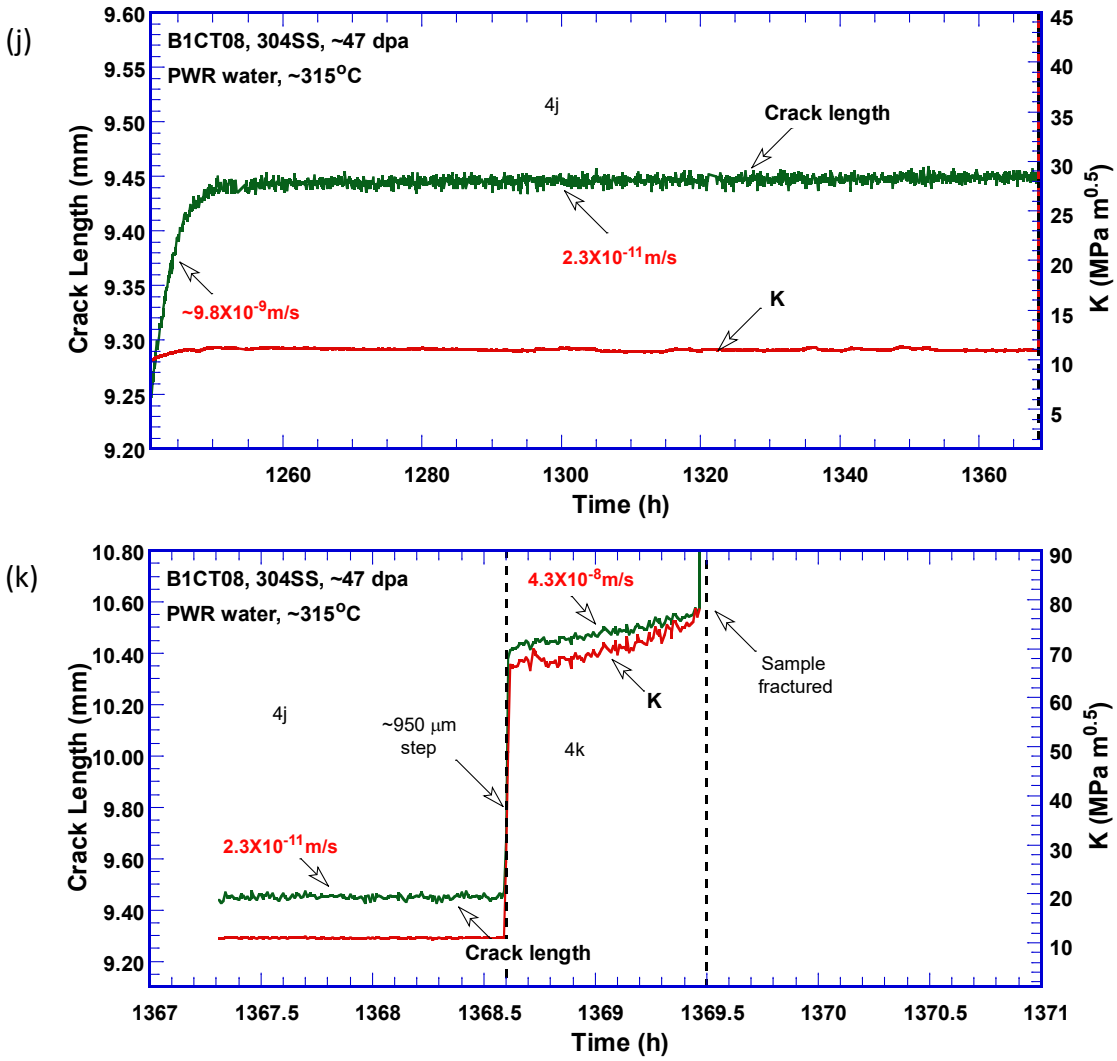

Figure 51. (Cont.)

The cyclic CGRs obtained from this sample are plotted against the anticipated fatigue growth rate in air in Figure 52. Note that the data points below the diagonal line representing the failed attempts to pre-crack the sample are omitted in the figure. The crack was difficult to initiate in this sample, and a much higher K_{max} had to be used at the beginning of the test. The degree of environmental enhancement was also not very high for this sample, compared with other lower-dose specimens. However, once the crack was initiated, the cyclic cracking behavior was stable and quite repeatable with similar ΔK values at two K_{max} levels (see Figure 52).

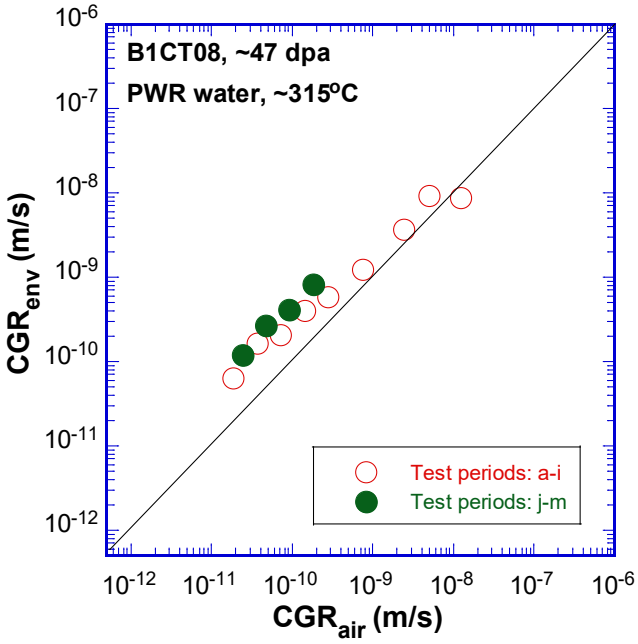

Figure 52. Cyclic CGRs of Specimen B1CT08 (~47 dpa) tested in PWR water

In contrast to a well-behaved cyclic cracking performance, the constant-K (or constant-load) SCC behavior of this sample is very different from all other specimens tested in this study. Figure 53 shows the SCC CGRs obtained from this sample along with the data from the first 47-dpa specimen (B1CT09). The NUREG-0313 curve is included in the figure as a reference. Before an unstable cracking behavior started in this sample, its SCC performance was nearly identical to that of the first 47-dpa sample (red data points in Figure 53). Rapid crack growth behavior started to appear during test segment *4a*, and only stopped when the applied K dropped substantially lower, to around 5.5 MPa $m^{1/2}$. Even at such a low K, the obtained stable CGRs are close to the NUREG-0313 curve, which indicates elevated cracking susceptibility. Any load increase, either by reloading the sample after a PPU or by increasing the applied K, will generate a huge jump in crack length, suggesting unstable cracking behavior. These jumps in crack length are so large that they are unlikely to be explained by a sudden rupture of previously unbroken ligaments developed during the test. As shown in Figure 53, the highest CGRs obtained on this sample are all around 4-6 × 10^{-8} m/s, much higher than the NUREG-0313 disposition curve. This high cracking susceptibility is unexpected for the low corrosion potential environment and seems to be related to unstable cracking behavior that can be triggered by load increases. Additional research is necessary to understand this cracking behavior and its relationship with irradiation damage and degradation.

4.6.2 Fracture Morphology

The fractured sample was removed from the autoclave and decontaminated remotely with manipulators. Several replicas were then cast from the fracture surface and examined with a SEM. Figure 54 shows the entire fracture surface of the sample; the crack advance direction is from bottom to top in the picture. Intergranular cracking is the dominant fracture morphology for this sample. The final crack size is much larger than that indicated by the DCPD measurement, confirming that the crack lengths and applied K values were significantly underestimated during the test. The final correction factor for this sample is 2.3, significantly higher than those of other specimens tested in this study.

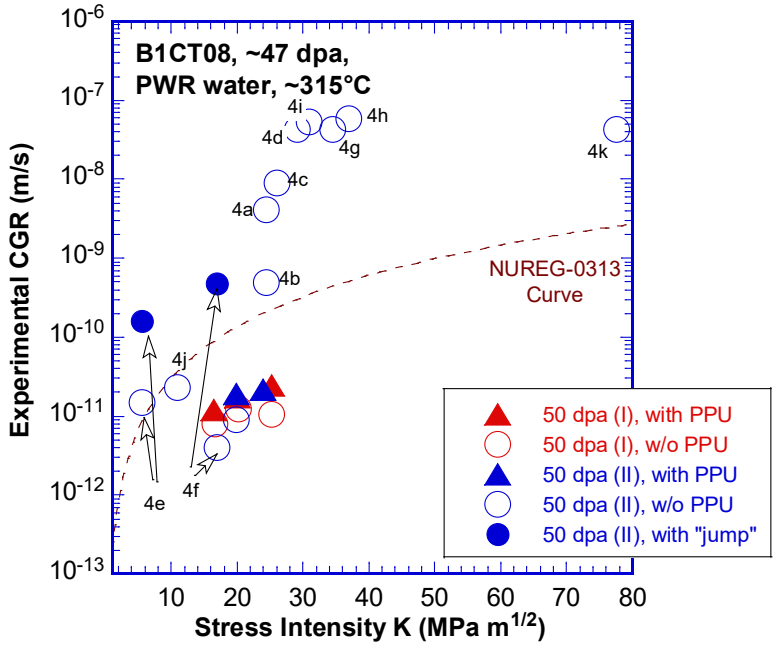

Figure 53. SCC CGRs of Specimen B1CT08 (~47 dpa) tested in PWR water

At the beginning of the CGR test, a small TG area can be seen, corresponding to the fatigue crack growth region. This TG area is not uniform across the entire crack front during the cyclic CGR test, suggesting a possible misalignment at the beginning of the test. This initial misalignment is believed to have no significant impact on the later test result since the final crack front was quite straight. The initial TG area also contains some crystallographic facets, as shown in Figure 55. As the crack propagates deeper, the fracture morphology become IG. Small patches of TG areas are still present, but the IG coverage has become very extensive, as shown in Figure 56. At the end of the CGR test, the sample failed unexpectedly because the applied K was severely underestimated during the test. The applied K at the failure was estimated to be ~78 MPa $m^{1/2}$. It is interesting to note that, despite the brittle IG morphology revealed during the CGR test, the final ligament of the sample was fractured in a ductile tearing mode as shown in Figure 57. This fracture morphology obtained at ~315°C is in sharp contrast to the IG morphology obtained at room temperature for other high-dose samples in this study.

Figure 58 shows the fracture surface along the sample centerline and corresponding crack length history plots at different test segments. Except some TG areas at low K levels, IG cracking covers the entire CGR test region. The very high CGRs (1-6 × 10^{-8} m/s) and big jumps in crack length were all obtained at relatively high K levels above ~25 MPa $m^{1/2}$.

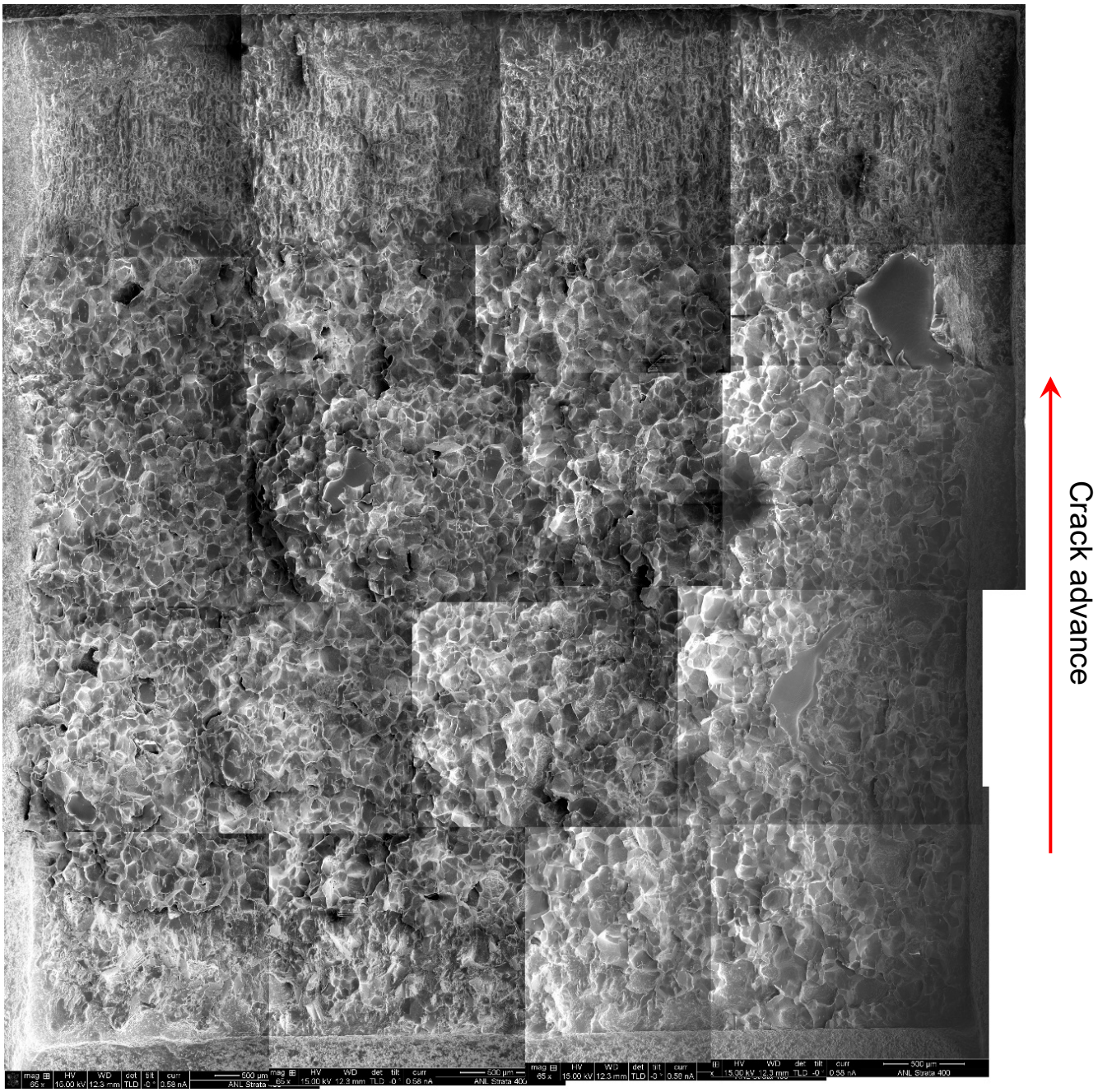

Figure 54. Fracture surface of B1CT08, a 47-dpa sample tested in simulated PWR water

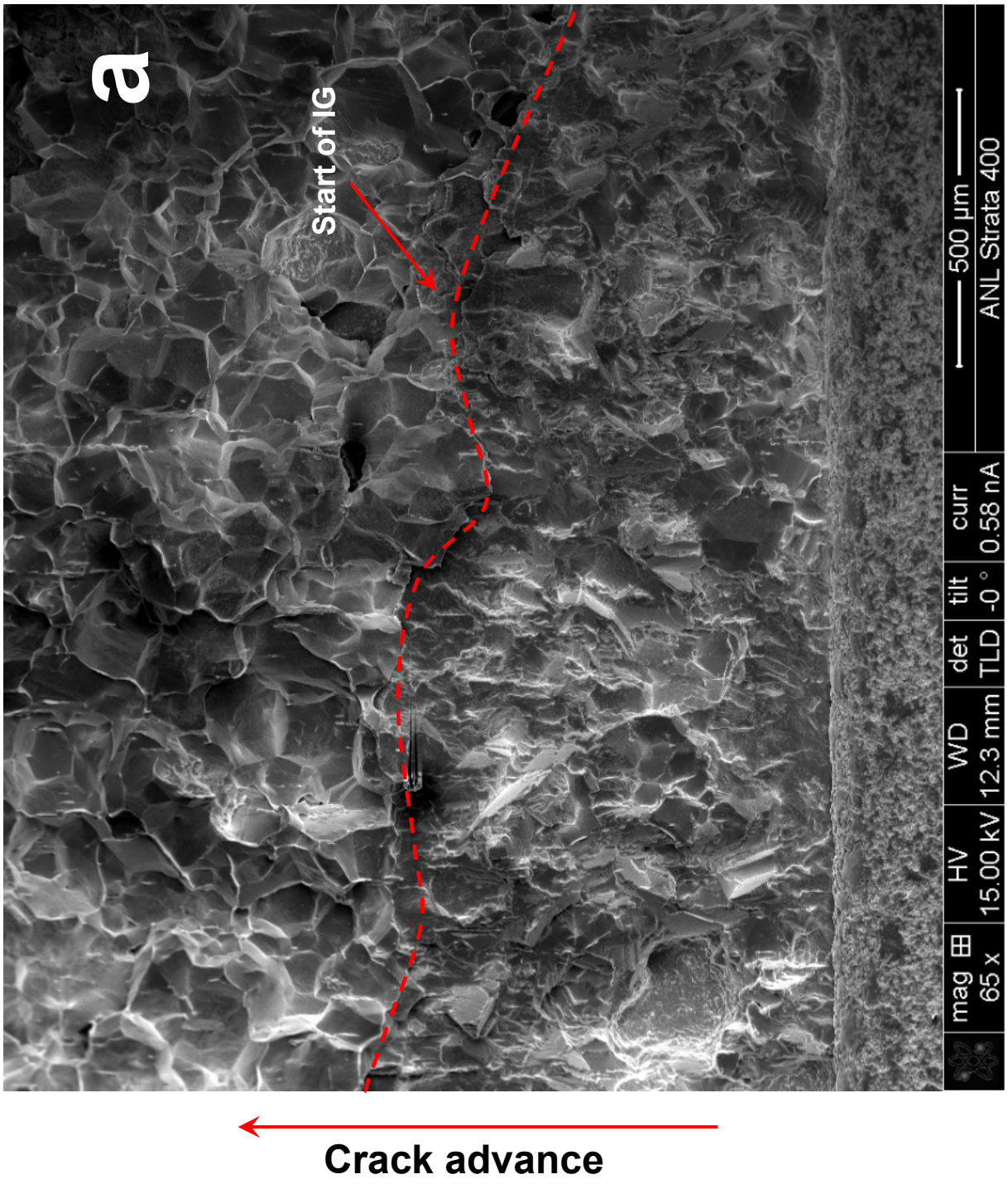

Figure 55. Enlarged views of the beginning of the CGR test for B1CT08, (a) and (b)

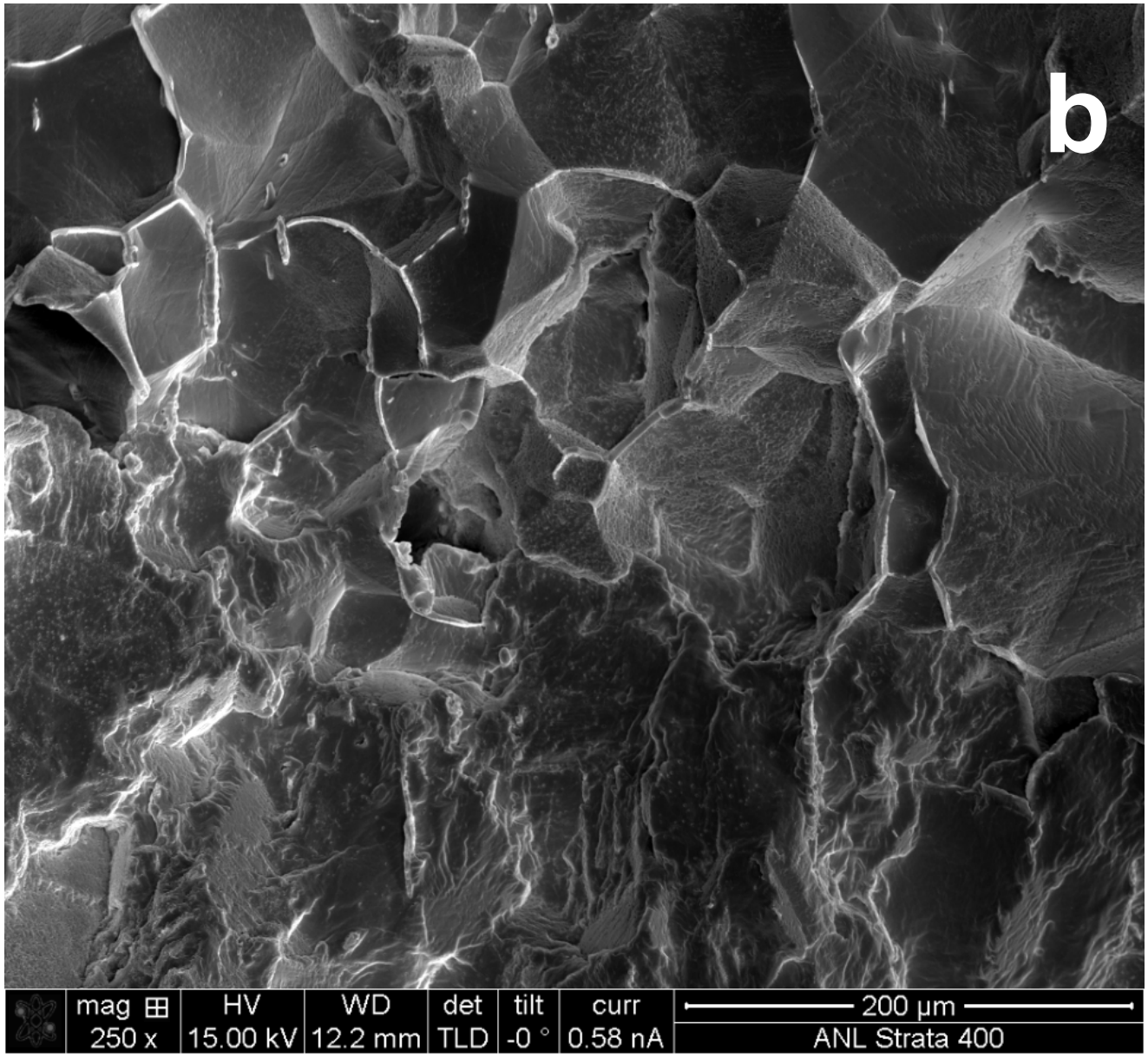

Figure 55. (Cont.)

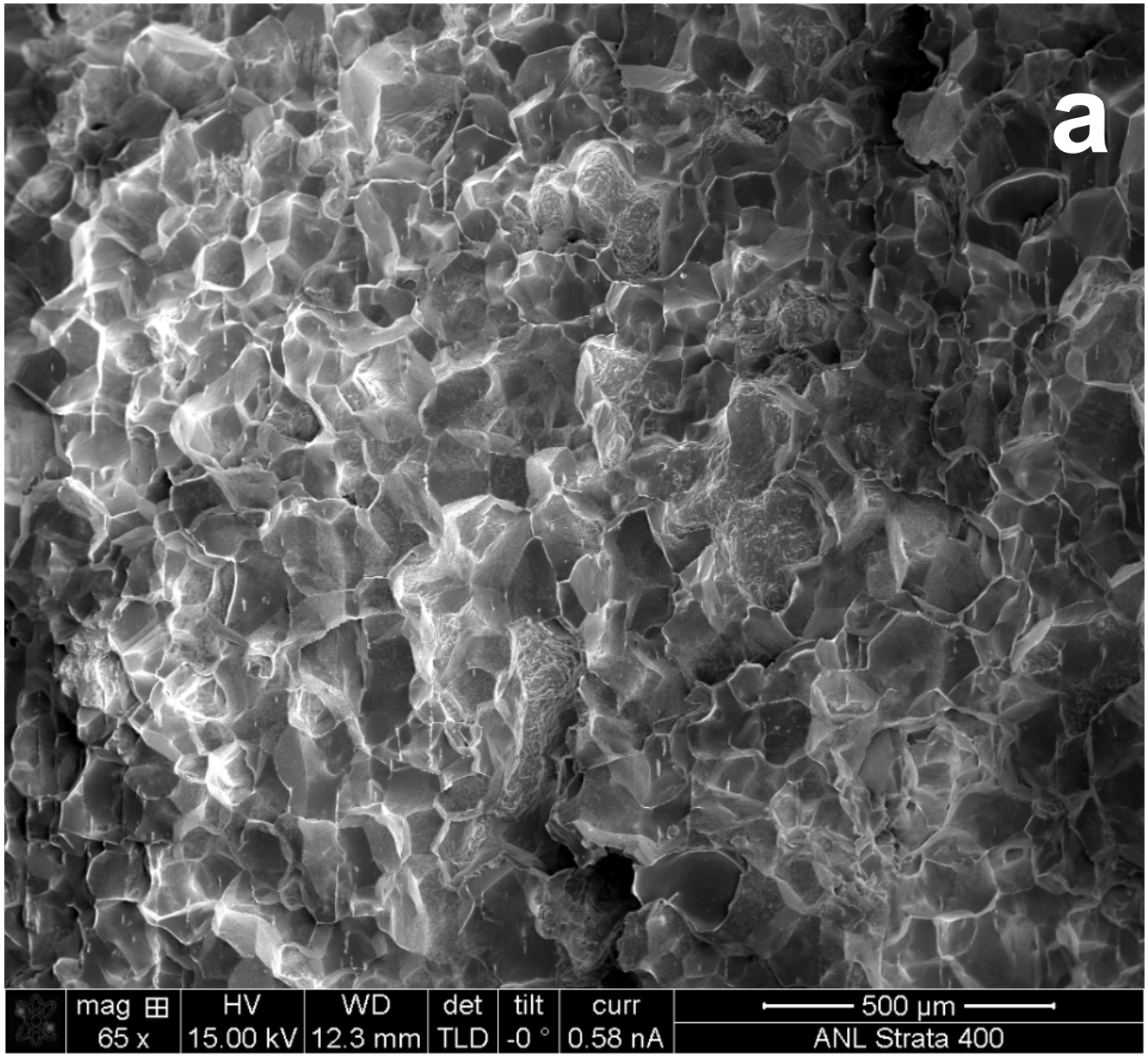

Figure 56. Enlarged views in the middle of the CGR test for B1CT08, (a) and (b)

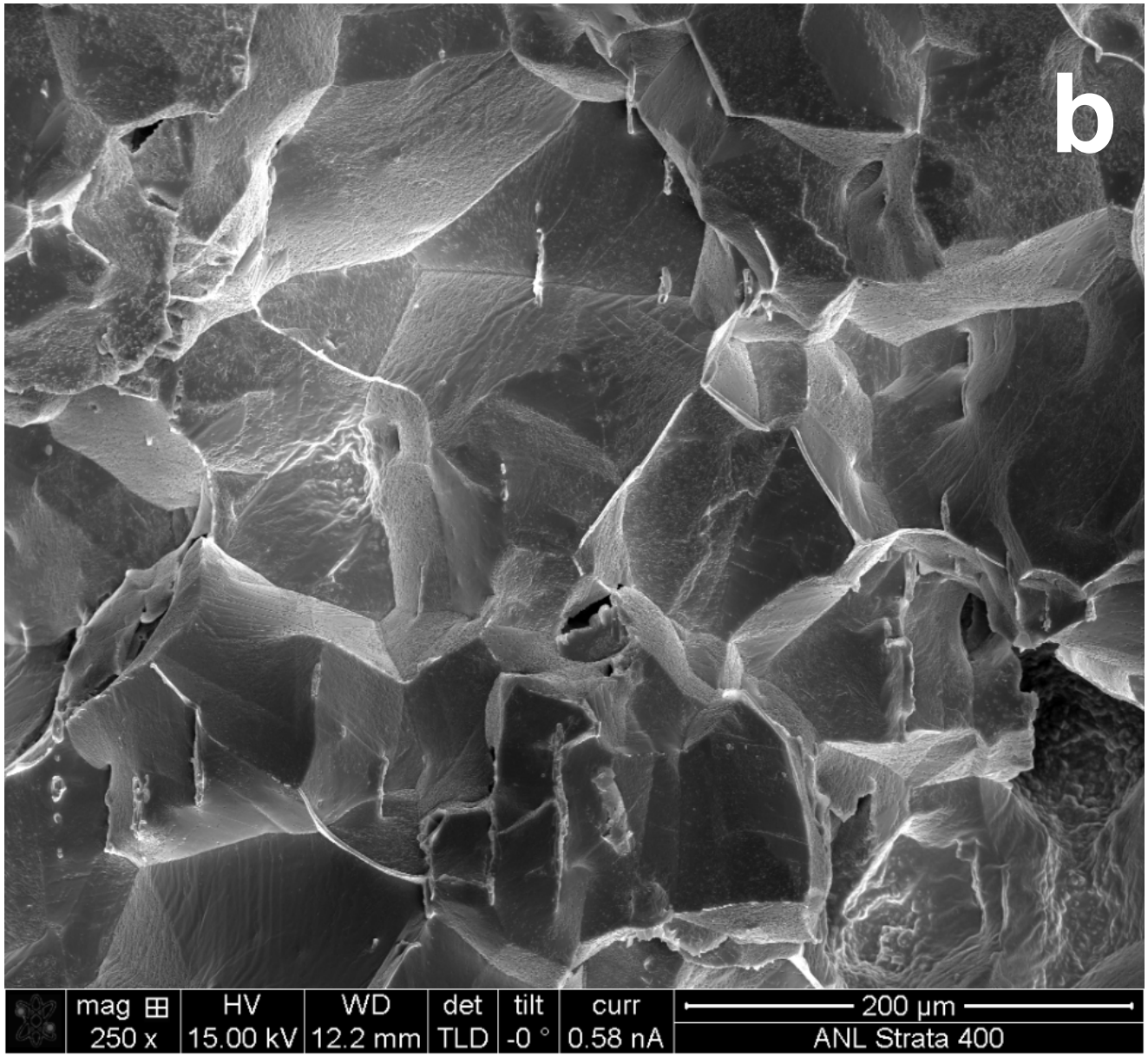

Figure 56. (Cont.)

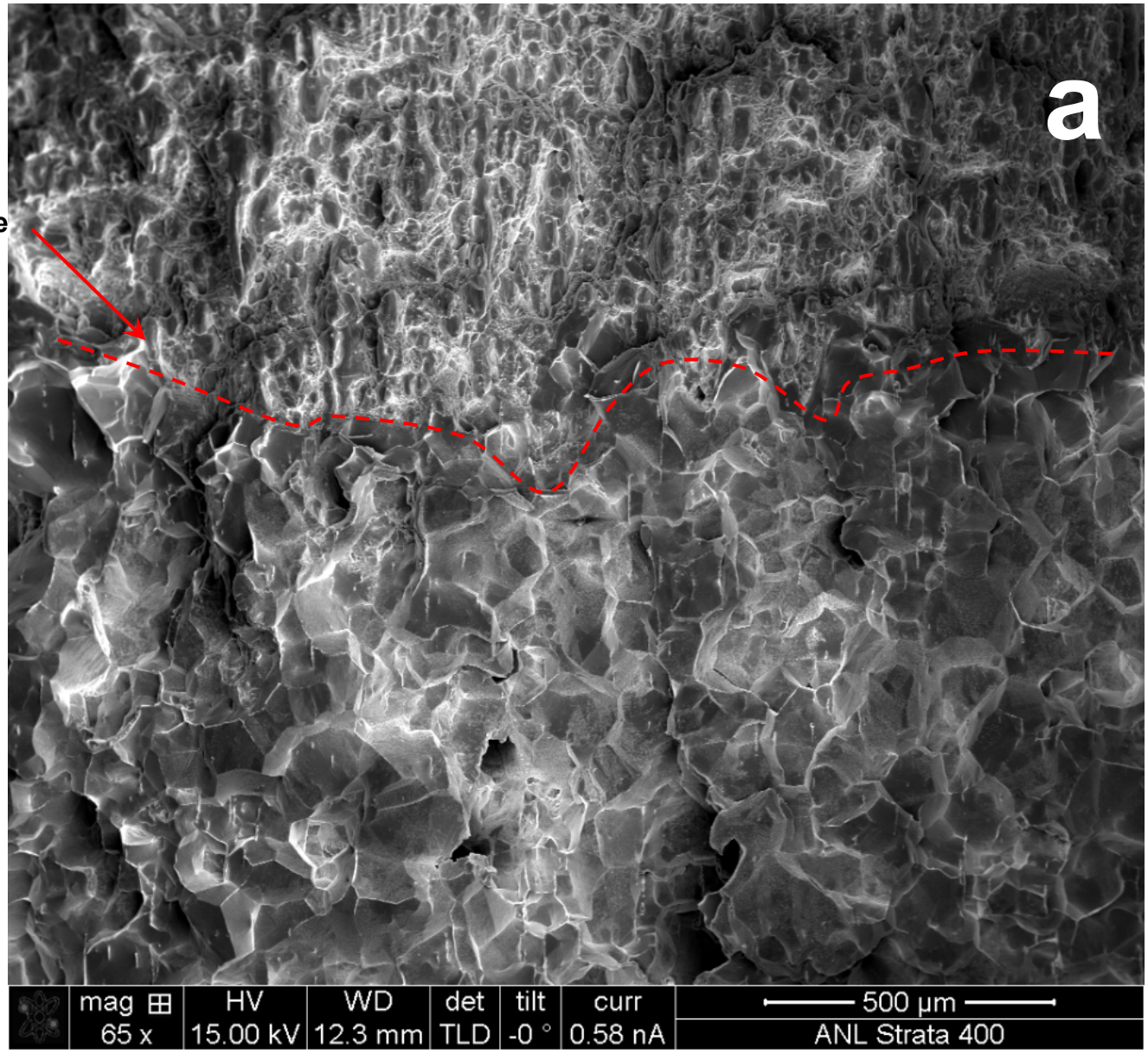

Figure 57. (a) Enlarged views at the end of the CGR test, and (b) the final tearing of the ligament for B1CT08. Crack advance direction is from bottom to top

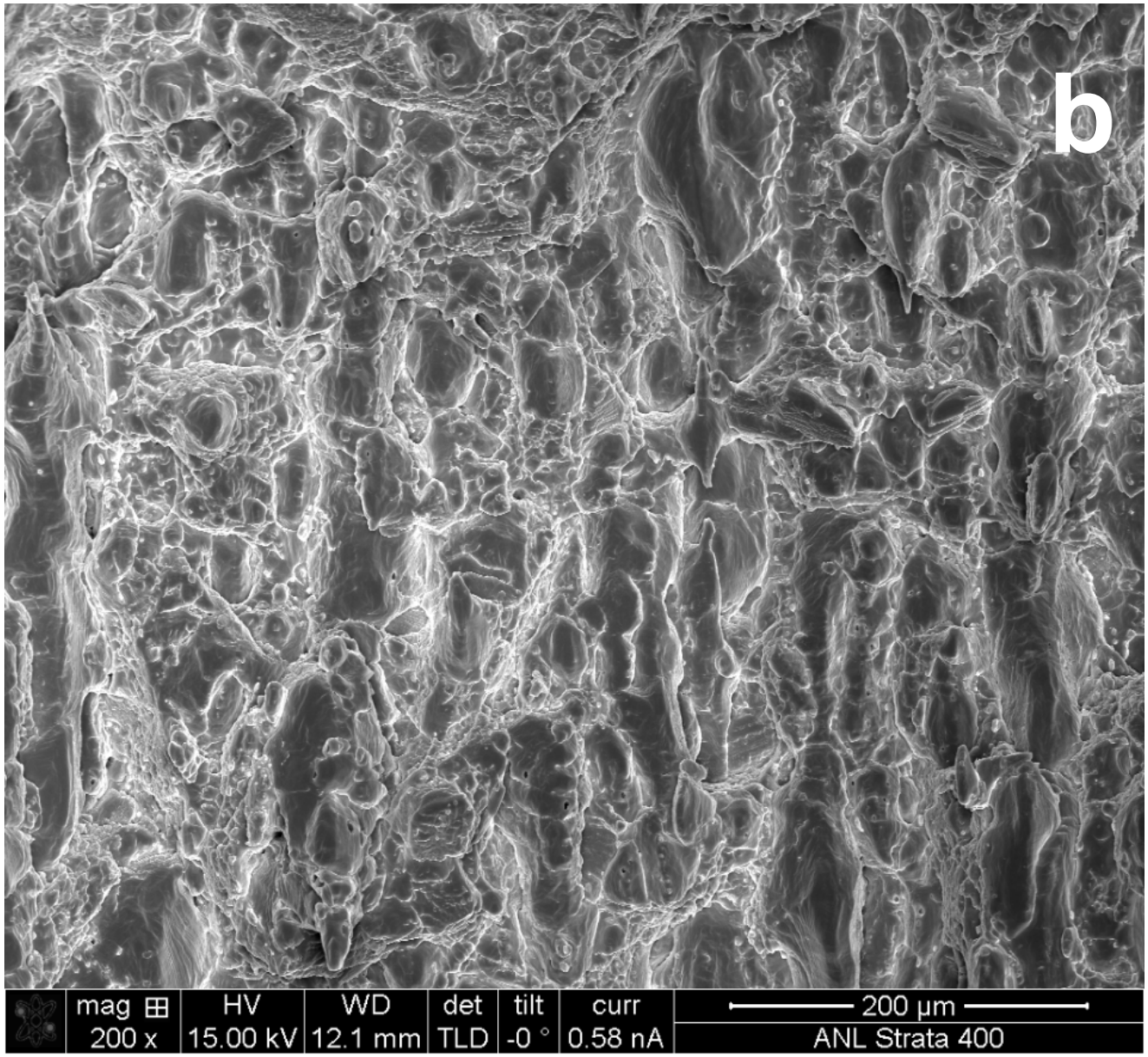

Figure 57. (Cont.)

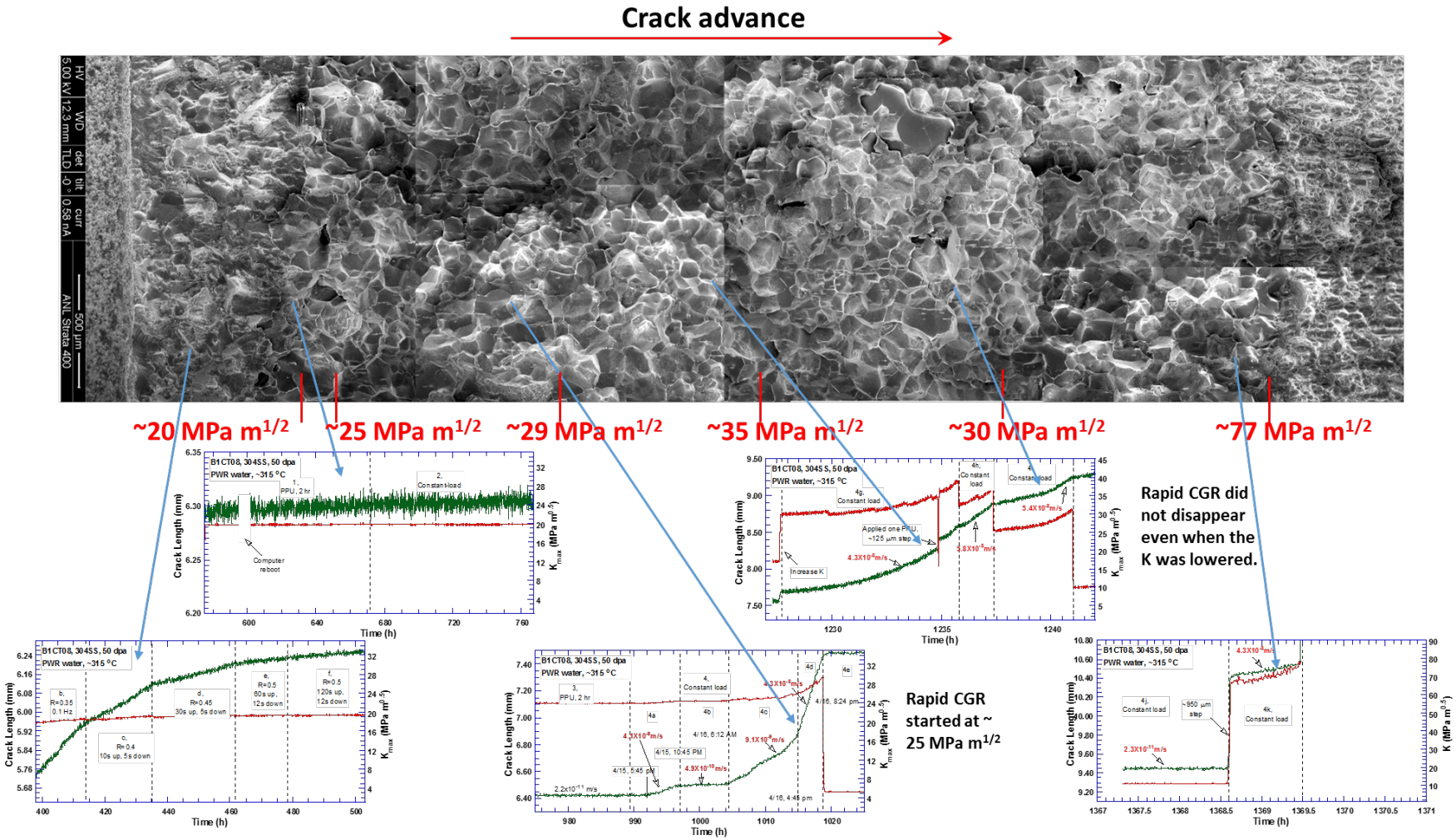

Figure 58. IG morphology and crack length history plots of Specimen B1CT08

5 DISCUSSION

Compact-tension specimens harvested from the decommissioned Zorita baffle plate materials were tested in this study to evaluate their SCC cracking susceptibility in low-corrosion-potential environments and fracture resistance at difference doses. The results of CGR and J-R curve tests are summarized in Table 9 and Table 10, respectively. For most of the specimens, near-constant K was maintained during their SCC tests by periodical load shedding. For the specimen exhibiting abnormally high CGRs (Specimen B1CT08), load shedding was insufficient, and thus the constant-K condition could not be maintained adequately. As a result, rising K was present in some test segments for Specimen B1CT08.

For the J-R curve tests, SCC cracks were used as starter cracks. The initial values of a/W were between 0.55 and0.57 for all samples. For each specimen, J-Δa data are fitted to a power-law correlation, and the resulting pre-factor (*C*) and power exponent (*n*) are reported in Table 10. The J values at the 0.2- and 2.5-mm crack extension are also given in the table. Note the $J_{2.5\text{-mm}}$ value is obtained by extrapolating the J-R curve to intercept with the 2.5-mm offset line.

Table 9. The SCC CGR test results for the decommissioned Zorita baffle plate materials

Sample ID.	**Dose (dpa)**	**Test Env.**	**SCC CGR**		
			K (MPa $m^{1/2}$) [a]	**CGR with PPU** ($\times10^{-11}$ m/s)	**CGR w/o PPU** ($\times10^{-11}$ m/s)
A3CT04	~0.06	PWR	15.5	0.99	-
			15.6	-	0.05
			21.5	1.51	-
			21.6	-	0.38
			27.5	1.77	-
			27.5	-	0.20
B3CT14	~8	Low-DO, high-purity	16.9	2.43	-
			17.2	-	1.47
			21.2	2.86	-
			21.2	-	1.78
			27.0	1.71	-
			27.0	-	1.27
ACT03	~15	Low-DO, high-purity	16.4	1.00	-
			16.4	-	0.96
			20.7	1.35	-
			20.7	-	0.59
			26.5	3.74	-
			26.9	-	2.25
B1CT07	~39	Low-DO, high-purity	16.7	3.03	-
			17.1	-	1.84
			21.3	3.01	-
			21.1	-	1.82
			26.0	3.94	-
			26.2	-	1.47
B1CT09	~47	Low-DO, high-purity	16.4	1.20	-
			16.6	-	0.80
			20.1	1.75	-
			20.2	-	1.24
			25.2	2.46	-
			25.3	-	1.04

Table 9. (Cont.)

Sample ID.	Dose (dpa)	Test Env.	SCC CGR		
			K (MPa $m^{1/2}$) [a]	**CGR with PPU** ($\times 10^{-11}$ m/s)	**CGR w/o PPU** ($\times 10^{-11}$ m/s)
B1CT08	~47	PWR	19.8	1.88	-
			19.8	-	0.90
			23.9	2.19	-
			24.4	-	409
			24.5	-	49.2
			24.3–26.0	-	906
			26.0–29.2	-	4290
			5.5	-	1.50
			17.0	-	0.40
			30.0–39.0	-	4280
			32.7–37.0	-	5780
			25.3–30.9	-	5350
			10.9	-	2.33
			66.5–77.6	-	4340

[a] When a rising K condition is present, a K range is provided.

Table 10. The J-R curve test results of decommissioned Zorita baffle plate materials

Sample ID	Dose (dpa)	$J = C \times \Delta a^n$		$J_{0.2\text{-mm}}$ (kJ/m^2)	$J_{2.5\text{- mm}}$ [a] (kJ/m^2)
		C	n		
A3CT04	~0.06	220	0.61	100	412
B3CT14	~8	113	0.07	103	120
ACT03	~15	92	0.13	77	104
B1CT07	~39	80	0.12	71	94
B1CT09	~47	80	0.04	75	83

[a] Calculated values by extrapolating the J-R curves to 2.5 mm.

5.1 Cyclic Crack Growth Rates

In this study, all samples were pre-cracked *in situ* in the autoclaves. Figure 59 shows the measured cyclic CGRs in the test environments as a function of the anticipated fatigue growth rate in air under the same loading conditions. The fatigue growth rates were calculated based on the Paris law relationship specified in Section XI of the ASME design code for unirradiated SSs [15]. For each specimen, the cyclic CGR test starts from the upper right corner of the CGR_{env}-versus-CGR_{air} plot and progresses toward the lower left corner as the rise time and load ratio increase. At the beginning of the test, the measured CGRs scattered around the CGR_{air} line, suggesting that mechanical fatigue plays a dominant role in the overall response of crack growth. Environmentally enhanced cracking only became evident when the fatigue growth rate fell below ~10^{-10} m/s among these samples.

A corrosion-fatigue curve previously developed at ANL for unirradiated SSs is included in Figure 59. By assuming that the environmental contribution to cyclic CGRs is correlated with fatigue growth rate in air by $CGR_{cf} \propto CGR_{air}^{0.5}$, Shack and Kassner [17] determined the corrosion-fatigue curve shown in Figure 59 bounds a large group of wrought and cast SSs tested in high-purity water with less than 0.2 ppm DO. As shown in the figure, most of the data points are also bounded by this low-DO curve, especially at the low CGR region, which suggests good

resistance to corrosion fatigue for this decommissioned Zorita material. No elevated environmental enhancement was seen among these samples up to ~47 dpa in their test environments.

Although all samples behaved similarly in the cyclic tests, the environmentally enhanced cracking appeared more readily in the 0.06-dpa specimen than in the other high-dose samples (i.e., dose > 8 dpa). As shown in Figure 59, many data points from the high-dose samples (all open symbols) fell below the CGR_{air} line, but the 0.06-dpa data (solid red triangles) were consistently above the CGR_{air} line. The reason that the enhancement is more evident in the 0.06-dpa sample is perhaps due to the different sizes of plastic zones in the high- and low-dose samples. The yield strengths increase rapidly in SSs with irradiation dose below ~5 dpa, but trend to saturate above ~10 dpa [13]. Consequently, the flow stress can be more than a factor of 2 lower for the 0.06-dpa sample than the rest of high-dose samples. Because most of the samples were pre-cracked with a similar K_{max} level between 15 and 16 MPa $m^{1/2}$, a larger plastic zone must have been present in the 0.06-dpa sample than in those of high-dose specimens. This may have facilitated the cracking and thereafter environmental enhancement in the 0.06-dpa sample.

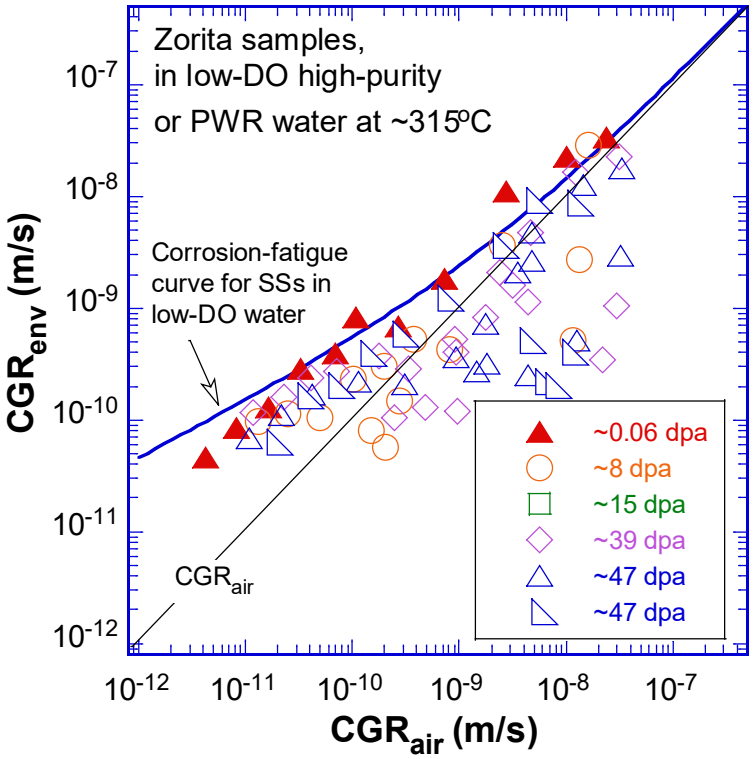

Figure 59. Cyclic CGRs measured in the test periods before the SCC CGR tests

The level of environmental enhancement continued to evolve during the cyclic test. Using the ratio of CGR_{env}/CGR_{air} as a measure, the degree of environmental enhancement can be evaluated. As shown in Figure 60, the enhancement factor of the 0.06-dpa sample is just slightly higher than those of samples at higher doses. If we normalize the enhancement factor with the applied ΔK, which is the basic driving force for cyclic crack growth, the 0.06-dpa sample really stands out. At a given ΔK, the environmental enhancement can be much stronger for the 0.06-

dpa specimens than for the rest of high-dose samples. This suggests that irradiation did not affect the corrosion-fatigue behavior of the decommissioned Zorita materials in the test environments.

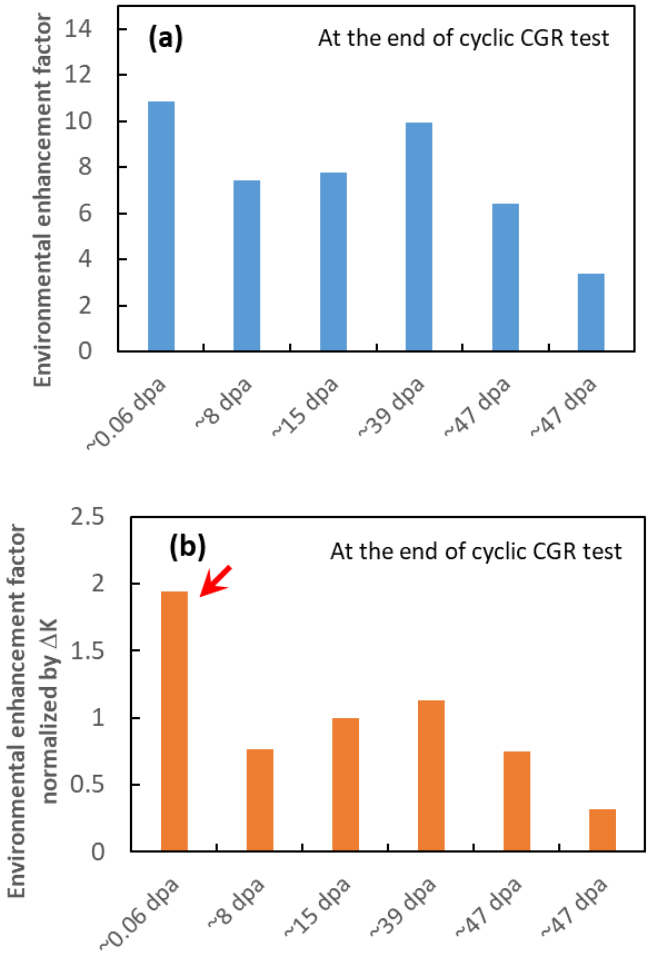

Figure 60. Environmentally enhanced cracking at the end of cyclic CGR test, (a) enhancement factor, (b) enhancement factor normalized by ΔK

Figure 61 shows the fracture surfaces of the cyclic CGR test regions of the tested samples. To reduce radiation exposure, replicas of the sample surfaces were used in the SEM examination. As shown in the figures, the dominant fracture mode of the cyclic CGR test regions is TG for all specimens. Some brittle facets can be seen on the fracture surfaces and are more pronounced in the high-dose samples. Despite a more faceted appearance, the cyclic CGRs of the high-dose samples are not very different from those of the 0.06-dpa specimen, suggesting a less important role of irradiation hardening for the corrosion-fatigue response in the low-corrosion-potential environments.

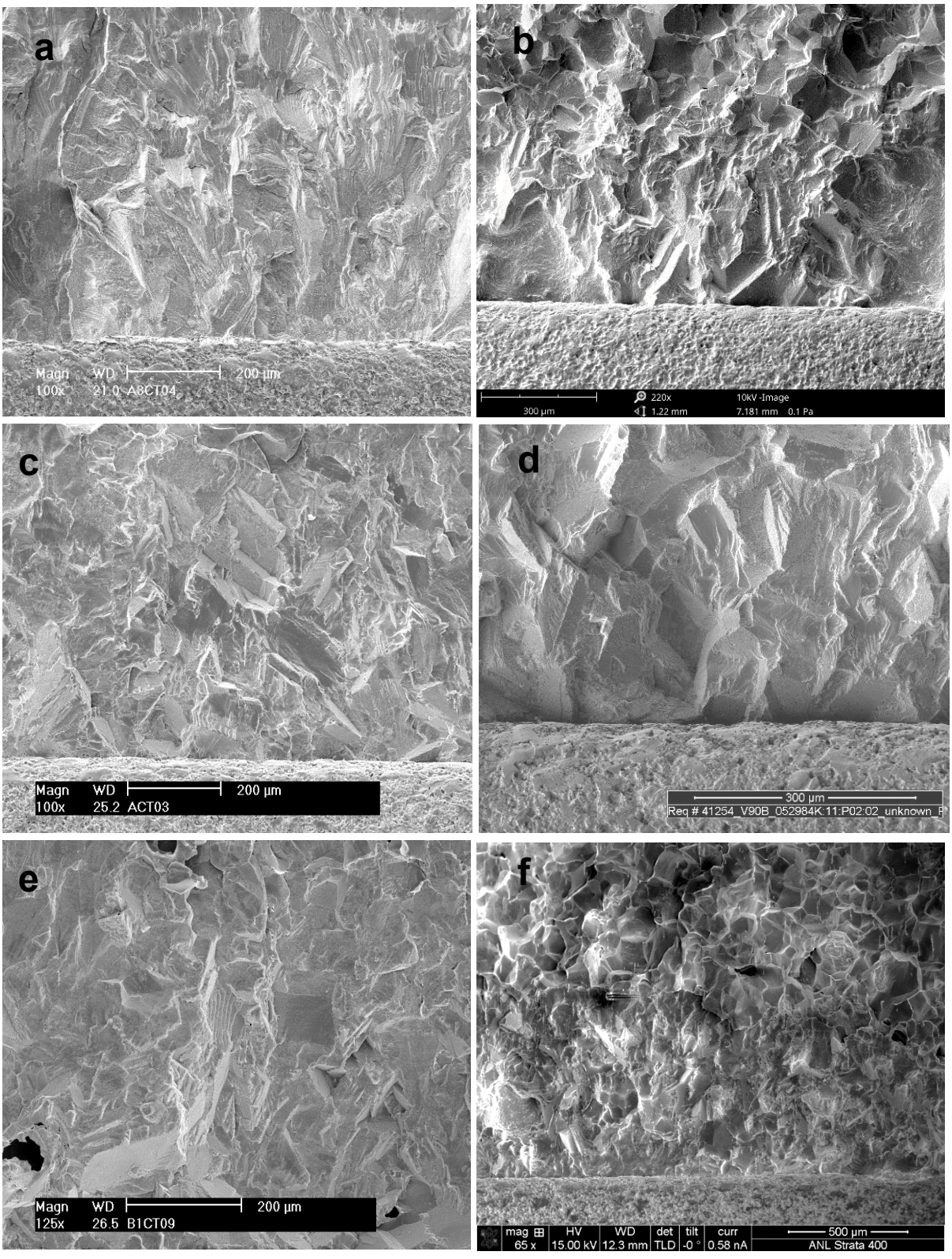

Figure 61. Fracture surfaces of the cyclic CGR test regions of the specimens, (a) ~0.06 dpa, (b) ~8 dpa, (c) ~15 dpa, (d) ~39 dpa, and (e–f) ~47 dpa. (crack advanced from bottom to top in all pictures)

5.2 SCC Crack Growth Rates

For each specimen, SCC CGRs were measured with and without PPU at three increasingly higher K levels above ~16 MPa $m^{1/2}$. Most of the samples in this study behaved normally, and no elevated cracking susceptibility was observed in the test environments. However, signs of cracking instability did exist in some of the samples. Several jumps in crack length were observed in some samples upon reloading or load increase. One of the 47-dpa samples also exhibited abnormally high CGRs during the test. Due to this drastically different cracking behavior, the SCC CGR results with and without the unstable cracking behavior are discussed separately.

Figure 62 shows the SCC CGRs as a function of applied K, excluding those data points associated with the unstable cracking. The filled and open symbols represent the test periods with and without PPU, respectively. In addition to the NUREG-0313 disposition curve, a more recent model [18] developed with irradiated data for PWR primary water is also included in the figure. This model is valid for 325°C and 800 MPa, a saturated yield strength above ~10 dpa [19]. As shown in Figure 62, no elevated SCC cracking susceptibility can be seen among these data points, and all SCC CGRs are well below the NUREG-0313 curve. Most of the test periods conducted with PPU show slightly higher growth rates than those without PPU. With PPU, the recorded CGR ranges from 1 to 4 × 10^{-11} m/s between 15 and 28 MPa $m^{1/2}$, and no clear dose dependency can be seen among these samples. Without PPU, the scatter of the CGRs is wider, and the CGR values are generally a factor of 1.5 to 8 lower than those with PPU. Note that, limited by the test time, some CGRs without PPU were too low (<10^{-12} m/s) to be determined confidently in this study.

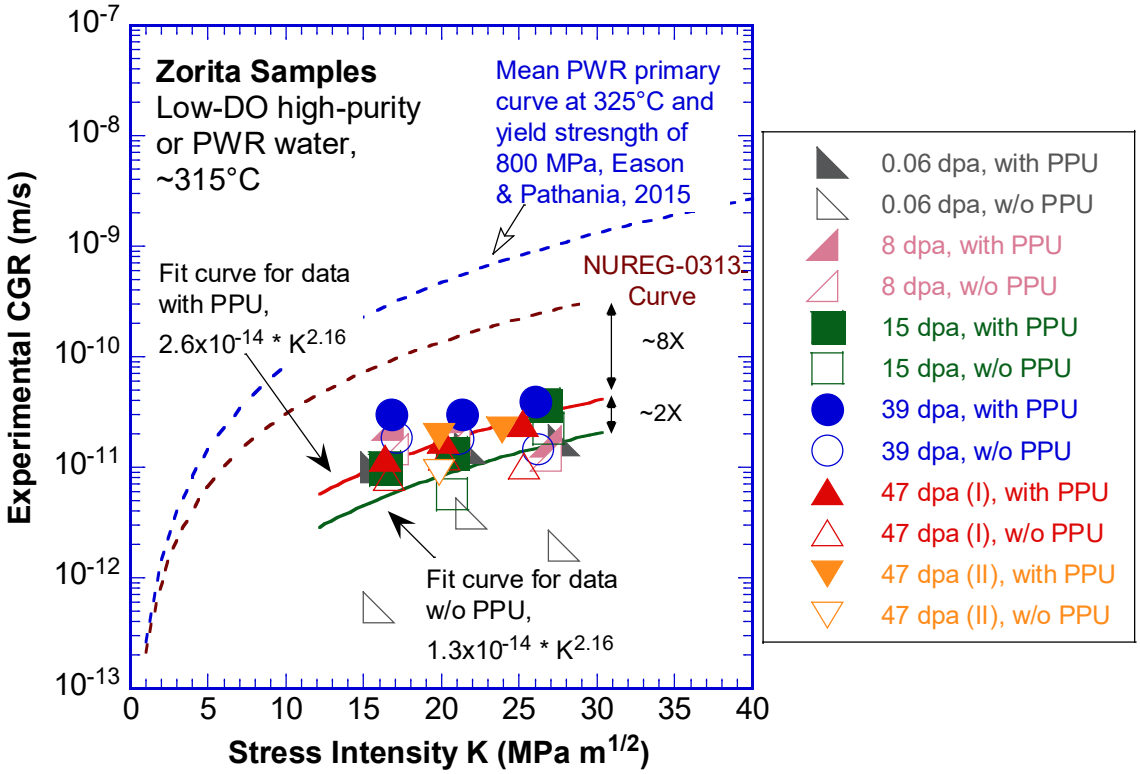

Figure 62. SCC CGRs without abnormal cracking behavior from the decommissioned Zorita baffle plate material

Without a clear dose dependence, all the CGR data in Figure 62 are grouped in two datasets, with and without PPU. A power-law correlation assumed for the NUREG-0313 curve [16] are used to fit the datasets. The fitting curve developed with the PPU dataset is at least a factor of 8 lower than the NUREG-0313 line. Without PPU, the correlation is reduced by another factor of 2. This rather good SCC resistance, even at ~47 dpa, is perhaps due to the beneficial effect of low-corrosion-potential environments. Both test environments are known to reduce the sensitivity of SSs to SCC substantially [14].

Despite this apparent good SCC performance, some peculiar cracking behaviors were noticed among these decommissioned Zorita materials. Figure 63 shows all data points obtained from this decommissioned Zorita material, including those of unstable cracking. Note that the upper limits of both horizontal and vertical axes are much higher than those in Figure 62. The “normal” SCC CGR data points cluster around the lower-left corner of the figure, below the NURGE-0313 curve. Some very high CGRs are observed, and most of them are from the second 47-dpa specimen (B1CT08). Note that such high K levels are not the intended test condition, but rather a result of the underestimation of crack length during the test.

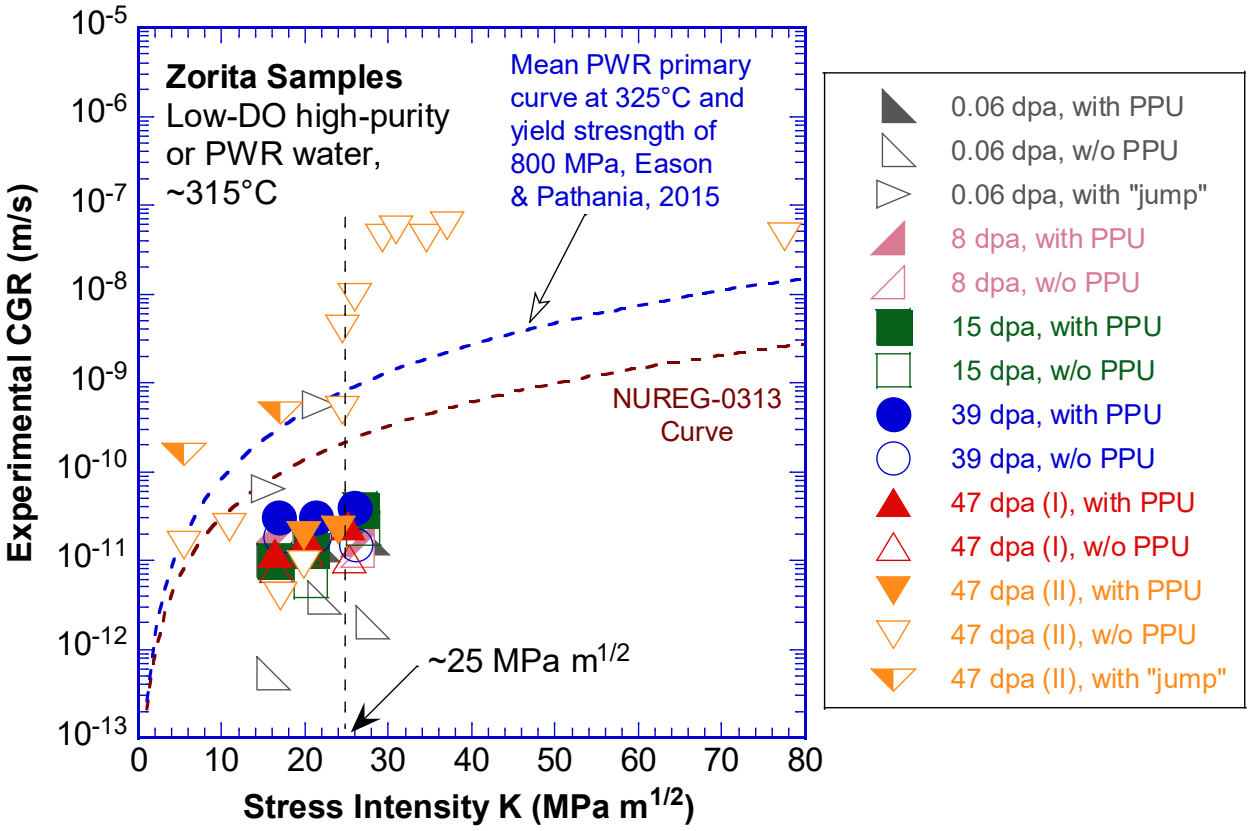

Figure 63. All SCC CGRs obtained from the decommissioned Zorita material

The high growth behavior in the second 47-dpa sample (B1CT08) did not occur at the very beginning of the test. In fact, the cyclic CGR test and the SCC CGR measurement at the first K level were normal in the first part of the test. As shown in Figure 63, the CGRs measured in the two test periods with PPU (solid orange upside-down triangles) are very similar to those of the first 47-dpa sample (solid red triangles). The high growth behavior was “activated” during the

SCC test without a clear trigger. The measured CGR climbed steadily from 2.2×10^{-11} m/s to 4.1×10^{-9} m/s within ~8 hours. There was an unintended rising K condition during this time because of the rapid crack growth. As a result, there could be a positive dK/da feedback to the crack growth behavior as shown by Andresen and Morra [21]. However, the magnitude of the dK/da in this case (~6 MPa $m^{1/2}$/mm) seems too low to affect the plastic strain rate at the crack front dramatically. Therefore, the observed rapid crack growth behavior is unlikely to have been caused by a positive dK/da effect.

The very high CGRs were all obtained above ~25 MPa $m^{1/2}$, as shown in Figure 63. Regardless of the applied K, the measured CGR seems always to approach to 4–6 × 10^{-8} m/s eventually. No K dependence can be seen among the high CGRs. In addition, this rapid growth behavior seems persistent once activated. Even when the applied K was lowered to ~5.5 and 11 MPa $m^{1/2}$, stable CGRs on the order of 10^{-11} m/s could be maintained in this 47-dpa sample. These CGRs were similar to those data points obtained at ~20 MPa $m^{1/2}$ before the abnormal cracking behavior started.

In addition to the high growth rate behavior, cracking instability was also observed in the 0.06- and 47-dpa specimens. Upon load increase or reloading, a stepwise increase in crack length was occasionally seen in the samples. These jumps in crack length can be seen in the time-history of Figure 4 and Figure 51. Four examples of these jumps are shown in Figure 64. For the 0.06-dpa sample, when K was increased from one level to another, a jump in crack length was observed during the first cycle of loading. This unstable, stepwise crack advance was similar to our previous observation on a 5-dpa cold-worked Type 316 SS sample, where stepwise growth behavior was observed in the test periods with PPU [20]. In this 0.06-dpa sample, however, the unstable crack jumps seemed unsustainable, and did not occur repeatedly during the unloading/reloading cycles of PPU. After these jumps, the observed CGRs declined rapidly under cyclic loading, suggesting the observed instability was associated with the loading events and did not contribute to stable crack growth. Regardless, if we count these abrupt crack jumps toward SCC crack growth, the measured CGRs would be dominated by the magnitudes of these jumps (as shown in Figure 63), and any measurement before the jumps would be meaningless.

For the 47-dpa sample, cracking instability was only observed after the high growth behavior was activated. The magnitudes of these jumps were also much larger compared to those in the 0.06-dpa sample, perhaps due to the higher K levels. However, a high growth rate can be sustained after a large jump in crack length, as shown in Figure 64d. This is different from that observed in the 0.06-dpa sample, suggesting a dose-dependent behavior. Nonetheless, the concurrence of these two phenomena suggests a common microstructural origin between the cracking instability and high growth rate. A high CGR behavior can only be sustained in the high-dose sample but not in the slightly irradiated specimen.

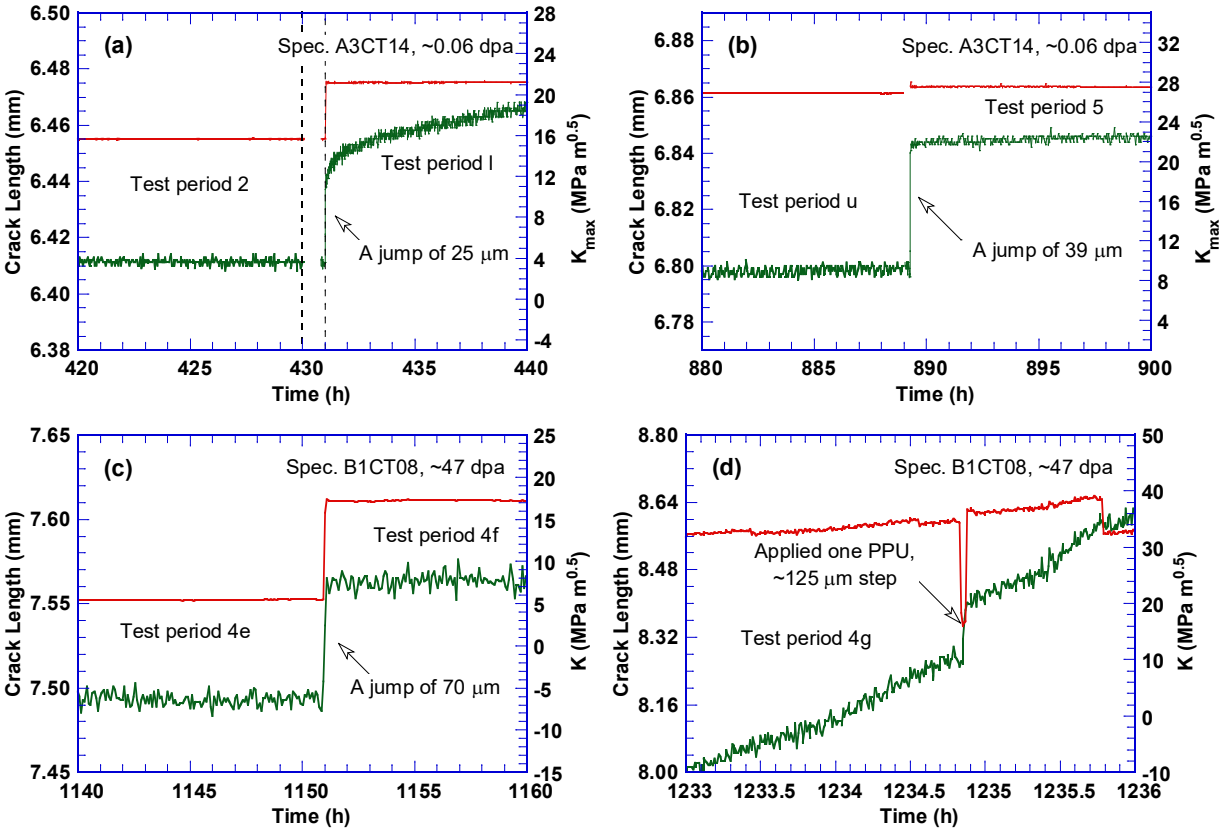

Figure 64. Jumps in crack length upon a load increase or re-loading, (a, b) Specimen A3CT14, ~0.06 dpa, and (c, d) Specimen B1CT08

The fracture morphologies of SCC test regions are shown in Figure 65. The crack propagation directions are from bottom to top in the pictures. A clear distinction can be seen between the 0.06-dpa sample and the rest of the samples at higher doses. The 0.06-dpa sample has a TG morphology, while all the other samples show a predominantly IG fracture. This change in fracture morphology with increasing dose suggests that a dose threshold may be necessary to activate an IG fracture mode in these samples. Damage mechanisms related to grain boundaries may dominate the IASCC response of the irradiated materials at high doses.

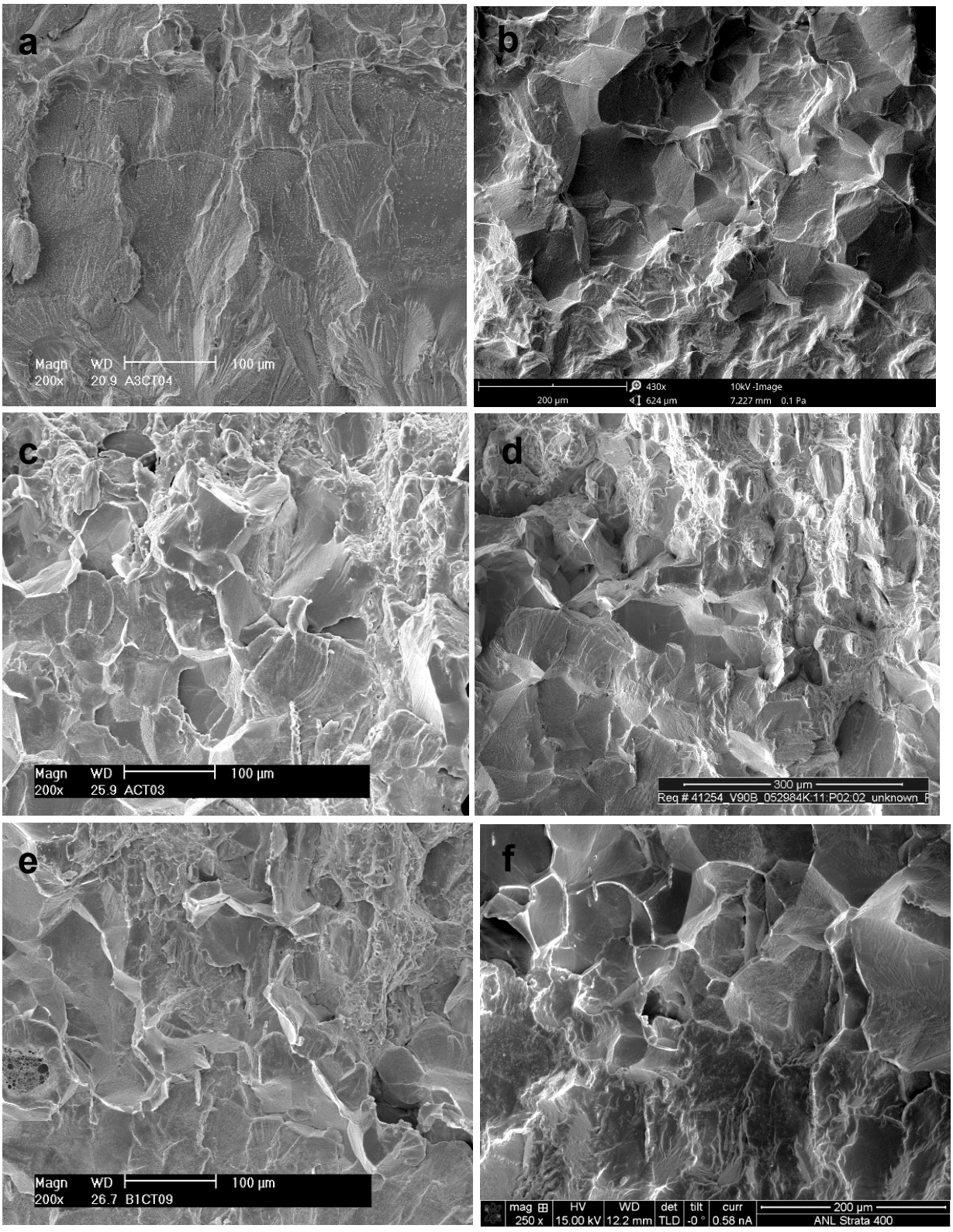

Figure 65. Fracture surfaces of the constant-K CGR regions of the specimens, (a) ~0.06 dpa, (b) ~8 dpa, (c), ~15 dpa, (d) ~39 dpa, and (e, f) ~47 dpa (crack advanced from bottom to top in all pictures)

5.3 Fracture Toughness J-R Curve Tests

Using the SCC cracks generated in the CGR tests as the starter cracks, fracture toughness J-R curve tests were performed on the samples in the test environments and temperatures. Figure 66 shows the J-R curves obtained from this study. The effect of neutron irradiation on the fracture resistance of the baffle plate material is evident. For the 0.06-dpa specimen, the power exponent of the J-R curve is about 0.6, similar to those of unirradiated 300-series SSs [22,23]. With the increase of irradiation dose, the J-R curve becomes much shallower, suggesting a significant reduction in fracture resistance. At ~47 dpa, the J-R curve is almost flat, indicating that very little energy is needed to propagate a crack once it has been initiated. There is no doubt that this baffle plate material was severely embrittled after 38 years in service.

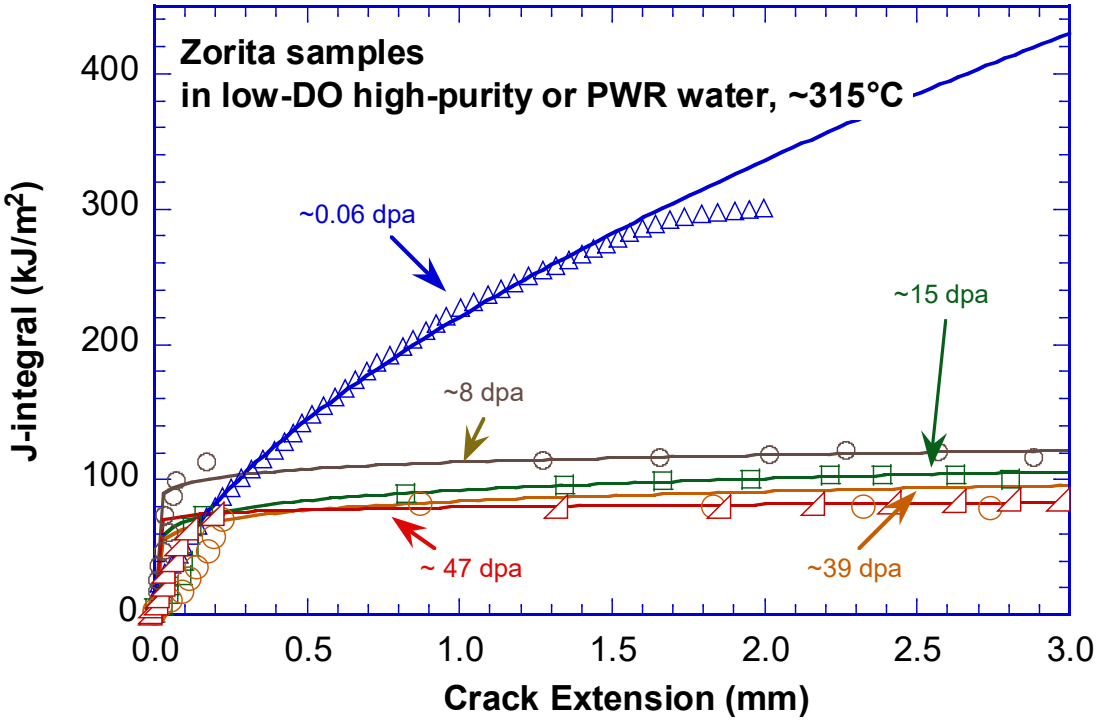

Figure 66. J-R curves obtained from the decommissioned Zorita baffle plate material.

As shown in Figure 66, the J-R curve of the decommissioned Zorita baffle plate material declines continuously with increasing dose. This dose-dependent behavior is better illustrated in Figure 67 with J values at 0.2- and 2.5-mm crack extensions. The effect of irradiation embrittlement is more evident with the $J_{2.5\text{-mm}}$ values. A sharp decline of the $J_{2.5\text{-mm}}$ value can be seen below 8 dpa with increasing dose, but slows considerably with the further increase in dose up to 47 dpa. The effect of irradiation-induced embrittlement can also be seen from the optical images of the fracture surfaces. As shown in Figure 68, the cross-section profiles of the fracture samples evolve from low to high doses. The side edges of the 0.06-dpa sample are curved due to the lack of constraint during its J-R test. The side edges become straight with increasing dose, indicating an improved constraint in the high-dose samples.

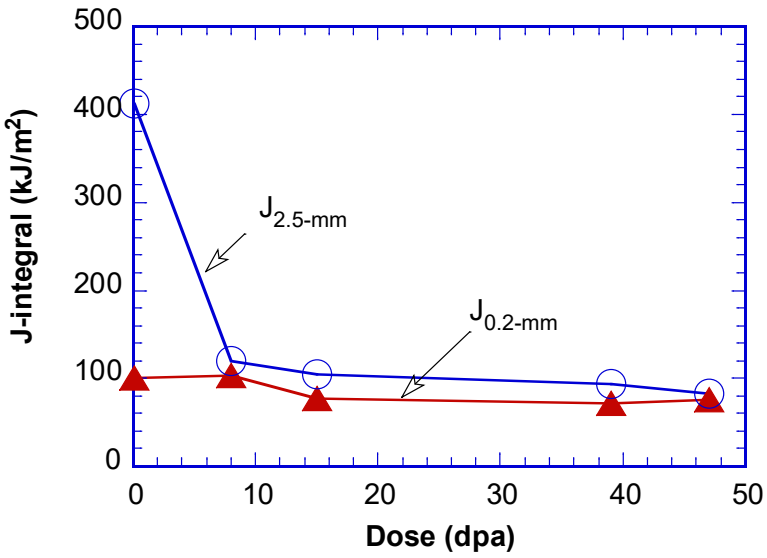

Figure 67. J values as a function of irradiation dose

For the 0.06-dpa sample, the $J_{0.2\text{-mm}}$ value is only 100 kJ/m^2, which is somewhat lower than those of unirradiated or slightly irradiated SSs [23]. In addition, cracking instability was observed in this sample during the load increases in the SCC test. The low J value and cracking instability in this sample may be related to inclusions or ferrite stringers that can be seen on the fracture surface. As shown in Figure 69, a large banded brittle area parallel to the cracking direction can be seen on the mostly ductile fracture surface. Smaller stringers along the deformation bands can also be seen on the fracture surface. This banded microstructure may be responsible for such a low value of fracture toughness. Nonetheless, the material can still resist the crack propagation considerably at this low dose level, and therefore a much higher toughness value can be expected at the 2.5-mm crack extension. With the increase of irradiation dose, the material becomes increasingly brittle, and the gap between the $J_{0.2\text{-mm}}$ and $J_{2.5\text{-mm}}$ diminishes rapidly, as shown in Figure 67.

The fracture morphologies of the J-R test region are very similar among these samples. Regardless of their irradiation doses, all J-R regions show a mix of ductile dimples and brittle fracture stringers parallel to the cracking direction, as shown in Figure 69. No IG morphology can be seen in the J-R test region, which contrasts sharply with both CGR and post-JR test regions.

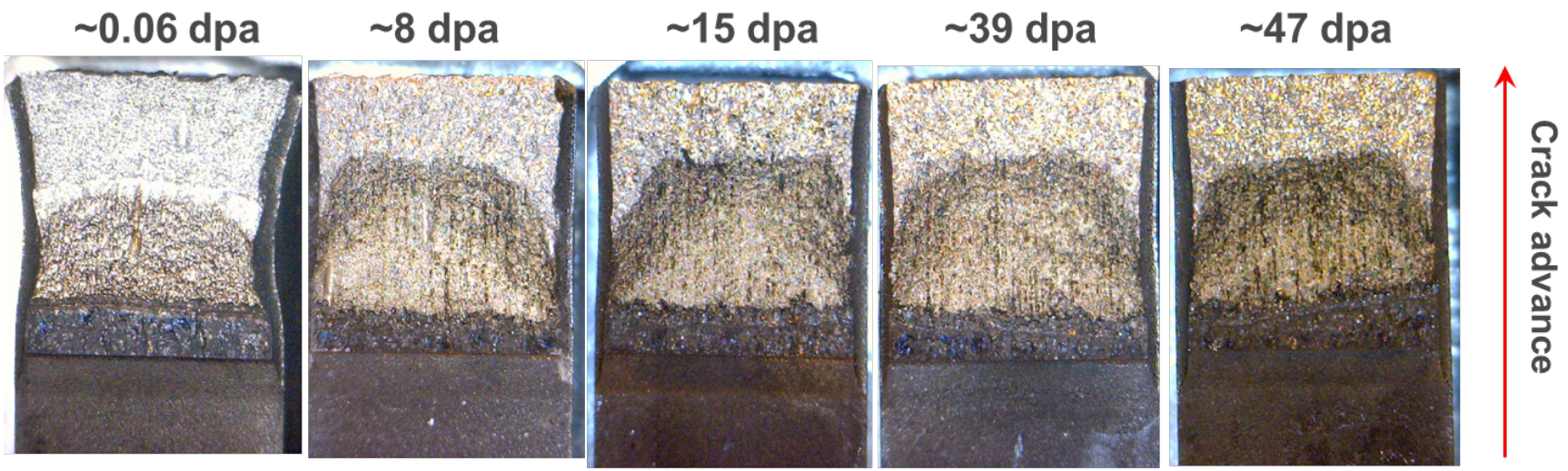

Figure 68. Optical images of the fractured samples

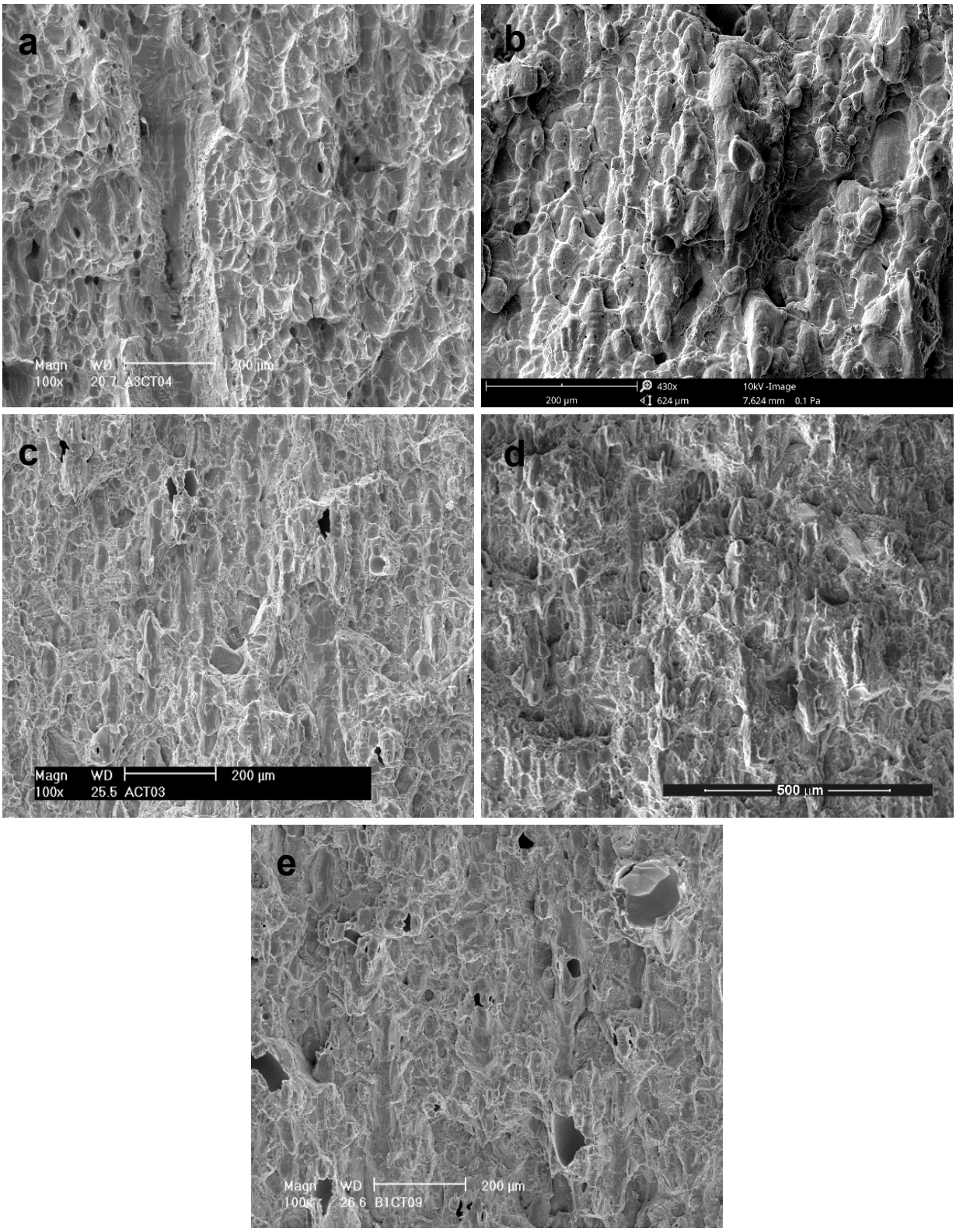

Figure 69. J-R curve test regions of the specimens, (a) ~0.06 dpa, (b) ~8 dpa, (c) ~15 dpa, (d) ~39 dpa, and (e) ~47 dpa (crack advanced from bottom to top in all pictures)

5.4 Fracture Morphology of the Final Ligaments

After the J-R curve tests, the samples were broken in air at room temperature with cyclic loading. The fracture morphologies of the final fractured ligament are shown in Figure 70. In general, cyclic loading was performed with a constant load amplitude, and a K_{max} between 40 and 80 MPa $m^{1/2}$. The final fracture of the ligament was done with a monotonic tensile load.

For the 0.06-dpa sample, ductile dimples are the dominant fracture mode, as well as some large stringers perhaps resulting from the manufacturing process that can be seen on its fracture surface. For the 8-dpa sample, a mixed-mode fracture of ductile tearing and IG cracking is observed (Figure 70b). For the other samples at higher doses, the fracture mode for the post-test fatigue regions is completely IG. This extensive IG fracture in air and at room temperature is unexpected because the samples were not subject to any high temperature water environment or elevated temperature at this stage of the test. Similar IG cracking in air was also reported by Jenssen et al. [24, 25]. This type of IG cracking in the absence of high temperature water environment can only be attributed to irradiation-induced embrittlement. Obviously, the observed IG cracking depends on irradiation dose, and may have a dose threshold below ~8 dpa and a saturation dose between 8 and 15 dpa for this decommissioned Zorita material.

It is interesting to note that the fracture of the final ligament on Specimen B1CT07 is not IG, but ductile dimples (see Figure 70f). This sample was broken during the CGR test, and therefore, its final fracture occurred in water at ~315°C, not in air at room temperature. The contrast between the two 47-dpa samples (i.e., Figure 70e-f) suggests that the IG morphology observed in the post-test regions is not only sensitive to irradiation dose, but also affected by deformation temperature. The IG fracture is more likely to occur at room temperature. This further confirms that the observed IG cracking at the final stage of the test is not an environmental phenomenon, but rather an embrittlement behavior sensitive to irradiation dose and deformation temperature. There is no doubt that neutron irradiation can cause brittle IG cracking in this baffle plate material with or without environments. Additional effort is needed to evaluate the extent of irradiation embrittlement in this material under similar conditions, especially at temperatures below typical LWR operating temperatures.

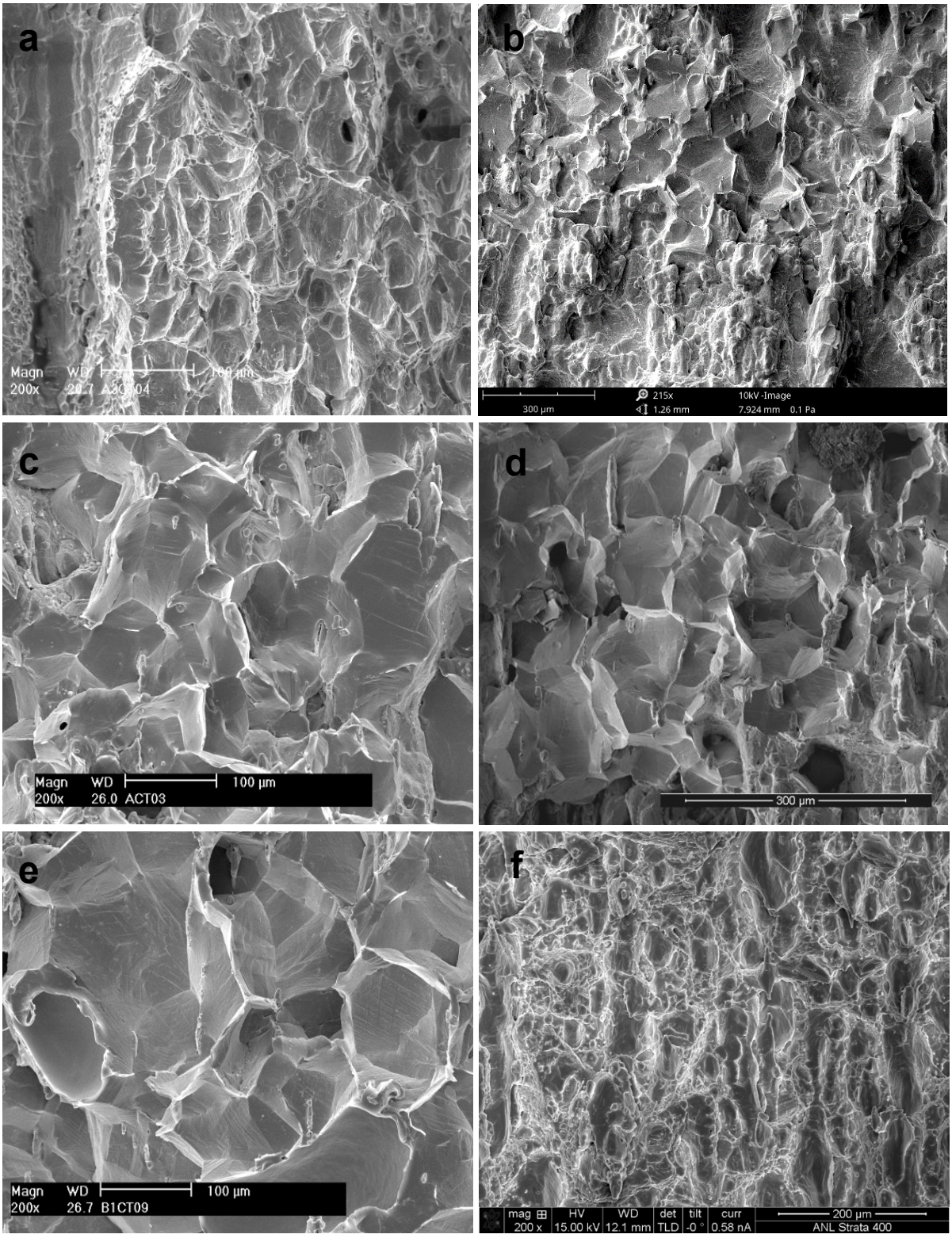

Figure 70. Post-JR fatigue regions fractured at room temperature in air for the specimens at (a) ~0.06 dpa, (b) ~8 dpa, (c) ~15 dpa, (d) ~39 dpa, (e) ~47 dpa, and (f) the final ligament of the 47-dpa sample fractured at ~315°C (crack advanced from bottom to top in all pictures)

6 SUMMARY

A Type 304 SS baffle plate material harvested from the decommissioned Zorita reactor was evaluated for cracking susceptibility and fracture toughness. Six specimens ranging from ~0.06 to ~47 dpa were tested in low-corrosion-potential environments. While all samples behaved similarly in the cyclic CGR tests, the 0.06-dpa sample seemed easier to pre-crack and showed a stronger environmental enhancement than the other samples irradiated to higher doses. All specimens except a 47-dpa sample showed a low SCC susceptibility in the low-corrosion-potential environments, and the measured CGRs were much lower than the NUREG-0313 disposition curve. No K or irradiation dose dependence can be seen among these samples.

An abnormal cracking behavior was observed in one of the 47-dpa samples, leading to extremely high CGRs above 25 MPa $m^{1/2}$. The exact trigger or condition for this cracking behavior is not clear and may be related to an unstable cracking phenomenon observed in this specimen. For the 0.06- and 47-dpa samples, an instant, stepwise crack growth behavior was observed upon load increase or reloading. This stepwise crack growth did not contribute to the stable SCC crack growth in the 0.06-dpa sample but could sustain a high growth rate in the 47-dpa specimen.

The effect of neutron irradiation on fracture toughness was evident among these samples. With increasing dose, the J-R curve declined considerably and became very shallow at high doses. It is evident that this baffle plate material was severely embrittled by neutron irradiation in service. In addition, the fracture toughness of the 0.06-dpa sample appeared to be lower than those of typical unirradiated or low-dose SSs. This may be related to the presence of ferrite stringers in the material.

In addition, an IG morphology was observed for all samples above 8 dpa in the post-test regions fractured at room temperature in air. The occurrence of this brittle fracture in the absence of high temperature water chemistry environment and elevated temperatures is unexpected and confirms a high degree of embrittlement for this material. Additional effort is needed to assess the extent of irradiation embrittlement for this material, especially below the LWR operating temperatures.

REFERENCES

1. U.S. NRC, “Expert Panel Report on Proactive Materials Degradation Assessment,” NUREG/CR-6923, 2006.
2. U.S. NRC, “Expanded Materials Degradation Assessment,” NUREG/CR-7153, 2013.
3. Chopra, O. K., B. Alexandreanu, E. E. Gruber, R. S. Daum, and W. J. Shack, *Crack Growth Rates of Irradiated Austenitic Stainless Steel Weld Heat Affected Zone in BWR Environments*, NUREG/CR-6891, ANL–04/20, 2005.
4. Chopra, O. K., and W. J. Shack, *Crack Growth Rates and Fracture Toughness of Irradiated Austenitic Stainless Steels in BWR Environments*, NUREG/CR-6960, ANL–06/58, 2008.
5. Chen, Y., O. K. Chopra, E. E. Gruber, and W. J. Shack, *Irradiation-Assisted Stress Corrosion Cracking of Austenitic Stainless Steels in BWR Environments*, NUREG/CR-7018, ANL-09-17, 2010.
6. Chen, Y., B. Alexandreanu, and K. Natesan, *Technical Letter Report on the Cracking of Irradiated Stainless Steels in Low-Corrosion-Potential Environments*, ANL-13/12, 2013.
7. Chen, Y., B. Alexandreanu, and K. Natesan, *Crack Growth Rate and Fracture Toughness Tests on Irradiated Cast Stainless Steels*, NUREG/CR-7184, ANL-12/56, 2015.
8. Chen, Y., B. Alexandreanu, and K. Natesan, *Crack Growth Rate and Fracture Toughness of Cast Austenitic Stainless Steels Irradiated to ~3 dpa*, ANL-17/15, 2017.
9. Chopra, O.K., and A.S. Rao, “A review of irradiation effects on LWR core internal materials – IASCC susceptibility and crack growth rates of austenitic stainless steels,” J. Nucl. Mater. 409 (2011) 235–256.
10. Barreira, P., and C. Cueto, “Radiation and Temperature Analysis of Zorita Baffle Plate and Core Barrel Weld Material,” Materials Reliability Program: Zorita Internals Research Project (MRP-392), EPRI, Dec. 2015
11. ASTM International, “Standard Test Method for Measurement of Fracture Toughness,” E1802-15a, *Annual Book of ASTM Standards*, 2015.
12. Mills, W. J., “Fracture Toughness of Type 304 and 316 Stainless Steels and Their Welds,” Int. Mater. Rev. 4(2), (1997) 45.
13. Chen, Y., W. Soppet, B. Alexandreanu, and K. Natesan, *Technical Letter Report on Slow Strain Rate Tensile Tests of Irradiated Stainless Steels in PWR Environment*, ANL-12/33, 2012.
14. Andresen, P.L., F.P. Ford, S.M. Murphy, and J.M. Perks, “State of Knowledge of Radiation Effects on Environmental Cracking in Light Water Reactor Core Materials,” Proc. 4th Intl. Symp. on Environmental Degradation of Materials in Nuclear Power Systems - Water Reactors, NACE, Houston, TX, pp. 1.83–1.121, 1990.
15. ASME Boiler and Pressure Vessel Code, Section XI, Non Mandatory Appendix C, ASME, New York.
16. Hazelton, W.S., and W.H. Koo, *Technical Report on Material Selections and Processing Guidelines for BW coolant Pressure Boundary Piping*, Final Report, NUREG-0313, Rev.2, 1988.
17. Shack, W. J., and T. F. Kassner, *Review of Environmental Effects on Fatigue Crack Growth of Austenitic Stainless Steels*, NUREG/CR-6176, 1994.
18. Eason, E., and R. Pathania, “Irradiation-assisted stress corrosion crack growth rates of austenitic stainless steels in light water reactor environments,” 17th International Conference on Environmental Degradation of Materials in Nuclear Power Systems – Water Reactors August 9–13, 2015, Ottawa, Ontario, Canada
19. *Materials Reliability Program Development of Material Constitutive Model for Irradiated Austenitic Stainless Steels*, MRP-135, EPRI Report 1011127, 2004.

20. Chen, Y., B. Alexandreanu, K. Natesan, and A.S. Rao, “Crack Growth Behavior of Irradiated 304L SS in PWR environment,” 16th Intl. Symp. on Environmental Degradation of Materials in Nuclear Power Systems - Water Reactors, Asheville, NC, 2013.
21. Andresen, P.L., and M.M. Morra, “Effects of positive and negative dK/da on SCC Growth Rates,” Proc. 12th Intl. Symp. on Environmental Degradation of Materials in Nuclear Power Systems - Water Reactors, TMS, 2005.
22. Chen, Y., B. Alexandreanu, W-Y. Chen, K. Natesan, Z. Li, Y. Yang, and A. S. Rao, “Cracking Behavior of Thermally Aged and Irradiated CF-8 Cast Austenitic Stainless Steel,” *Journal of Nuclear Materials*, 466 (2015) 560.
23. Mills, W.J., “Facture Toughness of Irradiated Stainless Steel Alloys,” *Nucl. Technol.* 82 (3) (1988) 290.
24. Jenssen, A., V. Grigoriev, R. Jakobsson, and P. Efsing, “Fracture Resistance Evaluation of a Flux Thimble Irradiated to 65 dpa in a PWR,” Contribution of Materials Investigation to Improve the Safety and Performance of LWRs (Fontevraud 6), Sept. 18–22, 2006, Avignon, France
25. Jenssen A., P. Efsing, B. Forssgren, B. Bengtsson, and M. Molin, “Examination of Highly Irradiated Stainless Steels from BWR and PWR Reactor Pressure Vessel Internals,” Contribution of Materials Investigation to Improve the Safety and Performance of LWRs (Fontevraud 7), Sept. 26–30, 2010, Avignon, France

Nuclear Engineering Division
Argonne National Laboratory
9700 South Cass Avenue, Bldg. #208
Argonne, IL 60439

www.anl.gov

Argonne National Laboratory is a U.S. Department of Energy laboratory managed by UChicago Argonne, LLC